Clemson University
TigerPrints

All Theses | Theses

12-2009

# A Study of the Mesosphere-Lower Thermosphere: Noctilucent Cloud Observations and Rocket Borne Density Measurements

Shelton Simmons
*Clemson University*, akfdda@hotmail.com

Follow this and additional works at: https://tigerprints.clemson.edu/all_theses

 Part of the Atmospheric Sciences Commons

Recommended Citation
Simmons, Shelton, "A Study of the Mesosphere-Lower Thermosphere: Noctilucent Cloud Observations and Rocket Borne Density Measurements" (2009). *All Theses*. 698.
https://tigerprints.clemson.edu/all_theses/698

This Thesis is brought to you for free and open access by the Theses at TigerPrints. It has been accepted for inclusion in All Theses by an authorized administrator of TigerPrints. For more information, please contact kokeefe@clemson.edu.

# A STUDY OF THE MESOSPHERE-LOWER THERMOSPHERE: NOCTILUCENT CLOUD OBSERVATIONS AND ROCKET BORNE DENSITY MEASUREMENTS

---

A Thesis
Presented to
the Graduate School of
Clemson University

---

In Partial Fulfillment
of the Requirements for the Degree
Master of Science
Physics.

---

by
Shelton O'Brien Simmons
December 2009

---

Accepted by:
Dr. Gerald Lehmacher, Committee Chair
Dr. Miguel Larsen
Dr. Sean Brittain

**Acknowledgements**

I would like to thank my advisor, Gerald Lehmacher, for all of his help with programming and researching these topics. I gratefully acknowledge the support of Gerd Baumgarten of IAP for allowing me the use of his photographs. I would also like to thank my grandmother, Earnestine, my parents Callie and Samuel, my stepfather Kenneth, and my brother, Lionel, for their support during my graduate career. I am indebted to Edward, Jasper, and Ramesh for their input and assistance. Last, but not least, I'd like to thank Cassie for all of her patience, understanding, and support throughout the researching and writing of my thesis.

## ABSTRACT

Herein, a study of a noctilucent cloud, NLC, display from 17 July 2007 is analyzed. A photogrammetric analysis was applied to time lapsed photographs taken from two observation sites, Rügen and Kühlungsborn, Germany. Both Kelvin-Helmholtz instabilities and internal gravity waves were identified during the NLC display based on the typical characteristics of such waves in the mesopause region. With the two observation sites, the location of details can be identified with an accuracy of $\pm 0.125\,^{\circ}$ longitude and $\pm 0.5\,^{\circ}$ latitude. A gravity wave with a wavelength of 50 km and Kelvin-Helmholtz instability or gravity wave of wavelength 16.5 km were observed. The 16.5 km wave had an apparent phase speed of $22\,\mathrm{m\,s^{-1}}$.

Two CONE ionization gauges are calibrated for a rocket campaign which took place in February of 2009. Their ion, emission, and filament currents are discussed as well as the results of a least squares fit to write the pressure as a function of the normalized ion current using both a polynomial and Gaussian fit. The results of the fits are then used to make a temperature profile of the MLT region. The resulting pair of temperature profiles agree on the temperature and location of the mesopause, $152\,\mathrm{K} \pm 12\,\mathrm{K}$ at about 92.5 km.

# Contents

# List of Figures

*Facilis descensus Averni;*
*Noctes atque dies patet atri janua Ditis;*
*Sed revocare gradum, superasque evadere ad auras,*
*Hoc opus, hic labor est.*

# Part I

# Photogrammetric Analysis of Noctilucent Clouds Over Sweden

## Chapter 1

# Introduction

Noctilucent clouds, or NLCs as they are commonly abbreviated, have been an object of fascination to the amateur observer as well as to the astute scientist ever since their discovery during the late 1800s. These NLCs are natural tracers which can allow us to determine the dynamics of the region that they highlight, namely the mesopause region. While there are other ways of studying the mesopause or, more loosely, the mesosphere as a whole, assaying noctilucent clouds is the least expensive and unobstructed way of doing so. Furthermore noctilucent clouds are a medium in which waves propagate throughout the mesopause region. A photogrammetric analysis can reveal not only background wind speeds but also wave propagation throughout this region, which is the goal of this study. The mesosphere and lower thermosphere, or the MLT region, is quite difficult to study for various reasons. The mesosphere is the region of the atmosphere that ranges from approximately 50 km to 90 km in altitude where the range is approximated because this region's niche varies not only with latitude, but with season. The mesopause acts as the ceiling of this region, being the place where the temperature reaches an absolute minima throughout the mesosphere. There are only a handful of ways to study this region of the atmosphere; rocket-borne probes, LIDAR, and via satellites. Rocket borne in-situ probes are an excellent way of studying this region but they are quite expensive and they can only give static measurements. LIDAR or **Li**ght **D**etection **a**nd **R**anging provides another means of observing the mesosphere but again it is an expensive apparatus with a high operating cost. Furthermore their usage is parceled out in such a way that one never has a LIDAR that is specifically tuned to monitor this region of the atmosphere. The last

way of observing the mesosphere, other than using NLCs, is with a satellite. Satellites are more expensive than the rockets and an in-situ satellite will be quite unstable within this region. There have been some satellites, such as the AIM satellite, which have obtained valuable information on the mesosphere, however they were never put into a stable orbit. All satellites below 2000 km will experience orbital decay which ultimately results in the satellite's descent to the Earth. That being said there is no low-maintenance, low-cost alternative to studying the mesopause region other than photogrammetry.

Photogrammetry is the methodology of using a photograph to determine the geometry of inherent within a photograph. This science has been used on tropospheric clouds before the rise of commercial airlines and Doppler radars. There are various ways of extrapolating the intrinsic geometry from a photograph, all of which have been well documented. My method will be similar to that used by Georg Witt, the first researcher to apply photogrammetry to assay noctilucent clouds. Given a photograph, a coordinate system is assigned to it in which the center of the image becomes the origin. This image-coordinate system is then mapped to one that is tangent to the celestial sphere, the standard-coordinate system. From the standard coordinate system and a star map we can determine the position of any point in the photograph in terms of right ascension and declination, which can be directly converted into longitude and latitude. From those, background windspeeds and wave parameters can be readily determined. In particular, the waveform characteristics can be determined by hand as well as by the application of a FFT.

# Chapter 2

# The Earth's Atmosphere

## 2.1 Layers of the Atmosphere

The atmosphere can be described as a series of concentric spherical shells, each with their own idiosyncrasies. The primary variables that are usually considered for gases are volume, pressure and temperature as per the ideal gas law however that is not the case for the atmosphere as a whole. The volume is intrinsically considered within our spherical shells because they are bounded by altitude. The pressure is assumed to follow the conditions of hydrostatic equilibrium, which is usually a good assumption. This leaves us with the temperature which varies with altitude and this gives us a way of segmenting the atmosphere into various concentric shells, each with its own characteristic temperature behavior.

The sphere that we live in, the troposphere, is characterized by a temperature profile that decreases steadily with height. This is because most of the heat is supplied by interactions with the earth's surface. The troposphere ranges from sea level to about 10 km in height, however its maximum extent can vary with latitude and the time of the year. Over the tropics its maximum height can be as high as 16 km in the summer while over the poles the troposphere can be completely absent during the winter. Since the true shape of the Earth is an ellipse it stands to reason that the tropopause should be somewhat elliptical. The top of the tropopause is characterized by a local temperature minimum called the tropopause which acts as the boundary between the troposphere and the stratosphere.

Extending from the tropopause to about 50 km in altitude is the stratosphere or

stratified sphere because the mean air flow in this regime can be categorized solely by the strata or layer of interest. The temperature in this region rises steadily throughout because of the absorption of ultraviolet radiation by ozone throughout most of this region. Because of this the stratosphere is dynamically stable, that is the convection and turbulence that are readily apparent in the troposphere are weaker in the stratosphere. Thus some long range aircraft fly through the bottom of the stratosphere to ensure a smooth ride. The temperatures in the stratosphere approach the temperatures that we experience on the surface with a maximum of about 270 K or 30 °F. The emission of infrared radiation by stratospheric carbon dioxide has a cooling effect in this region and interestingly the amount of carbon dioxide in the stratosphere has been increasing lately. At the top of the stratosphere there is a temperature maximum above which lies the coldest part of the atmosphere and our region of interest, the mesosphere.

The mesosphere or middle-sphere is the region of the atmosphere that ranges from about 50 km to about 90 km in altitude. It is characterized by a steady drop in temperature with increasing altitude due to gravity wave breaking. The region where the temperature reaches a minimum is called the mesopause. The mesopause ranges from 80 km to 90 km throughout the year and the temperatures can fall as low as $111K$(Gadsen and Schröder 1989).

Above the mesopause, extending outwards to an altitude of 500 km is the region of the atmosphere called the thermosphere. Within this sphere the temperature rises throughout and can vary from 600 K to 2000 K at the thermopause due to the absorption of solar radiation by oxygen, which is the primary constituent. In contrast to the stratosphere, the atoms and molecules within the thermosphere can and do become ionized. Another idiosyncrasy of the thermosphere is that oxygen becomes highly dissociated with elevation and above 130 km it exists almost entirely in atomic form. Furthermore diffusion becomes less and less important since the mean free path is so large at these altitudes and therefore turbulence becomes less and less of an issue. Because of this the heavier fluids tend to fall out and become less concentrated with

altitude akin to what happens in Italian dressing. Above this region lies the final boundary between earth and space, the exosphere.

The exosphere extends from the thermopause all the way to outer-space. From 500 km to around 1000 km helium replaces oxygen as the dominant constituent and above 1500 km atomic hydrogen is replaced by helium. The main characteristic of this region is that atomic hydrogen and helium can escape from the Earth's gravitational pull as they diffuse upwards if they are travelling faster than the earth's escape velocity. As mentioned when describing the thermosphere, the mean free path of these atoms is so great that it is highly unlikely for them to hit anything. The more massive particles, such as nitrogen, diffuse upwards at a much slower rate and therefore have a smaller, almost negligible chance of escaping from the Earth's gravitational pull(Bussinger and Fleagle, 1980).

## 2.2 Hydrostatic Equilibrium

Hydrostatic equilibrium is an assumption based on the concept that the mass of any particle in the atmosphere is being acted upon by two main forces; a net downward force caused by the net gravitational attraction of every particle above it, namely the weight of the atmosphere above it, and pressure caused by collisions with any particles beneath it. Because of the presence of weight we have to take the centrifugal force caused by the Earth's rotation into consideration. The centrifugal force would cause the mean flow to accelerate however, assuming that the flow is steady or hydrostatic, then centrifugal accelerations can be neglected and so the weight of the atmosphere above an unit plane is simply the pressure exerted by the atmosphere on the plane, the ubiquitous atmospheric pressure that can be readily measured with a barometer.

An emergent property of hydrostatic equilibrium is the relationship between pressure and height. The gravitational constant, $g$, is practically constant within the troposphere therefore the atmospheric pressure decreases linearly with height. The weight of the atmosphere above any unit plane is merely $\rho g$ where $\rho$ is the mass density per unit

volume therefore we have

$$dp = -\rho g dz \tag{2.1}$$

which is the basic equation governing hydrostatic equilibrium. Assuming that the atmosphere is an ideal gas we can write the density as

$$\rho = \frac{Mp}{kT} \tag{2.2}$$

where $m$ and $T$ represent, respectively, the molecular mass and temperature of the atmosphere. The gas constant is given by $R$ and so 2.1 can be rewritten as

$$\frac{dp}{p} = -\frac{mg}{kT} dz \tag{2.3}$$

where the quantity $\frac{RT}{mg}$ is typically called the scale height, $H$, the increase in altitude necessary to decrease the pressure by a factor of $e$. Integrating 2.3 we find

$$\ln\left(p_f - p_i\right) = -\frac{(z_f - z_i)}{H} \tag{2.4}$$

where the subscript $i$ represents initial and $f$ represents final. We can rewrite this as

$$p_f = p_i \exp\left(-\frac{(z_f - z_i)}{H}\right). \tag{2.5}$$

From this we can plainly see that pressure falls off exponentially with height, thereby proving that most of the mass in the atmosphere is within the troposphere. Hydrostatic equilibrium merely means that any accelerations due to the Coriolis Force are neglected. Naturally pressure isn't the only variable to consider when describing the

atmosphere as a whole. Just as the different regions can be described in terms of temperature, so to can the conditions of hydrostatic equilibrium. Writing the ideal gas law as

$$P = \rho m k T \tag{2.6}$$

where $P$ represents pressure, $\rho$ is the density of particles, $k$ is Boltzmann's constant, and $T$ represents temperature 2.1 can be rewritten as

$$dp = -gm\rho dz. \tag{2.7}$$

Since the objective is to express everything in terms of temperature this is recast as

$$d\left(\rho k T\right) = -gm\rho dz \tag{2.8}$$

which can be quickly rewritten as

$$kd\left(nT\right) = -gm\rho dz. \tag{2.9}$$

Putting the constants on the right hand side we have

$$d\left(\rho T\right) = -\frac{gm\rho\left(z\right)}{k} dz \tag{2.10}$$

which can be integrated to yield

$$\delta\left(\rho T\right) = -\int_{z_1}^{z_2} \frac{gm}{k} \rho\left(z\right) dz. \tag{2.11}$$

The left hand side can be evaluated using the total change theorem therefore we have

$$\rho(z)\,T(z) - \rho(z_0)\,T(z_0) = -\int_{z_1}^{z_2} \frac{gm}{k}\rho(z)\,dz \tag{2.12}$$

or

$$T(z) = \frac{1}{\rho(z)}\left(\rho(z_0)\,T(z_0) - \int_{z_1}^{z_2} \frac{gm}{k}\rho(z)\,dz\right) \tag{2.13}$$

While the right-hand side of 2.13 cannot be integrated analytically, it can be integrated numerically assuming a boundary condition is known.

## 2.3 Mesosphere Dynamics

The only place in the upper atmosphere that can support cloud formation is the mesosphere. The mesosphere is characterized by cooling due to gravity wave breaking and the radiative emission of infrared light by $CO_2$ as well as dynamics caused by Kelvin-Helmholtz instabilities gravity waves and planetary waves. It ranges from about 50 km-90 km. Above the mesosphere the atmosphere begins to warm up again due to the absorption of ultraviolet light by molecular and atomic oxygen. Therefore there is a temperature minimum at some height in the mesosphere which we call the mesopause, around 85 km.

Gravity waves are caused when gravity acts as the restoring force when a parcel of air is displaced into a region of air with a different density than the parcel. The gravitational force tries to "restore" the air parcel to its equilibrium position. However there isn't anything to dampen out this motion as it approaches equilibria. And so the air parcel will overshoot its equilibrium position until the restoring force is overcome by the parcel's buoyancy. The parcel will then proceed to rise towards its equilibrium position and overshoot it again. This oscillation around its equilibrium position is the

cause of the gravity wave. As the gravity wave propagates its amplitude increases because the density of air decreases with altitude. Furthermore gravity waves represent a mechanism of momentum transfer from one region in the atmosphere to the mesosphere.

Kelvin-Helmholtz instabilities result from the sheers between adjacent layers of the atmosphere. These instabilities cause waves akin to waves on the surface of an ocean. Given two vertically adjacent layers of fluid, each with its own distinctive density, an air parcel that is displaced from a lower density to a higher one will try to retain equilibrium as per the oscillations that cause gravity waves. However, if the two fluid laminae are moving at different velocities then a displaced parcel's path becomes circular. It is this kind of mixing, due to a sheer, that produces the Kelvin-Helmholtz instability. The Kelvin-Helmholtz instability becomes more pronounced as the wave becomes unstable due to the build-up of high density air within the low density lamina which ultimately results in breaking, akin to the breaking of ocean waves.

Planetary waves are caused by variations in the Coriolis force with latitude. Because of that variation there is a shear between the different sections of the atmosphere akin to what happens when a low-pressure system interacts with a high-pressure system. The air mixes and overturns like ocean waves but, unlike the ocean waves planetary waves are stationary with a variable period.

Planetary or Rossby waves are caused by variations in the Coriolis force with latitude. To get a feeling for this type of motion we must consider vorticity which is defined as the curl of the velocity vector. Mathematically the curl of a vector field is always associated with gyre-like motions. Of particular importance is the normal or vertical component of the vorticity because we assume that the air parcel moves at a constant height therefore any rotations would be in the plane parallel to the earth's surface. The vorticity vector describes any circular motion in a fluid at any point within the fluid. Any component of the vorticity vector that causes clockwise rotations is considered negative or anticyclonic. It follows that any component that produces counterclockwise flows is considered positive or cyclonic

If we consider a column of air extending from the surface of the earth to the lower stratosphere then we can consider any changes in the pressure of individual air parcels to be negligible such that change in vorticity with respect to time is a constant. If a parcel of air in our column at some intermediate height is perturbed from its equilibrium position in such a way that it moves diagonally with a northward component it must curl clockwise as it moves northward to conserve its vorticity. It will reach a local maximum in its anticyclonic motion at higher latitudes before it overturns and moves southwards. As it moves southwards the conservation of vorticity acts like a restoring force that tries to push the air parcel back into its equilibrium position but there is no mechanism to dampen out the motion and so our parcel reaches a local minimum in its cyclonic motion and then proceeds northwards to repeat the whole travail.

Of the three kinds of dynamics; gravity waves, Kelvin-Helmholtz instabilities, and planetary waves, only the former two will be considered as candidates for the dynamics revealed in this study. While planetary waves exist within the mesosphere, one night of data isn't sufficient to properly identify them. The most common planetary wave seen within the mesosphere is the 5-day wave which cannot be detected from a the data of a single night.

# Chapter 3

# Noctilucent Clouds

## 3.1 History

Noctilucent clouds were first studied in 1885 when Jesse(1885), Tserasaki(1887), and Leslie(1885), were independently observing the twilight sky to investigate the after-effects of the dust that was placed into the atmosphere by the eruption of Krakatoa. From then on they have been observed by both amateurs and researchers alike.

The history of noctilucent clouds is a plethora of observations coupled with a multitude of questions concerning the origins of the clouds, the nature of the cloud particles as well as their sizes, and the temperature profile of the mesosphere. Such questions as to why they shine at night?, are they visible during the day?, what kinds of waves are present within the clouds?, why are only visible during the summer?, and why can't they be seen at lower latitudes are usually left to be explained by books or by the earliest observations. It is the answers to questions like these that illuminate the differences between noctilucent clouds and tropospheric or stratospheric clouds. Here we will try to address each of these so that the reader can fully appreciate the NLCs.

The NLCs, or "night-shining" clouds, are so-called because they are only visible, by the naked eye, during twilight when they are still illuminated by sunlight that comes from beyond the horizon. They can only be seen by the naked eye during dusk against the twilight sky. This is because they are so nebulous that the incident sunlight that is scattered by them is completely screened by the ambient light of the sky. It is only because their high altitude enables them to remain illuminated by the Sun while the

surface beneath them is within the Earth's shadow that they are visible to the naked eye. Twilight is when the Sun falls below the horizon and falls into three different categories; civil, nautical, and astronomical. Civil twilight or sunset, when the Sun is between $0\,^\circ$ and $6\,^\circ$ below the horizon is usually too early to see noctilucent clouds. Nautical twilight or dusk, when the Sun is between $6\,^\circ$ and $12\,^\circ$ below the horizon, and astronomical twilight is when the Sun is between $12\,^\circ$ and $18\,^\circ$ below the horizon. It is the nautical twilight that is the most opportune time to see the noctilucent clouds. During the middle of nautical twilight anything from roughly 40 km to 60 km in elevation becomes illuminated while everything below that range is within the Earth's shadow. Sunlight scattered within the mesosphere produces a faint luminescence against which the NLCs can be readily observed(Bronhsten and Grishin, 1976). It is no small wonder that no one noticed the noctilucent clouds until after the industrial age.

NLCs aren't visible to the naked eye during the day. However, this is not because they aren't there, but rather because of the relative density of the clouds, coupled with incident daylight culminating in an effect that is synonymous to the invisibility of stars during the day. The mesopause region is where the NLCs form and thus it is useful to compare it to something with which we are all familiar, the troposphere. We live in the troposphere and all of the weather that we are familiar with arises within the troposphere. The density of the surrounding atmosphere, the mesopause region, is roughly $8.22 \times 10^{-6} \frac{\mathrm{kg}}{\mathrm{m}^3}$ which is over six orders of magnitude lower than densities within the troposphere. Furthermore the amounts of water vapor in the troposphere and in the mesosphere are highly different. Needless to say the amount of water vapor within the troposphere can vary a lot at sea level. At higher latitudes, $80\,^\circ$ and above, the amount of water vapor in the troposphere can have a mixing ratio as low as $0.5 \frac{\mathrm{g}}{\mathrm{kg}}$(Bussinger and Fleagle, 1980), that is 0.5 g of water vapor for every kg of background air. In the mesopause region the water vapor mixing ratio is $1.2 \frac{\mathrm{g}}{\mathrm{g}}$(Bronhsten and Grishin, 1976) or $1.2 \times 10^{-3} \frac{\mathrm{g}}{\mathrm{kg}}$ which is less than a quarter of a percent of the lowest mixing ratio of water vapor within the troposphere. Indeed "the entire water content above 80 km could freeze

out to give just one cloud particle of radius 0.042 mm for each square meter of cloud layer..."(Gadsen and Schröder 1989) That being said it is no surprise that the noctilucent clouds require the cold temperatures of the summer mesopause region to condense.

Noctilucent clouds are the highest clouds in the earth's atmosphere ranging from 82 km −85 km. While gases exist from the exosphere to the troposphere the mesosphere is the last region of the atmosphere where the temperature falls enough for clouds, visible mixtures of water or ice particles, to condense. As mentioned earlier the temperature drastically increases above the mesopause. This coupled with the dissociation of water vapor within the thermosphere makes it impossible for the right set of conditions that would allow cloud formation. It is, somewhat surprisingly, the summer mesosphere which has temperatures cold enough for noctilucent cloud formation.

The mesosphere's temperature profiles is controlled by three main factors; the absorption of infrared radiation by carbon dioxide, the general circulation of the middle atmosphere, and the way in which gravity waves break throughout this region. Carbon dioxide absorbs radiation throughout the mesosphere which acts as a warming mechanism. The general circulation is driven by heating and cooling within the troposphere which sets up a zonal flow. This zonal flow continues throughout the stratosphere and becomes altered in the mesosphere due to gravity wave breaking. Gravity waves break near the mesopause, depositing energy into this region which decelerates the mean flow causing a new circulation. The new circulation causes air in the mesosphere to rise over the summer pole and to then flow meridionally to the winter pole where it begins to descend.

Another difference between the NLCs are the more common garden tropospheric clouds is from where they can be seen from the ground. Needless to say tropospheric clouds can be readily seen from all latitudes because their formation isn't restricted to a certain region of the Earth. In contrast, the noctilucent clouds, are a polar phenomenon. As they flow away from the poles they will inevitably become warmer and as that happens they will vanish. Furthermore the observer is always a few degrees of latitude

lower than the clouds themselves and since this is a summer phenomenon the NLCs cannot be seen above the Arctic Circle, above which the Sun doesn't set during the summer. With these acting as a floor and ceiling, respectively, on the latitudes of observation it is no wonder that the noctilucent clouds were not discovered until after the Industrial Revolution. Typically the NLCs are observed between 50° and 60° however T. D. Bessonova has reported NLCs as low as 45° and as high as 71°(Bronhsten and Grishin, 1976, pg. 48). In spite of those differences, however, the noctilucent clouds do have some similarities with the tropospheric and stratospheric clouds.

The most obvious similarity between the two kinds of clouds is the in their appearance. In general we can see all sorts of shapes and patterns inherent within the tropospheric and stratospheric clouds from faces to more defined structures like the so-called mackerel sky. Furthermore common clouds have been systematically categorized based on the base height of the clouds and how they are formed. However the noctilucent cloud layer is restricted to height of about 1 km because of the cold temperatures needed to sustain them. Nevertheless there are five types of NLCs as per the International Noctilucent Cloud Observation Manual(WMO, 1970); Type I or Veils, Type II or Bands, Type III or Billows, Type IV or Whirls, and Type V or Amorphous.

## 3.2 Noctilucent Cloud Types

Veils are the most basic representation of the NLCs. As their name suggests they are quite tenuous and are usually seen as a backdrop from which other types can be seen. Since they have no structure veils can be quite difficult to notice without other cloud types present. Bands are long streaks which usually appear parallel to one another or interlaced. These cloud types do not change much over time which indicates that they were caused by some sort of stationary wave. Furthermore, the presence of a veil can mask the edges of a band, making them appear more diffuse. Notice how one band is almost indistinct because of the background veil in Figure 3·1 while another is only partially screened.

**Figure 3·1:** Noctilucent cloud bands and a veil where the veil obscures the edges of two bands. This photograph was taken on May 14, 2007 from Rügen, Germany courtesy of Gerd Baumgarten of IAP.

Billows are akin to bands but they are more closely spaced and not as long. Indeed billows normally appear perpendicular to bands such that the billows appear like the teeth of a comb with the band as the spine. The individual billows can be so close together that they appear to be nearly continuous or far enough apart to show distinctive wave-like patterns. Billows predominantly appear near the fringes of a noctilucent cloud system some of which are caused by interferences between the surfaces of other features much like water waves. Ergo the billows are the only features in NLCs that can be attributed to Kelvin-Helmholtz instabilities.

In Figure 3·2 we see a spectacular example of NLC billows. Notice how the bottom right side of the image is screened by a veil. They are like the bands of Figure 3·1 however the billow crests are far closer together than the bands corresponding to a smaller wavelength.

Whirls are dark centered elliptical features which may or may not be completely formed. They form within the previous noctilucent cloud types and have been observed to both flow with and against the mean airflow. Generally any sort of curvature is referred to as a whirl.Figure 3·3 clearly shows a whirl within a veil. Interestingly we see

**Figure 3·2:** Billows within a noctilucent cloud display on July 18, 2007 from Rügen. Courtesy of Gerd Baumgarten from IAP.

what appears to be subsequent whirls within the main one which are obscured by the veil. It is also apparent that there is a pair of either bands or rather long billows that are tangential to the whirl, thus giving us a sense of the underlying motions within the image.

The final cloud type, the amorphous is akin to a veil in that it's utterly indistinct however the amorphous is brighter which makes it easier to recognize than veils. Here we can clearly see the amorphous along with bands and billows. They all share, relatively, the same luminosity however the amorphous is akin to a palette on which we see the more interesting bands, billows, and whirls.

Noctilucent clouds are composed of ice particles that form in the mesosphere due to the extreme intrinsic coldness of the mesosphere. The temperatures can get as low as 120 K, so low that air is overly saturated in comparison to water vapor even despite the intrinsic dryness of the mesosphere. The average frost point temperature in the mesosphere is roughly 145 K(Espy, P.J. and Hutt, J., 2002). However the NLCs require a seed particle for cloud condensation which is most likely a form of meteoric smoke. As the NLC condenses it gets heavier and thus falls to a lower altitude where the temperature is higher and the background air is less saturated compared to the water vapor. Therefore the NLC starts to evaporate as it falls below the mesopause, roughly

**Figure 3·3:** Whirl within a noctilucent cloud display over Rügen, Germany on July 19, 2007. Courtesy of Gerd Baumgarten of IAP.

**Figure 3·4:** An amorphous taken from Rügen, Germany on July 1, 2006. Courtesy of Gerd Baumgarten of IAP.

83 km.

There have been numerous attempts to observe and study NLCs during the 20th century. Most efforts have been done using photogrammetry, the art of using photographs of a system to discern the physical geometry of the system. Georg Witt(1962) was one of the first scientists to use photogrammetry to examine the dynamics of the NLCs.

## 3.3 Other Observational Techniques

The mesosphere has been difficult to study previously mainly because of its location. One common way of getting data about the atmosphere is to use probes on aircraft but the maximum height for normal commercial aircraft is around 10 km, just beneath the

top of the troposphere. Another method is using balloon-borne probes but the highest balloon, the Ultra Long Duration Balloon, can only reach altitudes of about 45 km which is still too low to study the mesosphere. Needless to say, balloons and commercial aircraft would be the cheapest means of putting probes into the mesosphere. One might think that satellites could be used for in-situ it but it is too low for geosynchronous orbits. Rockets have been useful in getting information about the mesosphere but, aside from their relative high costs, they only give information on a very small time scale, roughly 7 min round trip. One should note that it does not take a rocket roughly 3.5 min just to reach the mesosphere, depending on the probe it might be in the best interest of the scientist to have the rocket overshoot the region of interest, particularly when a probe needs to be calibrated. This leaves three other means of studying the mesosphere, satellites such as the AIM satellite, LIDAR, and all-sky cameras. The CIPS, **C**loud **I**maging and **P**article **S**ize, probe exclusively studies NLCs. The AIM, **A**eronomy of **I**ce in the **M**esosphere, satellite was initially boosted into a 600 km high polar orbit which enables it measure the size of the cloud particles, monitor the meteoric smoke influx, and observe the background of the mesosphere as well as the chemical make-up of the clouds. It should be noted that meteoric smoke, residuum of meteors that ablate in the thermosphere, is the most likely candidate for the seed particulate of the noctilucent clouds. As mentioned previously satellites have problems measuring this region. In particular the orbit of the AIM satellite is not stable so it will eventually plummet back to the Earth. Also its polar orbit means that as it revolves around the Earth it is constantly looking at different positions of the Earth, and crossing the Earth's equator at a different longitude during each revolution. Another problem with the AIM satellite is that, like other satellite projects and rockets, it is highly susceptible to funding issues and bureaucratic mismanagement. However, the wide field of view and the ability to observe the entire mesosphere makes satellite observations desirable.

LIDAR or **Li**ght **D**etection **a**nd **R**anging is one of the more ecumenical instruments because it has a wide range of use. LIDARs operate on the basis of using back-scattered

light to make observations. For noctilucent clouds, researchers use $Na$ or $K$ LIDAR. They use lasers which are tuned to backscatter off of sodium or potassium layers within the mesosphere. This scattered light is then used to obtain information on the NLCs. LIDAR are able to supply vertical resolution of the noctilucent clouds as well as 2d imaging. The main drawbacks to using LIDAR are their high initial costs as well as their operating costs.

# Chapter 4

# Converting Images

A photograph of the sky can be thought of as a projection of the sky onto a plane. The camera must do this to project the image onto its CCD and the goal of photogrammetry is to make an inverse projection. To do this the photograph has to be projected onto a reference plane. The most obvious plane to use is one that is tangent to the celestial sphere at the origin. This is the most obvious plane because the celestial sphere gives us a means of verifying the conversion. This plane-to-plane conversion can be expressed as

$$\begin{aligned} X &= \frac{x\cos\theta}{f} - \frac{y\sin\theta}{f} + xoffset \\ Y &= \frac{x\sin\theta}{f} - \frac{y\cos\theta}{f} + yoffset \end{aligned} \tag{4.1}$$

where $X$ and $Y$ are called the standard coordinates of the tangential plane, $x$ and $y$ refer to coordinates of the image as displayed on the camera's CCD and the $x$ and $y$-offsets refer to a displacement of the center of the camera's line of sight. The trigonometric functions multiplying the image coordinates account for any rotation of the camera axis. Given that 4.1 involves trigonometric functions, solving for $\theta$ and the $x$ and $y$-offsets can

be quite troublesome however 4.1 can be rewritten as

$$\begin{aligned} X &= ax + by + c \\ Y &= dx + ey + f \end{aligned} \tag{4.2}$$

to decouple the trigonometric functions into four separate constants. 4.2 is easier to solve numerically. These constants, the so-called plate constants, can be numerically verified by using the background star fields in a least squares fit. Once the standard coordinates are known the plane that is tangent to the celestial sphere can then be projected onto the celestial sphere. In principle, this coordinate transformation can be written as

$$\alpha = \alpha_0 + \arctan\left(\frac{X}{\cos\beta_0 + Y\sin\beta_0}\right) \tag{4.3a}$$

$$\beta = \arcsin\left(\frac{\sin\beta_0 - Y\cos\beta_0}{\sqrt[2]{1 + X^2 + Y^2}}\right) \tag{4.4a}$$

where $\alpha$ is the azimuthal angle and $\beta$ is the elevation angle of the image point corresponding to $X$ and $Y$ and the subscript 0 denotes the coordinates of the camera center. For more details on these transformations please see the appendix. With the topocentric coordinate system so-defined we can represent every image coordinate as a point on the Earth's surface with one final coordinate conversion. To do this we have to solve a spherical triangle to convert from azimuth and elevation to longitude and latitude.

Where $C$ represents the pole, $A$ represents the camera's location and $B$ represents an image point. Care must be taken to not confuse the spherical triangle with a planar triangle. In spherical trigonometry not only are the vertices angles, but so are the sides. Furthermore, the sum of the interior angles are not constrained to be $180\,^\circ$. The distance, $c$, from the camera to the image point's projection onto the Earth's surface is given by

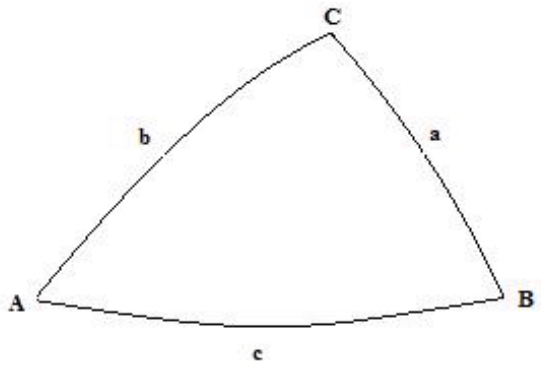


**Figure 4·1:** A typical spherical triangle where A, B, and C represent the angles of verticies and a, b, and c represent angular arc lengths.

$$c = \frac{\pi}{2} - \beta - \arcsin \frac{R \cos \beta}{R + h} \tag{4.5}$$

in Dalin(2004), where $\beta$ is the elevation angle of the point, $R$ is the Earth radius, and $h$ is the height of the image point above the Earth's surface. For noctilucent clouds $h$ can be assumed to be 83 km. $R$ is given by

$$R = \sqrt[2]{\frac{\left(a^2 \cos^2 \phi\right)^2 + \left(b^2 \sin^2 \phi\right)}{\left(a \cos \phi\right)^2 + \left(b \sin \phi\right)^2}} \tag{4.6}$$

where $a$ is the semi-major axis or equatorial radius and $b$ is the semi-minor axis or polar radius. $a$ was taken to be 6378.137 km and $b$ was 6356.7523 km. The radius was calculated for each observation site and treated as a constant for the entire image. For Rügen the latitude and longitude are, respectively, $54\,^\circ 7\,' 1.02\,''$ and $11\,^\circ 46\,' 19.54\,''$ and so the radius was calculated to be 6361.140 km. In principle the radius can be calculated to determine the latitudes and longitudes and those could be used iteratively to calculate better latitudes and longitudes however the radius of the Earth is not expected to

diverge much over the entire region and so such an iteration isn't necessary. If we choose $C$ to be the North Pole then

$$b = \frac{\pi}{2} - \phi_A \tag{4.7}$$

where $\phi_A$ is the latitude of the camera's position. This holds true because the spherical distance between a pole and any point is just the difference between their latitudes. Similarly we have

$$a = \frac{\pi}{2} - \phi_B \tag{4.8}$$

which we can use to find the latitude of the image point. The interior angles $A$ and $B$ respectively correspond to the azimuthal angles of the camera and projected image point. Because our spherical triangle uses the North Pole as a vertex the distance $C$ is also given by

$$C = \lambda_A - \lambda_B \tag{4.9}$$

where $\lambda$ is longitude. From this we can conclude that

$$\lambda_B = \lambda_A - C \tag{4.10}$$

Here care must be taken because none of our angles can be negative. When the quantity $\lambda_A - \lambda_B = 0$ then we know that both points have the same longitude. For negative values of $\lambda_B$ we know that the longitude of the image point is greater than that of the the camera. To handle this we can merely replace $A$ with $B$ or let $C$ be defined as

$$C = \lambda_B - \lambda_A \tag{4.11}$$

for any values of $C$ and $\lambda_A$ which yield negative values. Since we know $b$, $c$, $A$, and $B$ we can use the law of cosines for sides for a spherical triangle, namely

$$\cos a = \cos b \cos c + \sin b \sin c \cos A, \tag{4.12}$$

from which we can get $a$ by applying the inverse cosine to both sides of 4.12

$$a = \arccos\left(\cos b \cos c + \sin b \sin c \cos A\right). \tag{4.13}$$

We can find $C$ from a cyclical permutation of the law of cosines for sides. Given

$$\cos c = \cos a \cos b + \sin a \sin b \cos C \tag{4.14}$$

we can, after some algebra, write $C$ as

$$C = \arccos \frac{\cos c - \cos a \cos b}{\sin a \sin b}. \tag{4.15}$$

Therefore we can find the longitude and latitude of any point in our image. The longitudes can be converted into distances by

$$x = \lambda_B R \tag{4.16}$$

where $R$ is the radius of the Earth for the camera site and $\lambda_B$ is in radians. The latitudes can be converted into distances via

$$y = aR \cos a. \tag{4.17}$$

# Chapter 5

# Results

## 5.1 Plate Constants

The first set of noteworthy results is the plate constants. A different set of plate constants was determined for each camera location, namely Rügen and Kühlungsborn, Germany. Since only one night was considered in my analysis I only needed one set of plate constants for each camera location.

| | $a$ | $b$ | $c$ | $d$ | $e$ | $f$ |
|---|---|---|---|---|---|---|
| Rügen | 0.138270 | −0.00337485 | −0.00547696 | −0.00410211 | −0.137699 | 0.00655024 |
| Kühlungsborn | 0.138266 | −0.00530685 | 0.0645584 | −0.00689792 | −0.139025 | 0.104759 |

(5.1)

These plate constants were derived from a least squares solution to 4.2 where the stars were hand picked to minimize the sum of the residuals. The first thing to consider is whether or not these constants are capable of describing the image well enough to predict the positions of the stars that were used to find them.

As we see in Figure 5·1 the plate constants seem to match up pretty well with the actual star positions. The greatest difference between the actual and theoretical positions is around $10 pixels$. The plate constants are expected to be inaccurate near the borders because its trying to map spherical coordinates to planar ones. Near the borders of the image the curvature of the celestial sphere is more pronounced than in the center.

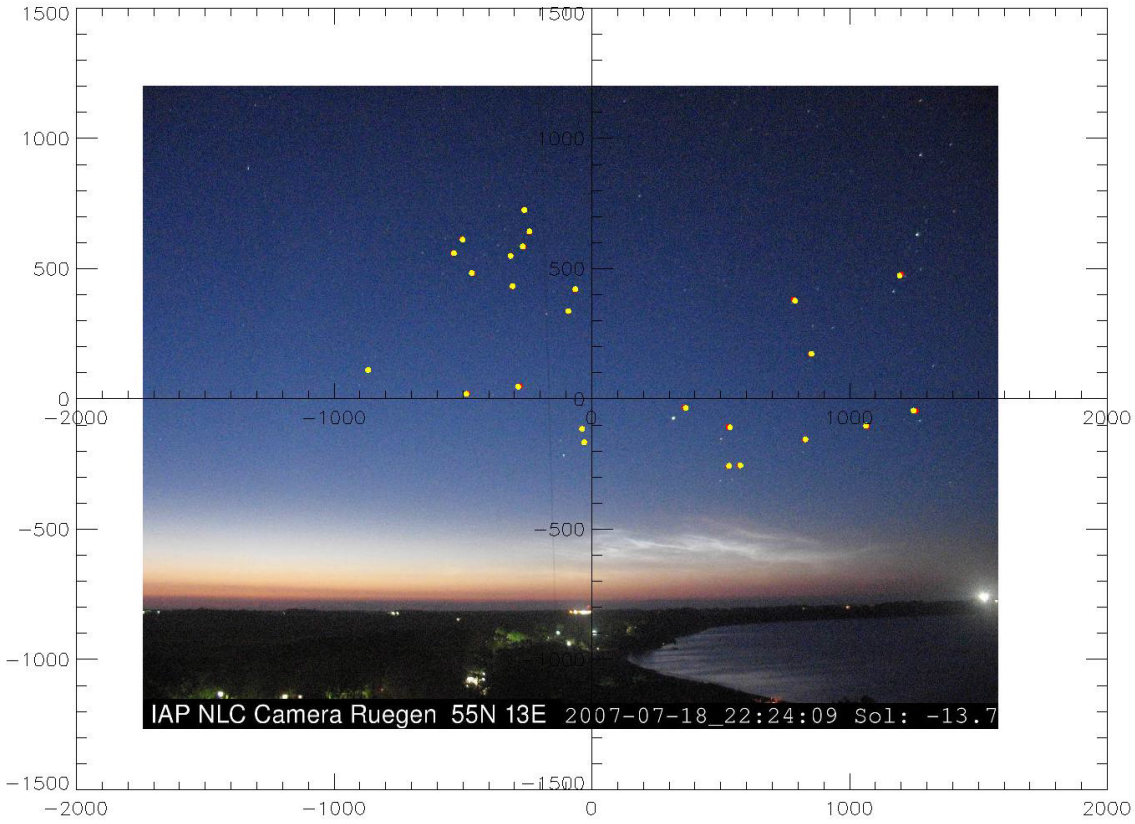


**Figure 5·1:** A photograph showing the actual star positions in red and the theoretical ones in yellow. The length scale is in pixels. Image courtesy of Gerd Baumgarten of IAP.

This coupled with a large field of view, about 60°, implies that the plate constants should be erroneous near the borders however the fit for Rügen doesn't seem to show this. Looking at the lower right-hand, fourth, quadrant we can see that theoretical position of $\epsilon$-Per, the rightmost star, is slightly off but the theoretical position its nearest neighbors, respectively 52-Per and 58-Per are more accurate. However if we look at the second, top left-most, quadrant we see a star near the origin,$\psi$1-Aur, whose theoretical position is slightly off while others in the immediate vicinity, $\psi$6-Aur which is further left and closer to the x-axis has a better match with its theoretical position. Indeed, the

left-most star, 22-Lyn, has a better match with its theoretical position than $\psi$1-Aur. These discrepancies could have developed because the number of stars in each quandrant is disproportionate, with the majority lying with quadrants two and four, respectively the top left-hand and bottom right-hand quadrants. On the other hand, adding in more stars near the periphery, from the lynx, camelopardalis, and perseus constellations, worsens the fit. Furthermore the lower quadrants have both NLC activity and the setting sun which makes it harder to see and identify more stars therein.

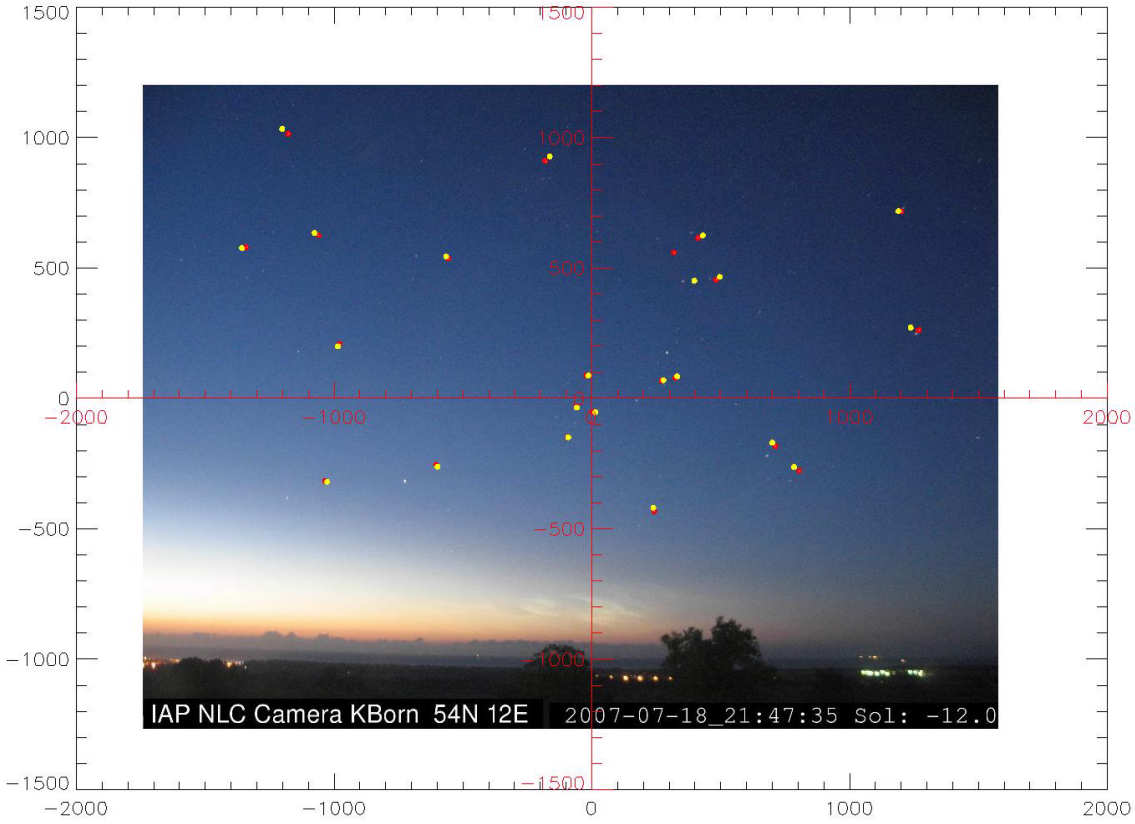


**Figure 5·2:** A photograph of a background star field with actual positions in yellow and calculated positions in red with a length scale in pixels. Image courtesy of Gerd Baumgarten of IAP.

As seen in the above photograph the plate constants do a decent job of describing

the image. However one position in particular is quite off, $\gamma$-Per in the first quadrant. The ordering and selection of stars for the least squares fit was done one at a time. Adding $\gamma$-Per without $\tau-$Per results in $\gamma$-Per's theoretical position being wrong by the same order that $\gamma$-Per's currently is. Aside from $\gamma$-Per the fit seems to produce a maximum difference of about $25 pixels$. $\gamma$-Per aside, the stars near the center seem to be more accurate than the ones in the periphery save for one in the first quadrant, 51-And. In and of itself the fit for Kühlungsborn doesn't seem remarkable until its plate constants are compared with the ones from the Rügen fit. The plate constants from the Kühlungsborn fit bear a remarkable resemblance to those from the Rügen fit except for the x and y-offsets. Recall that

$$c = \frac{xoffset}{F} \tag{5.2}$$

$$f = \frac{yoffset}{F} \tag{5.3}$$

and these offsets represent the offset of the center of the image from the origin of the plate constants. The other constants described a rotation of the camera with respect to the star field.

$$a = \frac{\cos\theta}{F} \tag{5.4}$$

$$b = -\frac{\sin\theta}{F} \tag{5.5}$$

$$d = \frac{\sin\theta}{F} \tag{5.6}$$

$$e = \frac{-\cos\theta}{F} \tag{5.7}$$

The agreement between $a$, $b$, $d$, and $e$ seem to indicate that both cameras have a

similar rotation with respect to their respective background star fields. If both cameras are aligned using the same technique then it's safe to assume that they should share a similar rotation angle. It is possible that a better fit for Kühlungsborn will produce more agreement with the Rügen plate constants however the plate seems to depend on the in which the star positions are applied and especially on the first three stars to be chose, namely the exact solution, as well as the concentration of stars used in the fit. A fit that starts off with points near the periphery seemed to be more accurate if more stars in the periphery are chosen than if I try to fill in the center. Similarly, a fit that starts in the center seems to be better at predicting the positions of stars near the center if I concentrate on stars near the center than near the periphery. Another reason for the discrepancy could be due to the number of stars used for the Kühlungsborn fit. However adding more seemed to worsen the fit. In the interest of time I decided to try the Kühlungsborn fit to see how far I could get with it.

Lastly the predicted rotation angles are worth comparing. Ideally 5.4 holds for all of the plate constants but the cosine is inaccurate for small angles and given the location of the horizon in the images we should expect any rotation to be quite small. Given that the focal length, $F$, is known to be 7.20 mm, the theoretical rotation angles for each plate constant are as follows

$$\arccos(aF) = 94.439\,\text{mrad} \tag{5.8}$$

$$\arcsin(-bF) = 2\,4.301\,\text{mrad} \tag{5.9}$$

$$\arcsin(dF) = -2\,9.531\,\text{mrad} \tag{5.10}$$

$$\arccos(-eF) = 130.99\,\text{mrad} \tag{5.11}$$

with the angles resulting from the inverse cosine being the largest angles. Given that the $b$ and $d$ have opposite signs, so do their resulting rotation angles. I'm at a loss to explain

the opposite signs from the arcsines aside from a sign error in 7.3. While $a$ and $-e$ yield numbers with the same sign and within the same ballpark, their resulting angles are too big, $5.410\,9^\circ$ for $a$ which should be noticeable for a field of view of approximately $60^\circ$. If we neglect the sign difference in the angles for $-b$ and $d$ then average the results we get a rotation angle of $\pm 26.920\,\text{mrad}$ or about $\pm 1.542\,4^\circ$. This is a reasonable result considering that the horizon appears relatively flat in the images from Rügen.

For Kühlungsborn we find

$$\arccos(aF) = 94.743\,\text{mrad} \tag{5.12}$$

$$\arcsin(-bF) = 38.219\,\text{mrad} \tag{5.13}$$

$$\arcsin(dF) = -49.685\ \text{mrad} \tag{5.14}$$

$$\arccos(-eF) = 44.268i\,\text{mrad} \tag{5.15}$$

Firstly the angle from $-e$ is imaginary. Upon closer inspection we find that $-eF = 1.0008$ which I take to indicate that $-eF = 1.0$ therefore the resulting angle is $0\,\text{mrad}$. Again the cosine of small angles is inaccurate so the inaccuracy could from that or it could come from bad plate constants. There is also a larger separation between the angles from $-b$ and $d$ and they still have opposite signs. Taking the average of the magnitudes we find that the rotation angle is $4.395\,2\,\text{mrad}$ or $2.518\,3^\circ$ which seems small enough to work. Still it's almost $1^\circ$ greater than the rotation angle found from the Rügen plate constants.

## 5.2 Projected Images

Figure 5·3 shows a photograph of the twilight sky taken from Rügen. This photograph shows a variety of noctilucent cloud formations. There isn't much of a veil in

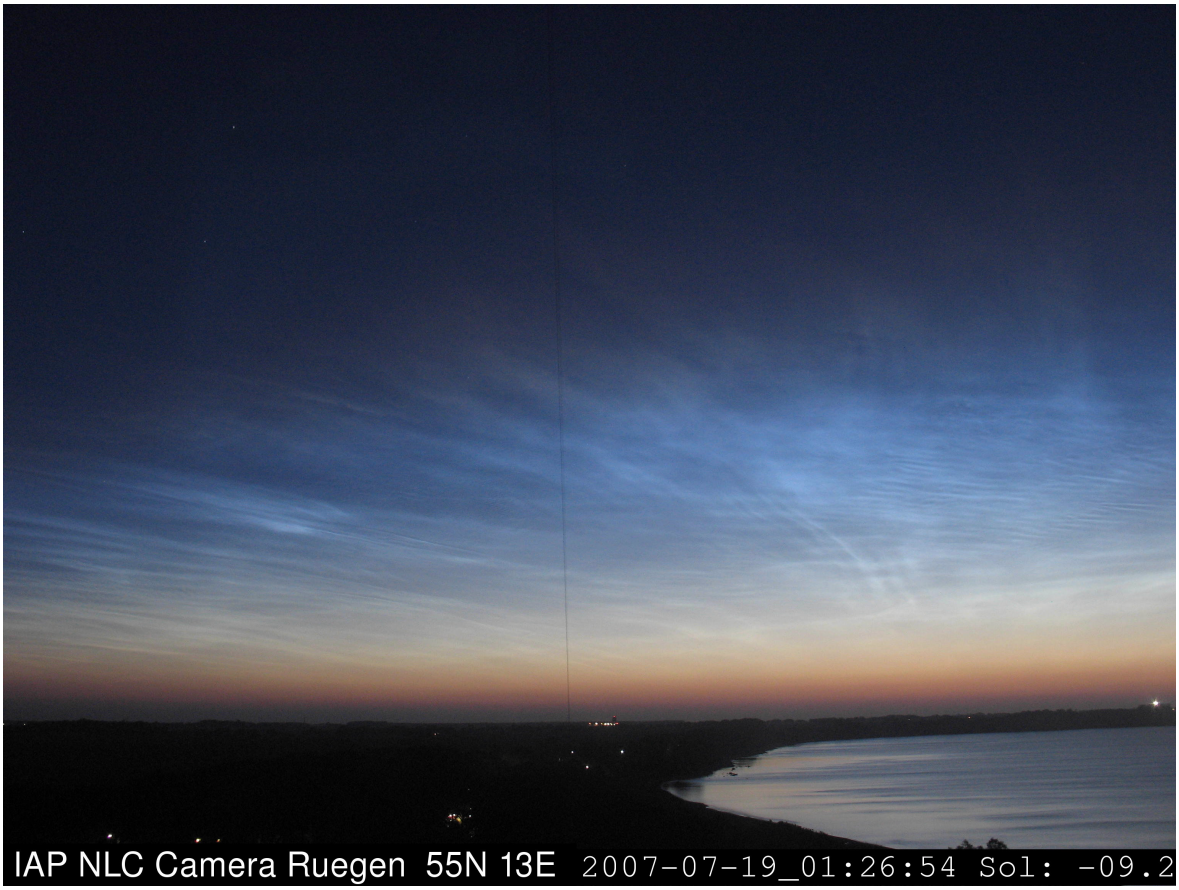


**Figure 5·3:** A photograph of the twilight sky from Rügen which shows a NLC field propagating southwards, courtesy of Gerd Baumgarten of IAP.

this image however there are bands and billows of different sizes. When this is mapped to the solution for the spherical triangle the resulting image is Figure 5·4, where the origin is fixed at the observation site and the majority of the horizon has been cut away and the length scale is in degrees from the origin. One of the first things to notice is that the x-axis has been flipped, as expected since this is a projection of the image onto the Earth's surface resulting in a mirror symmetry. Another thing to notice is that while the horizon in 5·3 is practically straight, however in the converted image it isn't. The image was clipped along the same height so if the rotation angle was 0 °, then the horizon in the converted image should be as well. Clearly there is some slight

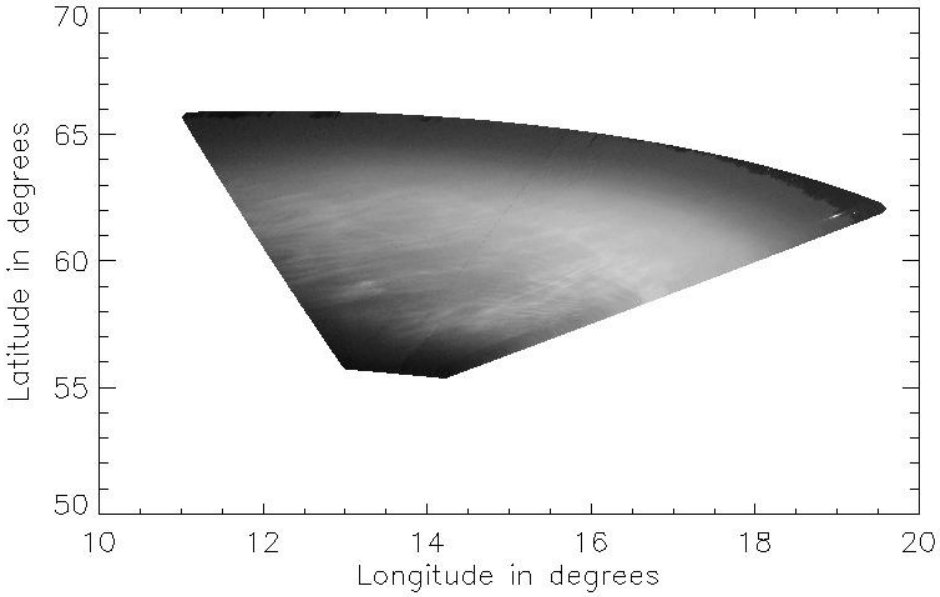


**Figure 5·4:** An image from Rügen which has been mapped onto the Earth's surface. The origin is centered at the camera's location in Rügen and the length scale is measured in degrees from the origin.

rotation in the image which could correspond to the $\pm 1.5424^\circ$ predicted by the plate constants. A curious feature about the horizon is that it vanishes near the center of the image but is apparent near the edges of the image.

Figure 5·5 shows an image taken from Kühlungsborn about a minute later than that of 5·3. The same features can be identified in each, billows, bands, and whirls. The converted image looks as follows
where the origin is the camera location in Kühlungsborn and the length scale is in degrees. In this image most of the horizon is gone except for a slight fragment on the far right side of the image. A similar conclusion could be made for Kühlungsborn except that there were a few scattered trees in the foreground of the image and that fragment could be from one such tree or it could be part of the weather from the foreground. To make a proper determination of the sign of the tilt angle the horizon cut off should be

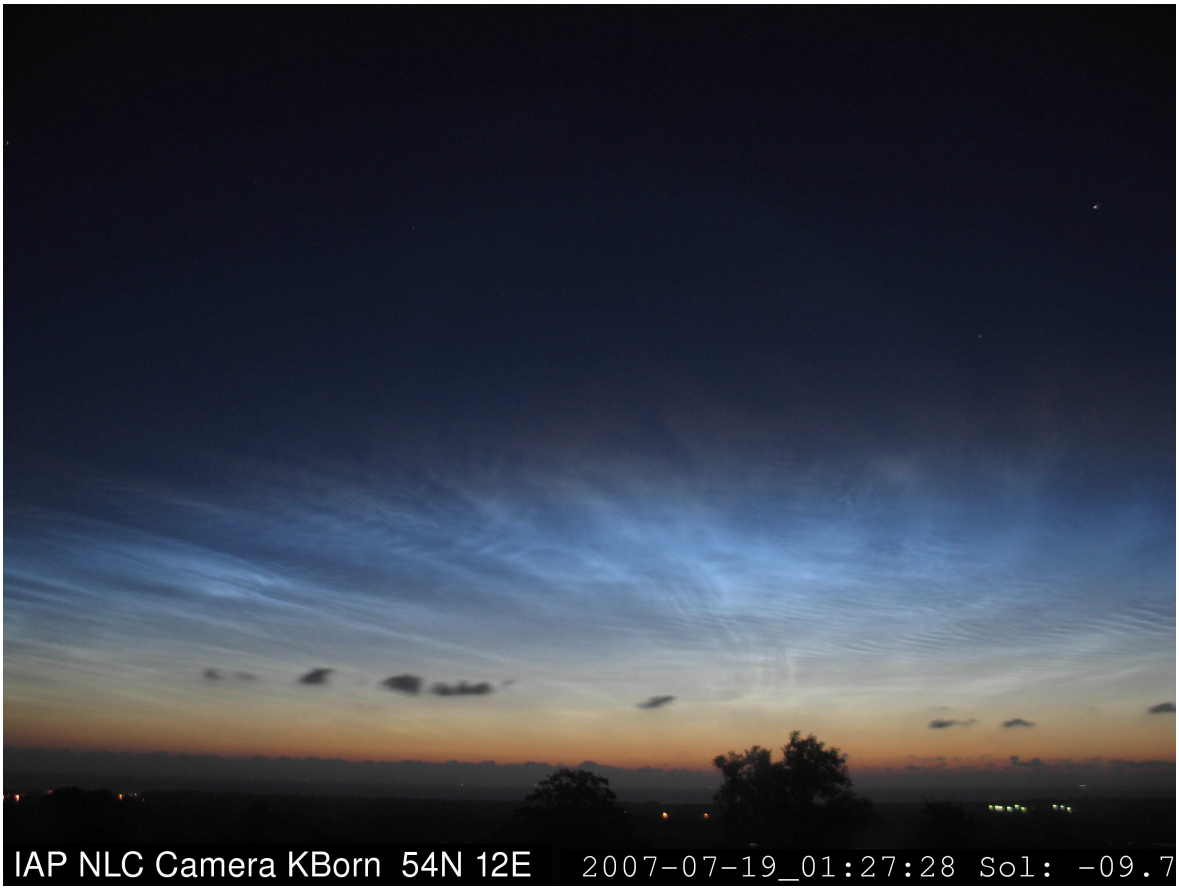


**Figure 5·5:** A photograph taken from Kühlungsborn showing a brillant NLC field, courtesy of Gerd Baumgarten of IAP.

lowered for this image.

Comparing the Rügen image to the Kühlungsborn image we find some of the same features in both images. Along the right of both images we can see some of the same band patterns. Near the origins we can see some of the same billow patterns however, some of the billow patterns present in the Rügen image seem to be absent from Kühlungsborn image and vice versa. This is most likely due to a double noctilucent cloud layer where the bottom layer is masking the lower layer. Also the contrast in the images could be screening some of billow patterns. The best way to test the plate constants is to see if the same features overlap the same part of the Earth.

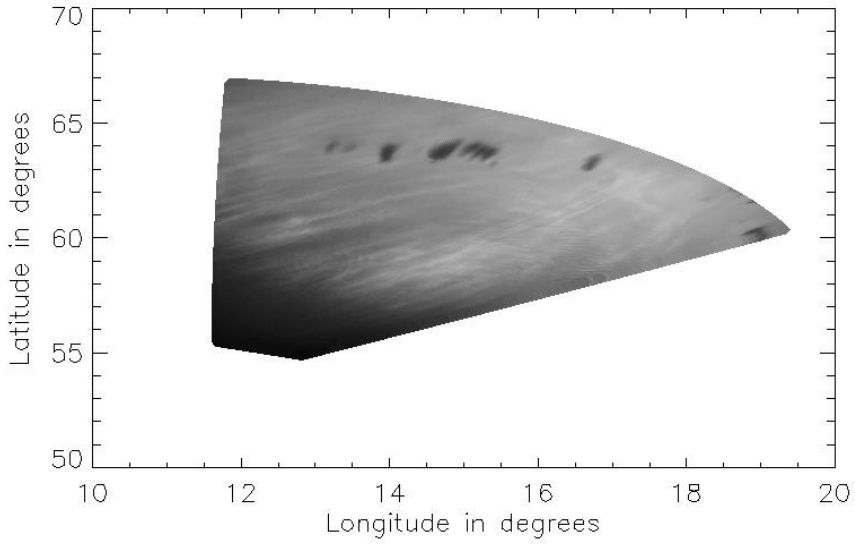


**Figure 5·6:** An image taken from Kühlungsborn and mapped onto the Earth's surface. The origin is centered at the camera's location and the length scale is in degrees from the origin, Kühlungsborn.

Here we have a section of Figure 5·4. The most notable features are the bands along the left side of the image as well as the veil-band structure in the bottom right corner of the image. If we look at the same features in the converted image of Kühlungsborn we have where we can identify the same features. Instantly one notices that this image appears more tilted than the one from Rügen. Also the bands in the left-side of the image appear one degree of latitude higher in the Kühlungsborn image. At first glance, it seems that this could be a result of the plate constants, but when the original images, Figure 5·3 and Figure 5·5, are compared it is apparent that the bands appear more slanted in the Kühlungsborn image. It seems more likely that the plate constants are causing a disparity in the location of the occidental bands but this is also at the edge of the image, where the curvature of the celestial sphere is the greatest, and thus the plate constants are expected to be less accurate here. As the images were taken roughly thirty seconds apart, the features aren't expected to move much. Figure 5·9 shows a section of an

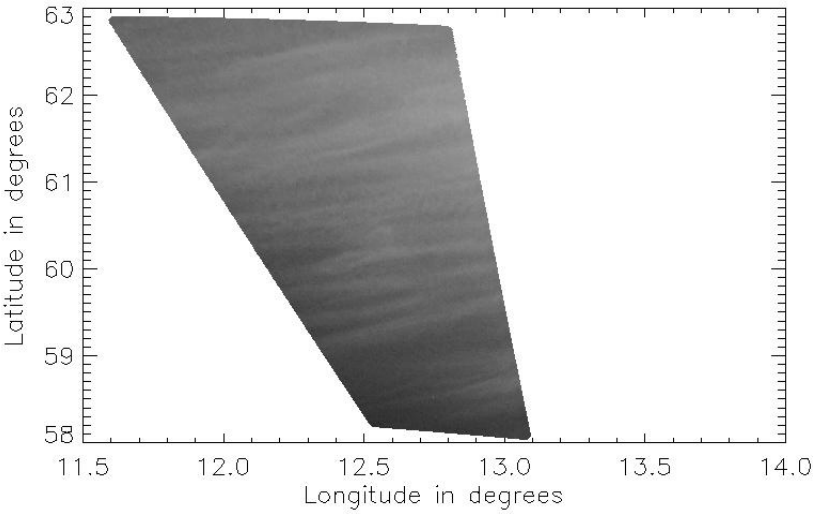


**Figure 5·7:** A section of the converted image that was taken from Rügen. The most notable features are the bands near the left edge of the image and the veil-band structure in the bottom right corner.

image that was taken from Rügen at a later time than the previous one, 1:42:42 universal time. In this image, we see billow patterns throughout with a veil in the bottom-left corner of the image with the bottom-most feature circled. Figure 5·10 shows the same features as in the image taken from with the matching feature circled. In the image taken from Rügen the billow is has a longitude of about 14.45° while in the image taken from Kühlungsborn it appears at 14.2°. Comparing latitudes, we see that the billow is at 57.1° in the Rügen image, but at 57.9° in the image from Kühlungsborn. Since the photographs were taken only eight seconds apart, their positions are not expected to diverge much. While the longitudes are quite close, the latitudes are some 0.8° apart. This could be due to the plate constants for Kühlungsborn or due to differences in atmospheric refraction from the two camera sites, however it is small enough to be neglected for the time being. My methodology seems capable of locating the same feature with an error of approximately ±0.125° longitude and ±0.5° latitude near the center of the image.

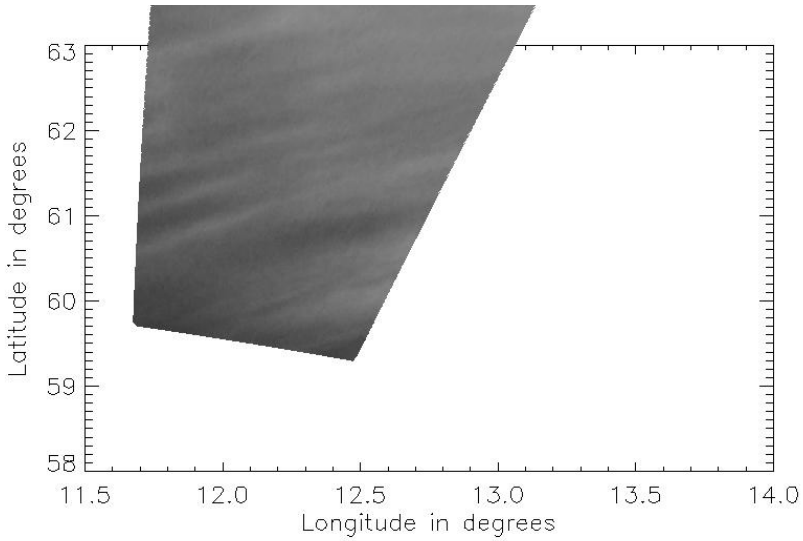


**Figure 5·8:** A section of a NLC field seen from Kühlungsborn. The image has been mapped to the Earth's surface.

## 5.3 Fourier Analysis

To describe the wave packets with wavelengths in meters instead of degrees the longitudes and latitudes must be converted into meters. The longitudes can be converted as follows

$$x = (\lambda - \lambda_c)\, R_e \tag{5.16}$$

where $R_e$ is the radius of the Earth in kilometers and $\lambda_c$ is the longitude of the camera site. Similarly, the latitudes can be converted as follows

$$y = (\phi - \phi_c)\, R_e \cos\phi \tag{5.17}$$

where the term $\cos\phi$ is used because lines of different latitudes don't lie on the same great circle. Given the above, the images from Rügen and Kühlungsborn can be mapped onto a grid in terms of the distances that the image points are from their

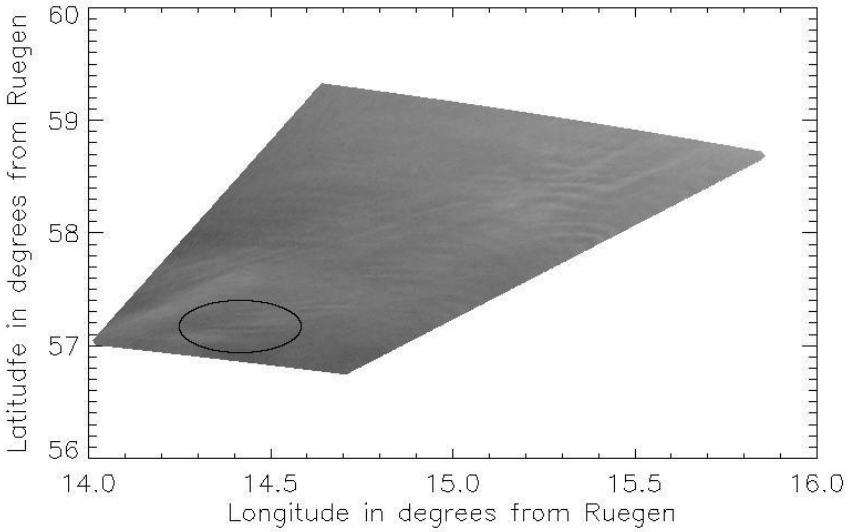


**Figure 5·9:** A section of an image from Rügen,taken at 1:42:42 universal time, that was mapped to the Earth's surface.

respective camera sites. In a typical Rügen image we have where the northwards extent is about 1375 km and the east-west extent is about 950 km. For Kühlungsborn we have where we can see a larger northward extent of just under 1400 km and a east-west, or zonal, extent of approximately 900 km. From such plots we can deduce wavelengths either by directly measuring or by the Fast Fourier Transform, FFT.

Looking at the power spectrum of a set of bands near the periphery we find where the object of the FFT is shown, boxed-in, in Figure 5·14. At first sight there doesn't appear to be anything in the power spectrum aside from some noise, but after the mean value of the image is subtracted from the image, to reduce the noise, our power spectrum becomes Figure 5·15, where a band appears at the value $k_y \approx 0.065\,\mathrm{km}^{-1}$. This is the wavenumber in the north-south, or zonal, direction, and it corresponds to a wavelength of about 15.4 km. The band of constant $k_y$ indicates that this wave only propagates meridionally. A wavelength of this magnitude seems to indicate the either Kelvin-Helmholtz instability or the presence of an internal gravity wave. It was

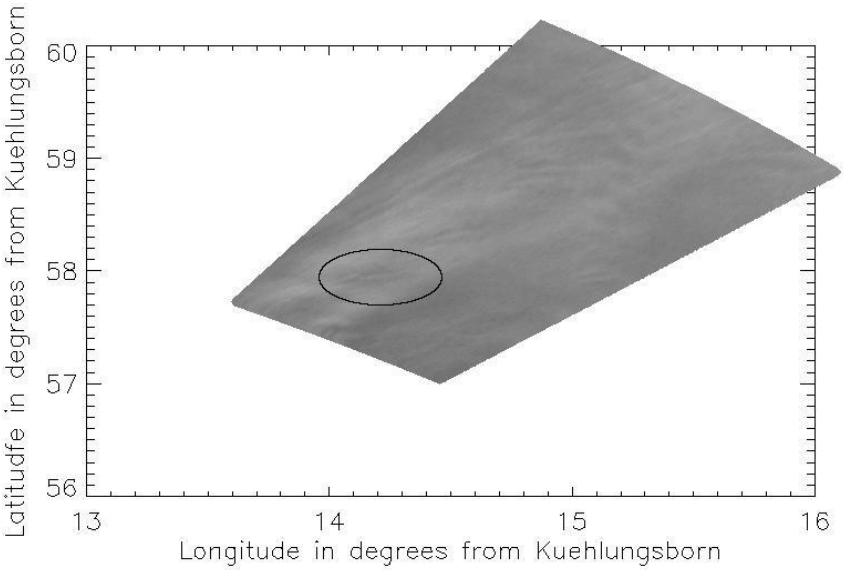


**Figure 5·10:** A section of an image taken from Kühlungsborn, at 1:42:50 universal time, and mapped onto the Earth's surface.

suggested by Grishin(**??**) that small and medium waves, wavelengths between 5 km and 50 km, are typically caused by Kelvin-Helmholtz instabilities while large scale wave patterns, wavelengths greater than 100 km are caused by internal gravity waves. However, assuming a Kelvin-Helmholtz instability for a wavelength of 28 km, the wind speeds of the layers must diverge by more than $200\,\mathrm{m\,s^{-1}}$(*GadsenandSchrder*1989). For the mesopause region this is very unlikely therefore, gravity waves are the likely sources for any medium to large scale waves. Without vertical resolution there is no way to determine whether this is a Kelvin-Helmholtz instability or a small wavelength gravity wave. Looking at a different region of the NLC field some bands can be identified. In Figure 5·16 we see a set of bands which has both a meridional and zonal component. The meridional wavelength as per the band at $k_x \approx 0.02\,\mathrm{km^{-1}}$ which corresponds to a wavelength of 50 km however, the FFT doesn't say anything about the zonal component. Visually, we can see that the zonal component of the wavelength is also around 50 km which corresponds to a wavenumber of approximately $0.02\,\mathrm{km^{-1}}$. For this case an

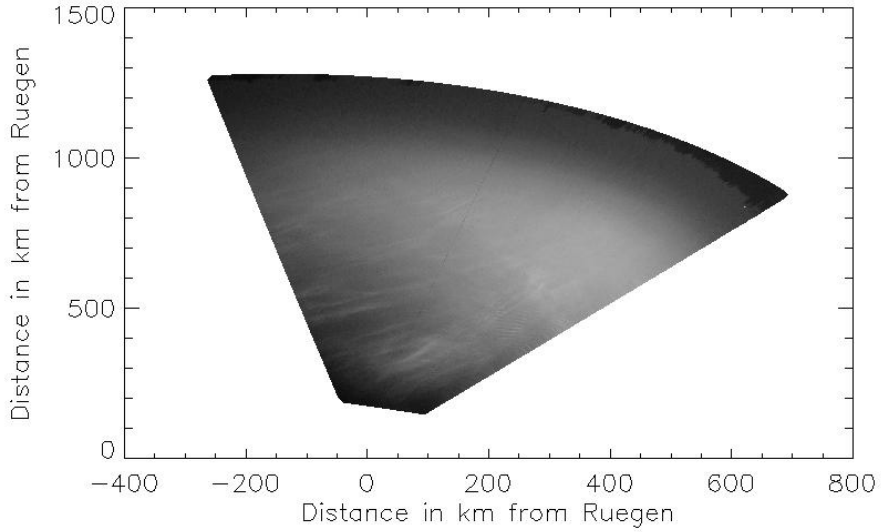


**Figure 5·11:** An image taken from Rügen that is shown on a kilometer grid.

internal gravity wave is the most likely culprit.

Phase velocities can be determined by measuring the displacement of the wave packets over time. In principle the phase velocity of the wave is augmented by the windspeed. Consequently the actual phase velocity of the wave packet is the difference between the wave's phase velocity and the windspeed, however measuring the mean windspeed of a noctilucent cloud system using photogrammetric methods can be difficult because most veils travel with band systems. Veils represent the only variety of NLC which are not affected by waves, thus they act as a natural tracer for the system.
If we compare the location of the billow pattern in Figure 5·18 and Figure 5·19 we find that the packets have moved approximately 40 km in the meridional direction and 20 km in the zonal direction. Given that the images were taken some fifth-teen minutes and six seconds apart its apparent phase velocity is about $44\,\mathrm{m\,s^{-1}}$meridionally and $22\,\mathrm{m\,s^{-1}}$ zonally, however the wave doesn't modulate meridionally. The meridional motion is indicative of the actual windspeed in display. Because small wave structures are known

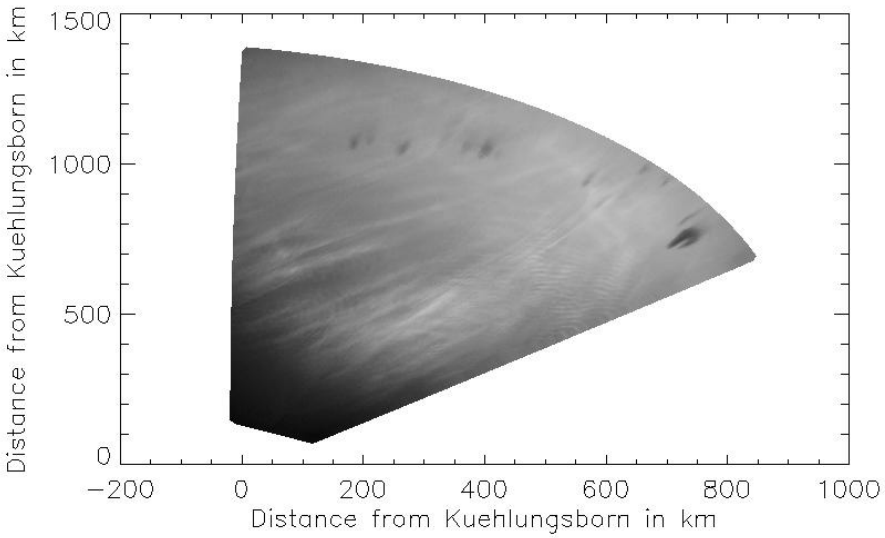


**Figure 5·12:** An image taken from Kühlungsborn that has been plotted on an x-y kilometer grid.

to move with the mean wind while the larger waves may even move opposite to the mean wind. The packet in 5·18 corresponds to the same packet observed in 5·15, a field with a wavelength of 16.5 km.

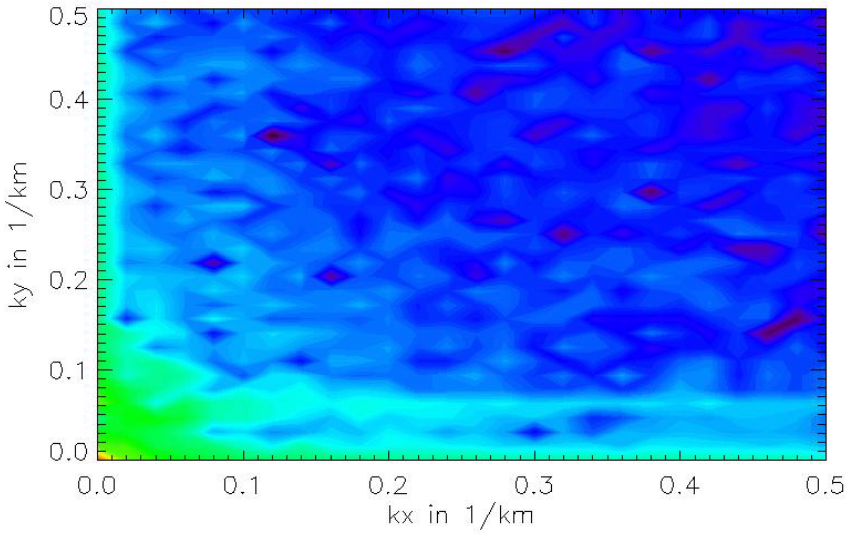


**Figure 5·13:** A contour plot of the power spectrum of a section of billow pattern.

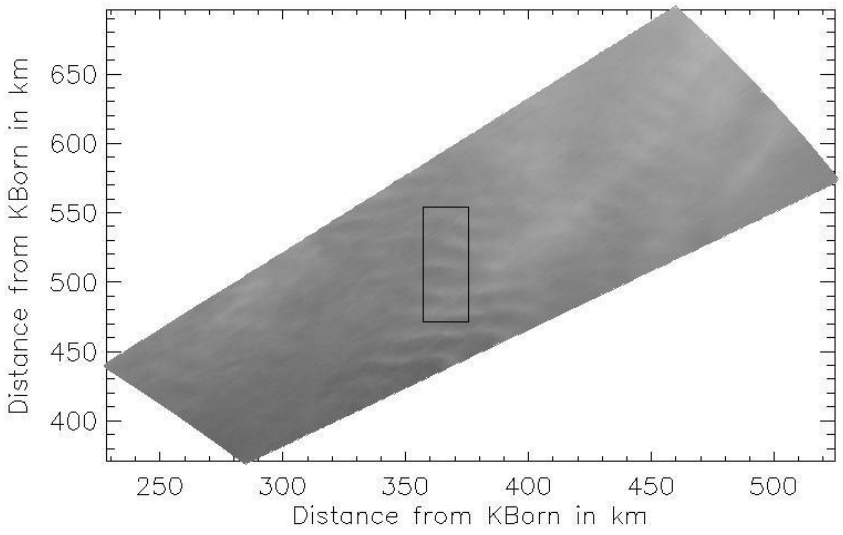


**Figure 5·14:** A cutout of a converted Kühlungsborn image.

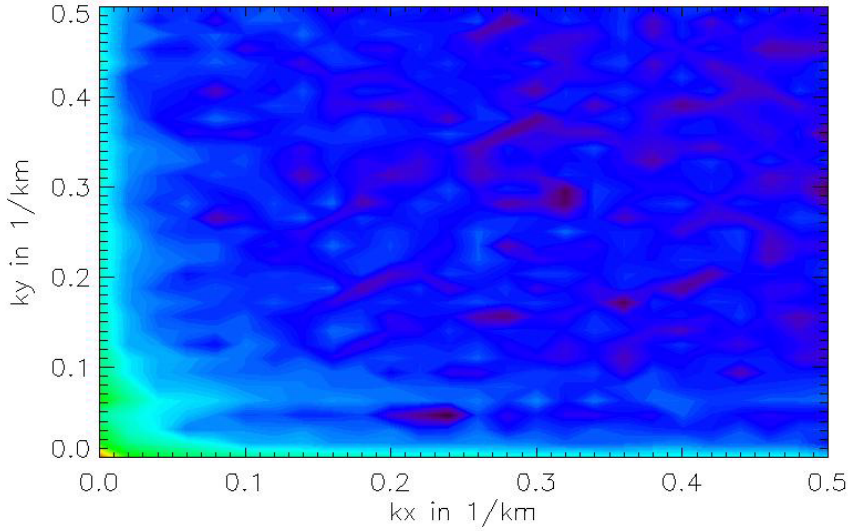


**Figure 5·15:** The power spectrum of a NLC wave packet from Kühlungsborn that has been filtered to remove some of the noise. The object of the FFT is in the lower left part of the image.

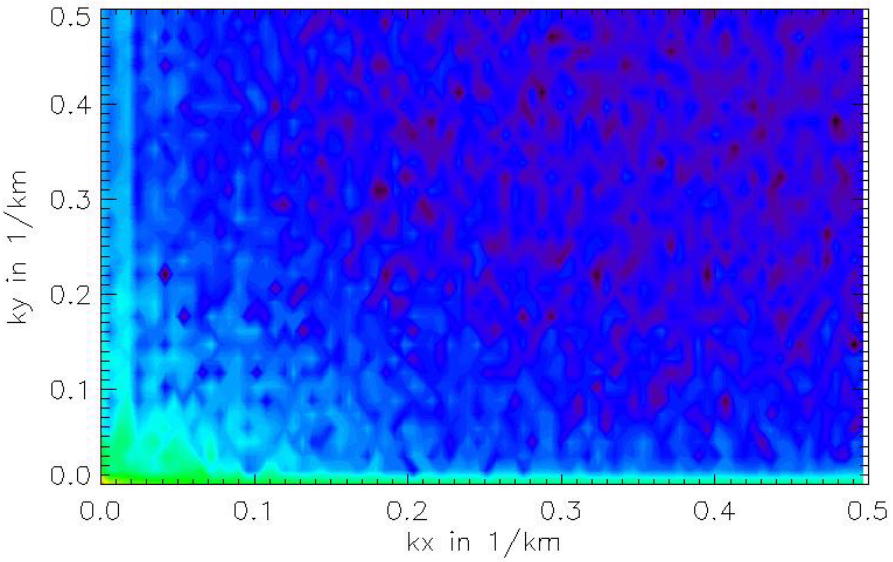


**Figure 5·16:** The power spectrum of a cloud field, taken from Kühlungsborn, which has a meridional wave packet.

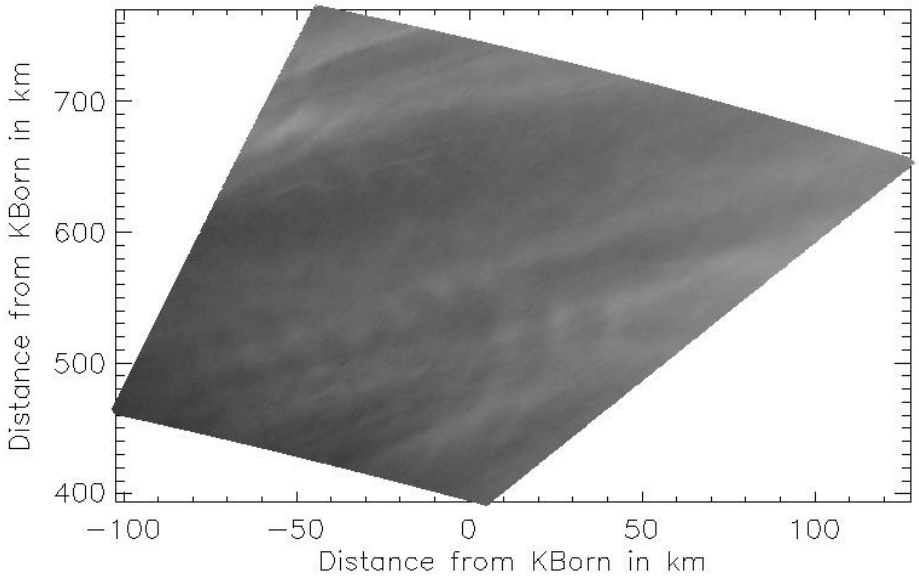


**Figure 5·17:** A cutout of a converted image from Kühlungsborn showing a wave with a 50 km wavelength.

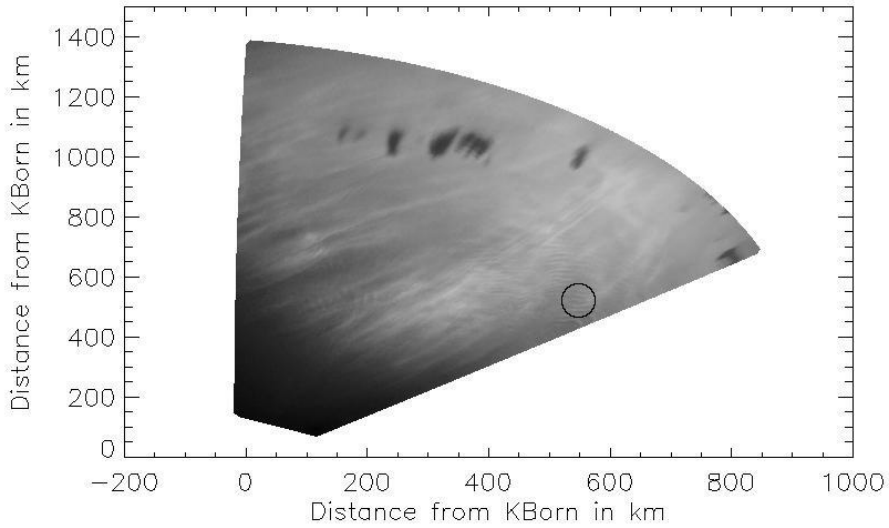


**Figure 5·18:** An image from Kühlungsborn taken, at 1:27:28 UT, with a wave packet encircled.

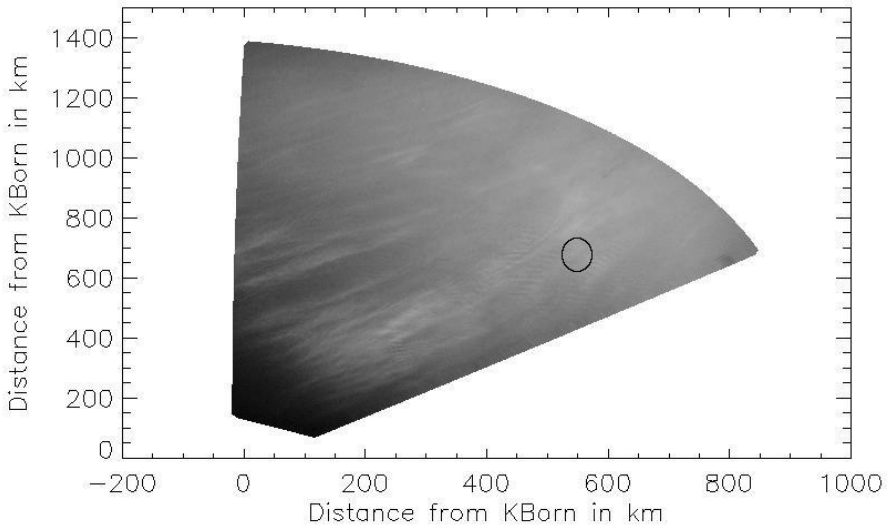


**Figure 5·19:** An image from Kühlungsborn, take at 1:42:34 UT, with a wave packet encircled.

# Chapter 6

# Conclusion

The simultaneous observations of a noctilucent cloud display from 19 July 2007 has been considered to determine the dynamics therein. Using time lapsed photographs taken from two observation sites, Rügen and Kühlungsborn, Germany, and supplied by Gerd Baumgarten of the Lebiniz Institut für Atmosphärenphysik, a photogrammetric analysis was employed which revealed gravity waves and Kelvin-Helmholtz instabilities within the system. Such an analysis can be used, as is, to unravel similar dynamics within future displays or extended to include a vertical resolution to not only pinpoint the altitudes of certain features, but to also properly identify the Kelvin-Helmholtz instabilities.

Having a multiple camera system in place solely for the observation of noctilucent clouds allows for a photogrammetric analysis to be carried out regularly, as the weather allows for the observation of the clouds. Wave parameters can be readily identified and used to characterize the NLC field because the plate constants should be identical for their respective sites as long as the cameras aren't moved. The knowledge of typical wave parameters allows for a quick means of identifying Kelvin-Helmholtz instabilities and internal gravity waves. This could then be extended by triangulation to reveal the vertical structure within the noctilucent cloud layer.

Herein, the plate constants were calculated to describe the NLC image in both the right-ascension and the horizon coordinate systems. These transformations allowed the sky to be mapped onto the Earth's surface, thus allowing the calculation of image points

via spherical trigonometry. The precision of the two sets of plate constants was determined, by comparing the respective positions of a single feature near the center of the images, to be $\pm 0.125\,^\circ$ longitude and $\pm 0.5\,^\circ$ latitude. Additionally, the plate constants seem to be internally consistent as per the rotation angles that they predicted, $\pm 1.542\,4\,^\circ$ for Rügen and $\pm 2.518\,3\,^\circ$ for Kühlungsborn. Consequently, the horizon of the Rügen images isn't uniformly along the periphery which could be a relic of the rotation angle or a consequence of the far right side of the image being closer to the camera than the far left side. Furthermore, the plate constants for the two sites are expected to be similar if the cameras used are identical and if they are aligned by the same person or methodology.

Having the sky mapped to the Earth's surface enabled wave parameters to be measured and classified based on typical results. A billow pattern with waves of 16.5 km and $22\,\mathrm{m\,s^{-1}}$ apparent phase speed were identified. The size of the wavelength attests to it being a Kelvin-Helmholtz instability or a small wavelength gravity wave. Another billow pattern of wavelength 50 km was recognized. The most likely source for such a wavelength is an internal gravity wave. Furthermore, the billow pattern of wavelength 16.5 km was found to move both zonally and meridionally. As the wave has no modulation in the meridional direction, the $44\,\mathrm{m\,s^{-1}}$ must be part of the mean windspeed for the entire system. It is well known that small waves move with the mean wind while the larger waves can even move opposite to the wind. It is likely that the phase speed is the zonal component of the mean windspeed, however the flow is expected to be mostly zonal in this region, flowing from the pole to the equator. An assay of more wave packets with similar motions would indicate that the phase speed of these waves is in fact the mean windspeed.

This analysis can be extended to the band structures within the noctilucent cloud field and to measure the frequency within some of the more interesting wave structures.

# Chapter 7

# Appendix: Coordinate Transformations

## 7.A Image Coordinates and Standard Coordinates

Cameras make a projection of a three-dimensional space onto a two-dimensional object, namely their CCD or film and the aim of photogrammetry is to do an inverse projection. However a direct inversion isn't possible unless there is some sort of foreknowledge that helps determine one of the three dimensions in question. But when there are pictures of the sky then there are bound to be stars in the background and they give us a reference coordinate system. These stars are on the celestial sphere and so their positions can be projected radially downwards onto any sphere. Therefore the goal is to relate these two coordinate systems, the image and celestial coordinate systems. To do this we need an intermediate coordinate system relating the surface of a sphere to a two-dimensional plane and so we use a plane that is tangent to the celestial sphere. We call this coordinate system the standard coordinate system.

For a perfectly aligned camera the transformation from image coordinates to standard coordinates is very straightforward. For coordinate systems with the origin at the center the transformation becomes

$$\begin{aligned} X &= \frac{x}{f} \\ Y &= \frac{y}{f} \end{aligned} \tag{7.1}$$

where "$X$" and "$Y$" represent standard coordinates, "$x$" and "$y$" represent image coordinates and $f$ is the focal length. The image coordinates are scaled by the focal length to make the standard coordinates dimensionless and so both the image coordinates and the focal length are in millimeters. However experiments are rarely perfect and in our case we have to account for the camera being rotated as well as offset. The rotation is easily described by a standard two-dimensional rotation matrix and so the transformation becomes

$$\begin{aligned} X &= \frac{x\cos\theta}{f} + \frac{y\sin\theta}{f} \\ Y &= \frac{x\sin\theta}{f} + \frac{y\cos\theta}{f} \end{aligned} \tag{7.2}$$

To handle the offsets in the $X$ and $Y$ directions our equations become

$$\begin{aligned} X &= \frac{x\cos\theta}{f} - \frac{y\sin\theta}{f} + xoffset \\ Y &= \frac{x\sin\theta}{f} - \frac{y\cos\theta}{f} + yoffset \end{aligned} \tag{7.3}$$

## 7.B Celestial Coordinates

To express the image coordinates in terms of the celestial coordinates we have to apply vector algebra to the geometry of our system. The standard procedure for describing a plane that is tangent to a surface is to parametrize the surface vector as a function of two variables. Then we find a normal to this surface by first finding two vectors in the tangent plane and then taking their cross product, which is tangent to both the surface and the plane. The surface in question is the unit sphere and so the surface vector is just

$$\mathbf{P} = \sin\alpha\cos\beta\mathbf{i} + \cos\alpha\cos\beta\mathbf{j} + \sin\beta\mathbf{k} \tag{7.4a}$$

Where $\alpha$ and $\beta$ represent, respectively, the azimuth and elevation angles of the image point in question. The elevation angle is aligned with the $Y$ axis and the azimuth angle is aligned with the $X$ axis. To determine the tangent vectors we make use of the derivative. If we keep one of the parameters constant, say $\alpha$, and take the derivative of the surface vector we get a tangent vector at the point of tangency defined by the azimuth and elevation angles of the camera center, respectively $\alpha_0$ and $\beta_0$. Therefore our tangent vectors are simply the partial derivatives of $\mathbf{P}$, namely

$$\begin{aligned} \mathbf{P}_\alpha &= \cos\alpha\cos\beta\mathbf{i} - \sin\alpha\cos\beta\mathbf{j} \\ \mathbf{P}_\beta &= -\sin\alpha\sin\beta\mathbf{i} - \cos\alpha\sin\beta\mathbf{j} + \cos\beta\mathbf{k} \end{aligned} \tag{7.5}$$

To find the normal vector to our surface and tangent plane evaluated at the camera center we take the cross product of $\mathbf{P}_\beta$ and $\mathbf{P}_\alpha$ where the order was chosen such we have an outward pointing normal of

$$\mathbf{n} = \mathbf{P}_\beta \times \mathbf{P}_\alpha = \cos^2\beta\sin\alpha\mathbf{i} + \cos\alpha\cos^2\beta\mathbf{j} + \left(\cos\beta\sin\beta\cos^2\alpha + \cos\beta\sin\beta\sin^2\alpha\right)\mathbf{k} \tag{7.6}$$

Which, with the use of the well known trigonometric identity $\sin^2\theta + \cos^2\theta = 1$, can be reduced to

$$\mathbf{n} = \cos^2\beta\sin\alpha\mathbf{i} + \cos\alpha\cos^2\beta\mathbf{j} + \cos\beta\sin\beta\mathbf{k} \tag{7.7a}$$

Now we want to characterize the tangent plane in terms of $X$ and $Y$. To do this we make use of the fact that the dot product of two vectors, $\mathbf{a}$ and $\mathbf{b}$, can be interpreted as the scalar projection of $\mathbf{b}$ onto $\mathbf{a}$ multiplied by the length of $\vec{a}$.
(insert dot product Figure)That is

$$\mathbf{a} \cdot \mathbf{b} = S_P \left|\mathbf{a}\right| \tag{7.8}$$

where

$$S_P = \left|\mathbf{b}\right| \cos\theta \tag{7.9}$$

and $\theta$ is the angle between $\vec{a}$ and $\vec{b}$. If we use the two vectors lying in the tangent plane, $\vec{P}_\alpha$ and $\vec{P}_\beta$, and the surface vector of the celestial sphere then $S_P$ is just the scalar projection of our vector onto the tangent plane, namely our standard coordinates $X$ and $Y$. Lets take $\vec{P}_\alpha$ evaluated at the point of tangency first.

$$S_{P1} = \frac{\mathbf{P}_\alpha \cdot \mathbf{P}}{\left|\mathbf{P}_\alpha\right|} = \frac{(\cos\alpha_0 \cos\beta_0 \mathbf{i} - \sin\alpha_0 \cos\beta_0 \mathbf{j}) \cdot (\sin\alpha\cos\beta\mathbf{i} + \cos\alpha\cos\beta\mathbf{j} + \sin\beta\mathbf{k})}{\left|(\cos\alpha_0 \cos\beta_0 \hat{\imath} - \sin\alpha_0 \cos\beta_0)\right|} \tag{7.10a}$$

$$S_{P1} = \frac{\cos\alpha_0 \cos\beta_0 \sin\alpha\cos\beta - \sin\alpha_0 \cos\beta_0 \cos\alpha\cos\beta}{\sqrt[2]{\cos^2\beta_0 \left(\cos^2\alpha_0 + \sin^2\alpha_0\right)}} \tag{7.10b}$$

$$S_{P1} = \frac{\cos\beta_0 \cos\beta \left(\sin\alpha\cos\alpha_0 - \cos\alpha\sin\alpha_0\right)}{\cos\beta_0} = \cos\beta\sin\left(\alpha - \alpha_0\right) \tag{7.10c}$$

Where we made use of the identity $\sin\theta\cos\phi - \cos\theta\sin\phi = \sin\left(\theta - \phi\right)$. If we try the same routine with $\mathbf{P}_\beta$ we have

$$S_{P2} = \frac{\mathbf{P}_\beta \cdot \mathbf{P}}{|\mathbf{P}_\beta|} = \frac{(-\sin\alpha_0 \sin\beta_0 \mathbf{i} - \cos\alpha_0 \sin\beta_0 \mathbf{j} + \cos\beta_0 \mathbf{k}) \cdot (\sin\alpha\cos\beta\mathbf{i} + \cos\alpha\cos\beta\mathbf{j} + \sin\beta\mathbf{k})}{\left|-\sin\alpha_0 \sin\beta_0 \hat{\imath} - \cos\alpha_0 \sin\beta_0 \hat{\jmath} + \cos\beta_0 \hat{k}\right|} \tag{7.10d}$$

$$S_{P2} = \frac{-\sin\alpha_0 \sin\beta_0 \sin\alpha\cos\beta - \cos\alpha_0 \sin\beta_0 \cos\alpha\cos\beta + \cos\beta_0 \sin\beta}{\sqrt[2]{\sin^2\alpha_0 \sin^2\beta_0 + \cos^2\alpha_0 \sin^2\beta_0 + \cos^2\beta_0}} \tag{7.10e}$$

$$S_{P2} = \frac{-\sin\beta_0 \cos\beta\left(\sin\alpha\sin\alpha_0 + \cos\alpha_0\cos\alpha\right) + \cos\beta_0\sin\beta}{\sqrt[2]{\sin^2\beta_0\left(\sin^2\alpha_0 + \cos^2\alpha_0\right) + \cos^2\beta_0}} \tag{7.10f}$$

$$S_{P2} = \frac{\cos\beta_0 \sin\beta - \sin\beta_0 \cos\beta\cos\left(\alpha - \alpha_0\right)}{\sqrt[2]{\sin^2\beta_0 + \cos^2\beta_0}} \tag{7.10g}$$

$$S_{P2} = \cos\beta_0 \sin\beta - \sin\beta_0 \cos\beta\cos\left(\alpha - \alpha_0\right) \tag{7.11a}$$

Where we made use of the trigonometric identity $\cos(\theta - \phi) = \cos\theta\cos\phi + \sin\theta\sin\phi$. Now we only need to scale $S_{P1}$ and $S_{P2}$ to define the tangent plane in terms of the azimuth and elevation angles, namely by the distance between a point on the plane and the celestial sphere. Where this distance is just the magnitude of the scalar projection the vector $\mathbf{c}$ onto the normal vector. Where $\mathbf{c}$ is simply the position vector of the point. But any position vector space can be represented in spherical coordinates as simply

$$\mathbf{c} = \sin\alpha\cos\beta\mathbf{i} + \cos\alpha\cos\beta\mathbf{j} + \sin\beta\mathbf{k} \tag{7.11b}$$

$$D = \frac{|\mathbf{n}\cdot\mathbf{c}|}{|\mathbf{n}|} = \frac{\left|\left(\cos^2\beta_0\sin\alpha_0\mathbf{i} + \cos\alpha_0\cos^2\beta_0\mathbf{j} + \cos\beta_0\sin\beta_0\mathbf{k}\right)\cdot\left(\sin\alpha\cos\beta\mathbf{i} + \cos\alpha\cos\beta\mathbf{j} + \sin\beta\mathbf{k}\right)\right|}{\left|\cos^2\beta_0\sin\alpha_0\hat{\imath} + \cos\alpha_0\cos^2\beta_0\hat{\jmath} + \cos\beta_0\sin\beta_0\hat{k}\right|} \tag{7.11c}$$

$$D = \frac{\left|\cos^2\beta_0\sin\alpha_0\sin\alpha\cos\beta + \cos\alpha_0\cos^2\beta_0\cos\alpha\cos\beta + \cos\beta_0\sin\beta_0\sin\beta\right|}{\sqrt[2]{\cos^4\beta_0\sin^2\alpha_0 + \cos^2\alpha_0\cos^4\beta_0 + \cos^2\beta_0\sin^2\beta_0}} \tag{7.11d}$$

$$D = \frac{\left|\cos\beta_0\left[\left(\cos\beta_0\cos\beta\right)\left(\sin\alpha_0\sin\alpha - \cos\alpha\cos\alpha_0\right) + \sin\beta_0\sin\beta\right]\right|}{\sqrt[2]{\cos^2\beta_0\left(\cos^2\beta_0\left[\sin^2\alpha_0 + \cos^2\alpha_0\right] + \sin^2\beta_0\right)}} \tag{7.11e}$$

$$D = \frac{\left|\cos\beta_0\right|\left|\cos\beta_0\cos\beta\cos\left(\alpha - \alpha_0\right) + \sin\beta_0\sin\beta\right|}{\left|\cos\beta_0\right|\sqrt[2]{\cos^2\beta_0 + \sin^2\beta_0}} \tag{7.11f}$$

$$D = \cos\beta_0\cos\beta\cos\left(\alpha - \alpha_0\right) + \sin\beta_0\sin\beta \tag{7.11g}$$

Where we have dropped the absolute value sign because all angles that we will be considering will be in the first quadrant, between $0\,^\circ$ and $90\,^\circ$. Therefore we can define our standard coordinates as

$$X = \frac{S_{P1}}{D} = \frac{\cos\beta\sin\left(\alpha - \alpha_0\right)}{\cos\beta_0\cos\beta\cos\left(\alpha - \alpha_0\right) + \sin\beta_0\sin\beta} \tag{7.11h}$$

$$Y = \frac{S_{P2}}{D} = \frac{\cos\beta_0\sin\beta - \sin\beta_0\cos\beta\cos\left(\alpha - \alpha_0\right)}{\cos\beta_0\cos\beta\cos\left(\alpha - \alpha_0\right) + \sin\beta_0\sin\beta} \tag{7.11i}$$

Given $X$ and $Y$ we can define the azimuthal and elevation angles as

$$\alpha = \alpha_0 + \arctan\left(\frac{X}{\cos\beta_0 + Y\sin\beta_0}\right) \tag{7.12a}$$

$$\beta = \arcsin\left(\frac{\sin\beta_0 - Y\cos\beta_0}{\sqrt[2]{1+X^2+Y^2}}\right) \tag{7.13a}$$

as per (Larsen, pg. 1). With the above equations our description is almost complete. The only missing pieces are the determination of the position angles of a given pixel position and the distance from the camera site to the projection of the image position onto the earth's surface.

To determine the angular position of an image point we use the standard system of celestial coordinates. We will employ the use of the background stars to convert the azimuthal and elevation angles into right ascension, $\rho$, and declination, $\delta$, angles. As per usual $\rho$ is measured from the first point of Aries, namely $\gamma$. The background stars will give a definitive way of testing the coordinate conversion. To convert from celestial to geocentric coordinates we must know the orientation of the camera relative to the celestial sphere as well as a way of describing the motion of the celestial sphere, namely its equation of motion.Figure 7·1 shows a drawing of the celestial sphere as explained in (Larsen, pg. 7) where Larsen uses $\alpha_A$ and $\delta_A$ to denote, respectively, the right ascension and declination of point $A$. As explained above, $\gamma$, is the first point of Aries.

Knowing the orientation of the camera system relative to the celestial sphere reduces to knowing the time that the image was taken relative to a reference time, $t_0$. From $t_0$ we can find the $\gamma$ that it corresponds to in any standard star catalog. If we call $\Phi_0$ the reference angle at $t_0$ then it follows that $\Phi$ is the hour angle of the first point of Aries, the vernal equinox, at some time $\Delta t$ after $t_0$.

The main problem to address is the position of the NLCs relative to the earth. To

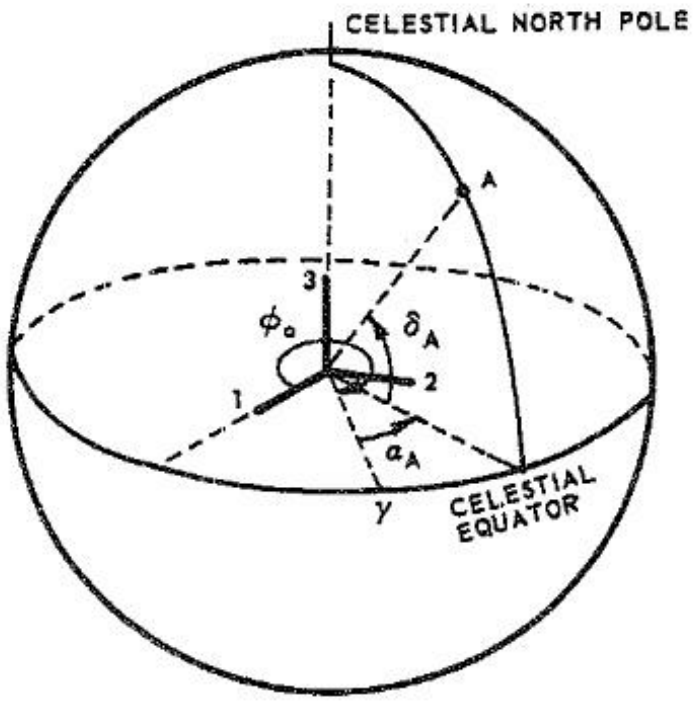


**Figure 7·1:** A rough drawing of the celestial sphere, taken from (Larsen, pg. 7).

do this we must take a step back and look at all of the coordinate systems involved. The coordinate systems that we will consider are the topocentric coordinate system, the celestial coordinate system, the standard coordinate system, the geocentric coordinate system, and the image coordinate system.

The topocentric coordinate system is a Cartesian coordinate system centered at the camera station. The $z$-axis is directed radially outwards. The $x$-axis is directed eastwards from the camera and the $y$-axis is directed northwards from the camera, both of which are mutually orthogonal to one another and the $z$-axis.Figure 7·2 shows a topocentric coordinate system as explained by (Larsen, pg. 5), where 4, 5, and 6 are used to denote the $x$, $y$, and $z$-axes, respectively.

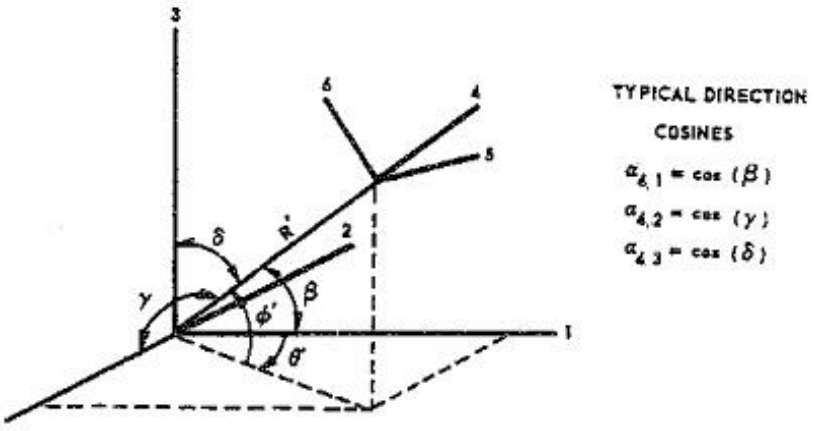


**Figure 7·2:** A topocentric coordinate system taken from (Larsen, pg. 5).

The geocentric coordinate system is Cartesian coordinate system centered at the center of the earth. The $y$-axis increases along the line tangent to the intersection of the equator with the Greenwich Meridian. Positive $x$ is directed towards $90\,^\circ$ east longitude and $0\,^\circ$ latitude. The $z$-axis is directed along a meridian with positive values northwards of the equator. Figure 7·3 shows a geocentric coordinate system as per (Larsen, pg. 4) where 1, 2, and 3, are used to denote the $x$, $y$, and $z$-axes, respectively.

The coordinates of any point in space can be represented as

$$\begin{aligned} x &= R\cos\phi\sin\theta \\ y &= R\sin\phi\sin\theta \\ z &= R\cos\phi \end{aligned} \tag{7.14}$$

as per the standard transformation from Cartesian to spherical coordinates. Where

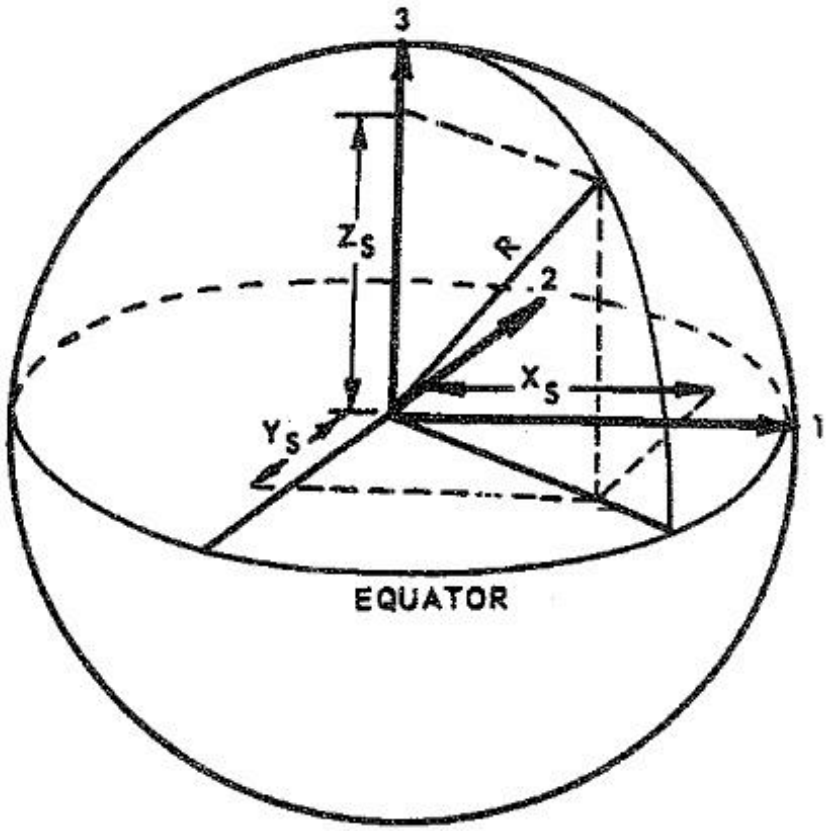


**Figure 7·3:** A geocentric coordinate system as depicted in (Larsen, pg. 4).

$$R = r + h \tag{7.15}$$

$r$ is the radius of the earth and $h$ is the height of the point above the surface,namely above sea level. If $\phi$, $\theta$, and $h$ are, respectively, the latitude, longitude, and height of the camera then we can define a transformation from topocentric to geocentric coordinates using direction cosines, the cosine of the angle between a given vector and a coordinate axis.Figure 7·4 shows two Cartesian coordinate systems as depicted in (Arfken and Weber, pg. 196). The primed coordinate system represents the unprimed coordinate system

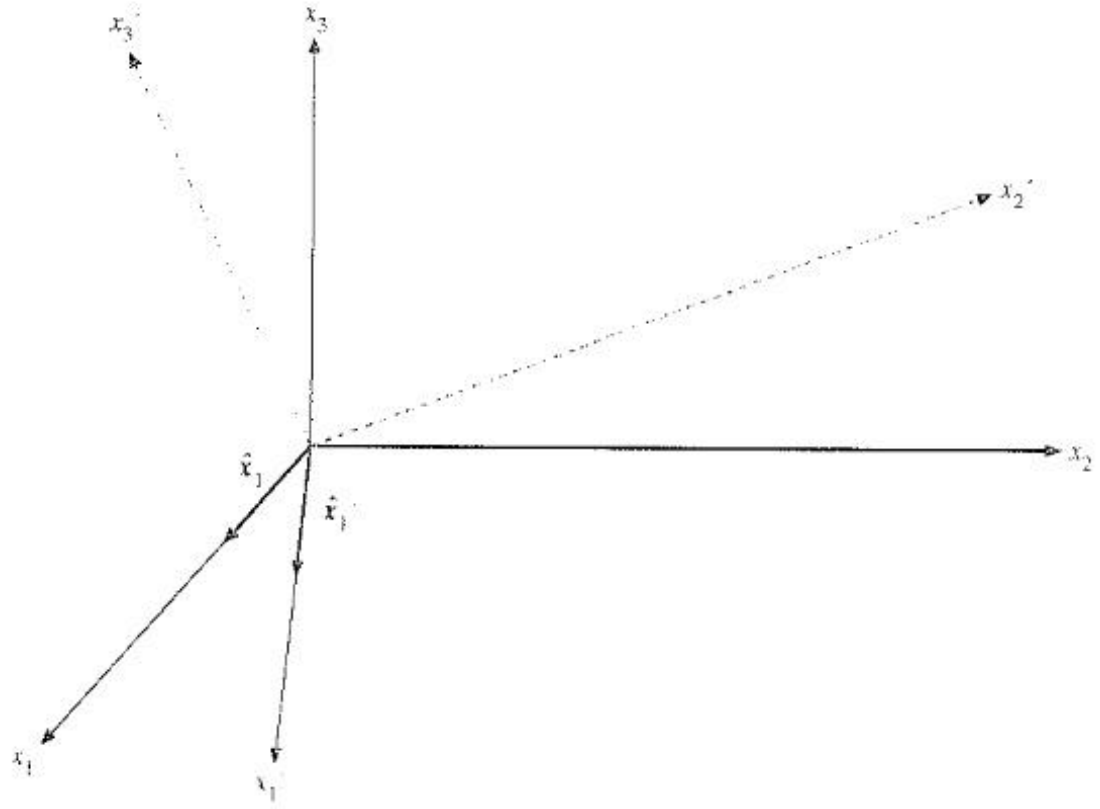

**Figure 7·4:** Two Cartesian coordinate systems taken from (Arfken and Weber, pg. 196). The primed coordinate axes are used to denote a coordinate system that has been rotated from the unprimed coordinate system.

after a rotation. I have taken $x_1$, $x_2$, and $x_3$ to denote the $x$, $y$, and $z$-axes, respectively. The sort of rotation depicted in Figure 7·4 can be described by a set of direction cosines.

Direction cosines are defined as being the cosines of the angle separating two vectors. Given $\mathbf{x}'$, a unit vector along the $x'$-axis, we can define $\mathbf{x}'$ in terms of its projections onto the unprimed coordinate axes, namely the $x$, $y$, and $z$-axes.

$$\mathbf{x}' = \mathbf{x}\left(\mathbf{x}\cdot\mathbf{x}'\right) + \mathbf{y}\left(\mathbf{y}\cdot\mathbf{x}'\right) + \mathbf{z}\left(\mathbf{z}\cdot\mathbf{x}'\right) \tag{7.16}$$

where $\mathbf{x}$, $\mathbf{y}$, and $\mathbf{z}$ are unit vectors along the $x$, $y$, and ,$z$-axes, respectively. Since we are dealing with unit vectors the dot products are simply the cosines of the angles between the two unit vectors, namely the direction cosines. We can write them as

$$\begin{aligned} \mathbf{x} \cdot \mathbf{x}' &= \cos\left(x, x'\right) = a_{11} \\ \mathbf{y} \cdot \mathbf{x}' &= \cos\left(y, x'\right) = a_{12} \\ \mathbf{z} \cdot \mathbf{x}' &= \cos\left(z, x'\right) = a_{13} \end{aligned} \tag{7.17}$$

Summarily with $\mathbf{y}'$ and $\mathbf{z}'$

$$\begin{aligned} \mathbf{x} \cdot \mathbf{y}' &= \cos\left(x, y'\right) = a_{21} \\ \mathbf{y} \cdot \mathbf{y}' &= \cos\left(y, y'\right) = a_{22} \\ \mathbf{z} \cdot \mathbf{y}' &= \cos\left(z, y'\right) = a_{23} \\ \mathbf{x} \cdot \mathbf{z}' &= \cos\left(x, z'\right) = a_{31} \\ \mathbf{y} \cdot \mathbf{z}' &= \cos\left(y, z'\right) = a_{32} \\ \mathbf{z} \cdot \mathbf{z}' &= \cos\left(z, z'\right) = a_{33} \end{aligned} \tag{7.18}$$

We can rewrite 7.16 as

$$\mathbf{x}' = \mathbf{x}a_{11} + \mathbf{y}a_{12} + \mathbf{z}a_{13} \tag{7.19}$$

and likewise

$$\begin{aligned} \mathbf{y}' &= \mathbf{x}a_{21} + \mathbf{y}a_{22} + \mathbf{z}a_{23} \\ \mathbf{z}' &= \mathbf{x}a_{31} + \mathbf{y}a_{32} + \mathbf{z}a_{33} \end{aligned} \tag{7.20}$$

To go from our topocentric coordinate system to our geocentric coordinate system our direction cosines are

$$\begin{aligned} a_{11} &= \cos\phi' \cos\theta \\ a_{12} &= \cos\phi' \sin\theta \\ a_{13} &= \sin\phi' \\ a_{21} &= \sin\theta \\ a_{22} &= \cos\theta \\ a_{23} &= 0 \\ a_{31} &= -\sin\phi' \cos\theta \\ a_{32} &= -\sin\phi' \sin\theta \\ a_{33} &= \cos\phi' \end{aligned} \tag{7.21}$$

where $\phi'$ is the geocentric latitude of the earth. Since the earth isn't a perfect sphere the latitude determined by the local gravitational field will not be the same as the geocentric latitude, angle subtended at the center of the earth. To convert from the geographic latitude to geocentric latitude we assume that the earth is perfect spheroid, a sphere-like shape obtained from rotating an ellipse about one of its principle axes. Therefore the equation of the earth as an ellipse is

$$\left(\frac{x}{a}\right)^2 + \left(\frac{y}{b}\right)^2 = 1 \tag{7.22}$$

where $a$ and $b$ are, respectively, the earth's semi-major and semi-minor radii. If we take the differential we have

$$\frac{2xdx}{a^2} + \frac{2ydy}{b^2} = 0 \tag{7.23}$$

which we can rewrite as

$$\begin{aligned} \frac{xdx}{a^2} &= -\frac{ydy}{b^2} \\ \frac{dx}{dy} &= -\frac{ya^2}{xb^2} \end{aligned} \tag{7.24}$$

but

$$\tan\phi = -\frac{dx}{dy} \tag{7.25}$$

and

$$\tan\phi' = \frac{y}{x} \tag{7.26}$$

so we have

$$\tan\phi = \frac{a^2}{b^2}\tan\phi' \tag{7.27}$$

or

$$\phi' = \arctan\left(\frac{b^2}{a^2}\tan\phi\right) \tag{7.28}$$

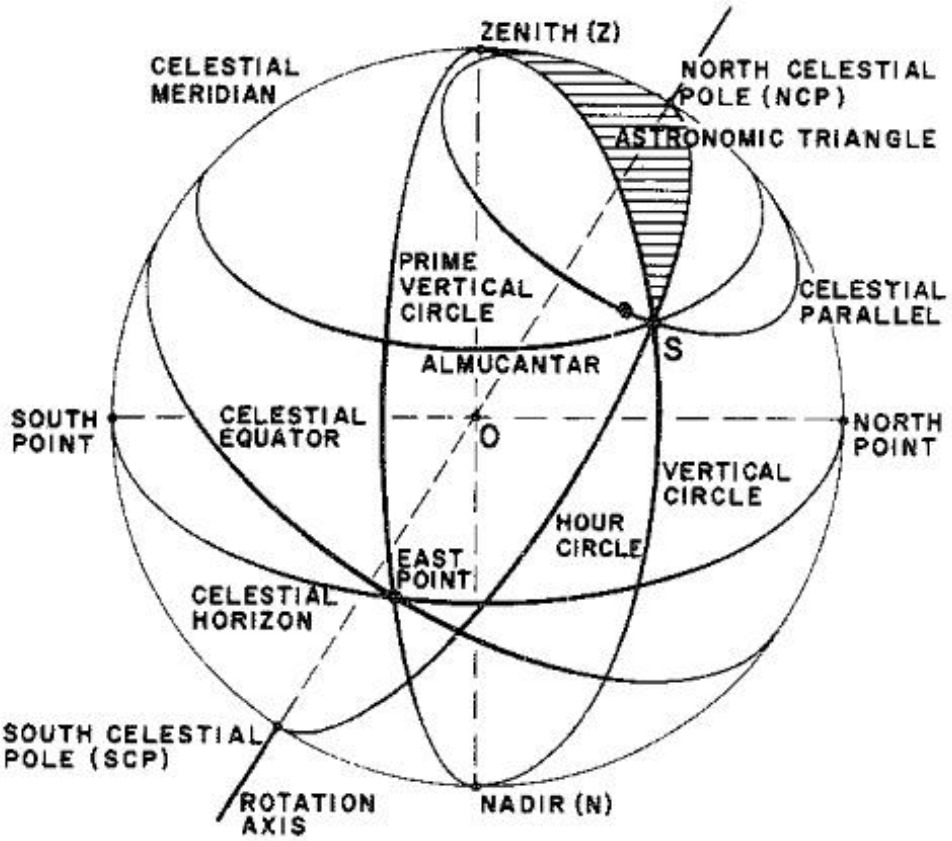


**Figure 7·5:** The celestial sphere as explained by (Mueller and Eichhorn, pg. 30).

The celestial coordinate system, generally, is the best means of locating objects on the celestial sphere, namely stars. Celestial objects are at such a great distance compared to the radius of the earth that they give observers the impression that they are on a sphere that revolves about the observer. This sphere is called the celestial sphere and its surface is a two-dimensional grid that can be used to identify any point on the surface. The intersection of the celestial sphere and the earth is a plane called the celestial equator, where the points of intersection are the north and south celestial poles as seen in Figure 7·5. A great circle is circle that intersects a spherical surface such that

the center of the circle is also the center of the sphere. The great circle that includes both of the celestial poles is called the hour circle. The celestial equivalent of a line of longitude is called the celestial parallel.

The vertical of any sphere has two points of intersection. For the celestial sphere these are called the zenith, above the observer, and the nadir. The plane that contains the observer and is normal to the sphere is called the celestial meridian. Given any point on the celestial sphere, P, we can form a spherical triangle that has a vertex at the P, a pole, and the zenith. Given any point on the celestial sphere, P, we can form a spherical triangle that has a vertex at P, a vertex at the camera's normal, and a point, S, that lies on the same celestial parallel as the camera's projection onto the celestial sphere.

Furthermore the rotation of the earth about its axis from west to east means that the celestial sphere is seen to move from east to west. Therefore all of the celestial coordinates are based on the location of the observer. Because of this we have two celestial coordinate systems to work with, namely the horizon system and the right ascension system.

In the horizon system the celestial horizon is the primary reference plane and the observer's celestial meridian is the secondary reference plane. Given an arbitrary point on the celestial sphere, P, we can determine its position by two angles, namely azimuth and elevation. The azimuth angle, $\theta$, is the angle between the vertical plane of P and the celestial meridian of the camera where we measure it eastwards from the north pole, normally from $0\,^\circ$ to $360\,^\circ$. The elevation angle is measured from the celestial horizon to P, from $0\,^\circ$ to $90\,^\circ$. Figure 7·6 shows the horizon system as explained by (Mueller and Eichhorn, pg. 32) where their reference point is $S$, $a$ is the elevation angle, and $A$ is the azimuthal angle, $z$ is the zenith distance or co-elevation angle, $Z$ and $N$ are the zenith and nadir respectively, while $NCP$ and $SCP$ correspond to, respectively, the north and south celestial poles.

In the right ascension system the primary reference plane is the celestial equator and the secondary reference plane is the hour circle that contains the celestial poles and

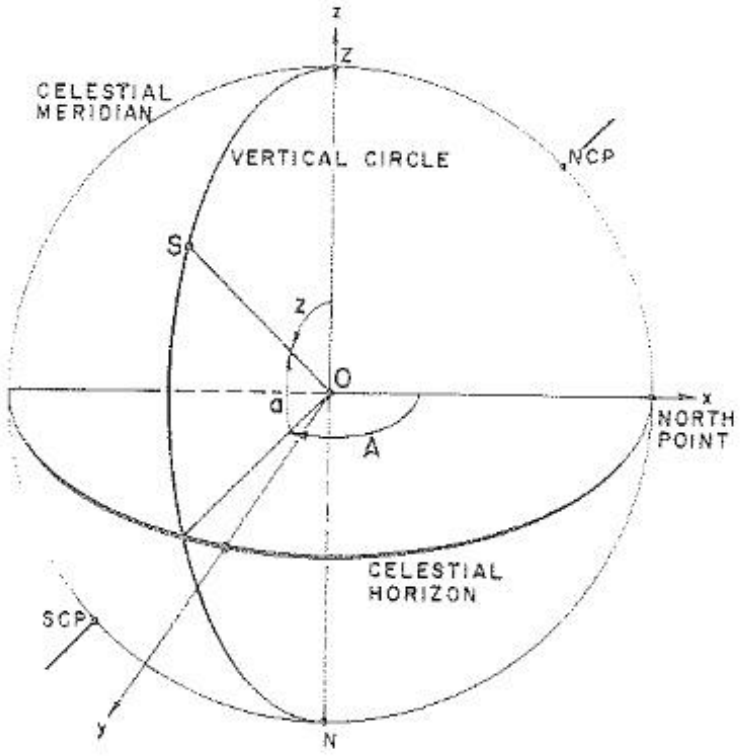


**Figure 7·6:** A drawing, taken from (Mueller and Eichhorn, pg. 32), showing the horizon celestial coordinate system.

equinoxes, namely the equinoctial colure. Given a point, P, on the celestial sphere we call its right ascension, $\alpha$, the angle spanned from the P's hour circle to the equinoctial colure measured eastwards from the vernal equinox, normally from 0 h to 24 h. The declination, $\delta$, is measured from the intersection of P's hour circle to the celestial equator. It has a positive sign on the northern half of the celestial sphere and a negative sign on the southern half. Figure 7·7 shows the right ascension celestial coordinate system as explained by (Mueller and Eichhorn, pg. 34). As per their naming convention, $S$, $Z$, $NCP$, and $SCP$ respectively correspond to their reference point, the zenith, and the north and south celestial poles. The right ascension and declination variables are the same as stated earlier, namely $\alpha$ and $\delta$ respectively.

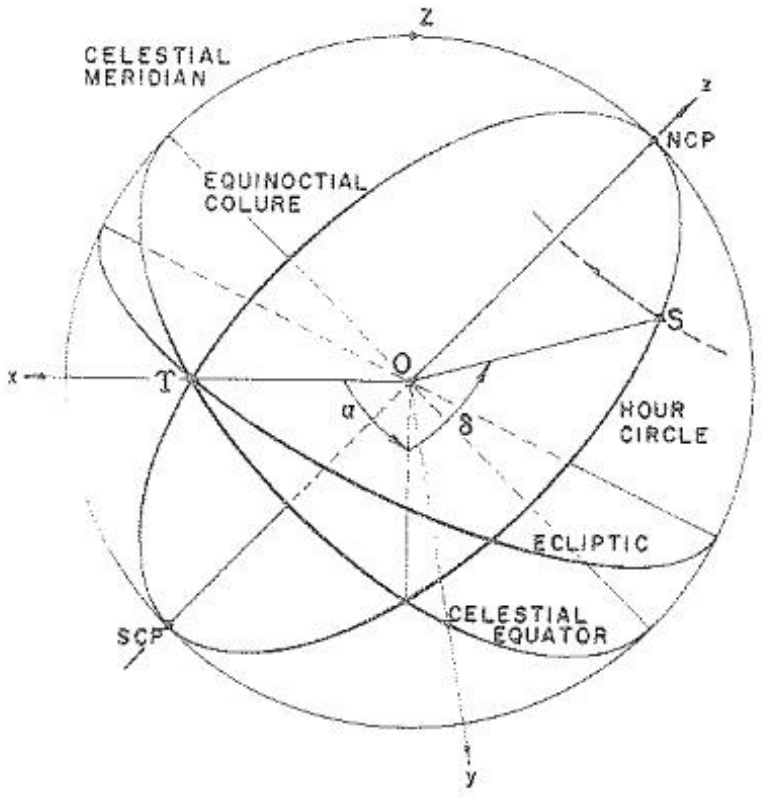


**Figure 7·7:** The right ascension coordinate system as seen in (Mueller and Eichhorn, pg. 34).

The image coordinate system is a Cartesian coordinate system centered on the camera's CCD. We take the y-axis to increase upwards and the x-axis to increase rightward. The dimensions of this system are the same as the camera's CCD, namely millimeters. The standard coordinate system is a similar Cartesian coordinate system that is centered at the azimuth and elevation of the camera's optical axis. The relationship between the image coordinate system and the standard coordinate system is readily obtained from the plate constants as per 7.3. Similarly the transformation from the standard coordinate system to the horizon coordinate system is readily obtained from 7.11i and 7.12a. Therefore we need a transformation from the horizon system to the right ascension system.

The horizon system is based on the observer's field of view relative to their position on the earth. The azimuthal angle tells us which direction the camera is looking at relative to the north pole. The elevation angle tells us the viewing angle of the camera's optical axis subtended by the horizon. In the right ascension system the right ascension tells us the position of a point relative to the hour angle of the vernal equinox. The declination angle is the angle subtended by the point to the celestial equator. Therefore the right ascension system's parallel to the azimuthal angle is the right ascension angle and the declination angle is its parallel to the horizon system's elevation angle. Our task is thus reduced to relating the aforementioned angles. If we know the hour angle of the vernal equinox, $\Phi_0$, for a given reference time, $t_0$, then we can determine the right ascension of a point for any given time, $\Delta t$, thereafter. Given the right ascension, $\rho_P$, for a point, $P$, we define $\theta$, the point's position $\Delta t$ minutes after $t_0$ as

$$\theta = \rho_P - \Phi \tag{7.29}$$

where $\Phi$ is the angular separation of $\rho_P$ and $\theta$ caused by the rotation of the celestial sphere. To determine $\Phi$, the hour angle, precisely we simply have to know how the celestial sphere moves in time. Since the horizon system and the right ascension system both use the celestial equator as the primary reference plane the declination is common to both or independent of $\Phi$. Therefore the only cause for the angular separation between the right ascension and $\theta$ is the passage of time and we need only relate the passage of time to revolutions of the celestial sphere. The apparent motion of the celestial sphere is caused by the Earth's revolution about its axis.

Civil time, time in its most common form, is reckoned in a twenty-four hour day and so the Earth is divided into 24 time zones, each with a width of one hour or $15^\circ$ of longitude. However civil time partitions the day into integer hours. The sidereal day, the time that it takes for a complete revolution of the so called "fictitious sun" along the equator, is actually 23 hours 56 minutes and 4.1 seconds. Where a fictitious sun is used

in place of the real sun because its motion is not uniform. In particular the hour angle of the sun doesn't increase uniformly because the sun doesn't lie on the ecliptic plane and because the sun doesn't lie on the celestial equator. Where the ecliptic plane is defined as the plane containing the center of the sun, the center of mass of the earth-moon system as and its orbit. That irregularity in the sun's hour angle makes it more difficult to use the true sun for time keeping because we want time to be based on a regularly occurring interval. We want our basic intervals of time to be constant and therefore using the actual sun for civil timekeeping would be at odds with our intentions. Therefore we use the fictitious sun which has a uniform sidereal motion along the equator and has an hour angle that is practically identical to that of the actual sun. Therefore the angular separation between the star's actual location and its location in the local time system, namely the image, can be reduced to dimensional analysis, that is a basic unit conversion.

$$\Phi = \Phi_0 + \Delta t \frac{15\,^\circ}{60\,\mathrm{min}} \frac{24\,\mathrm{h}}{23\,\mathrm{h\,s} + \frac{56+\frac{4.1}{60}}{60}\,\mathrm{h\,s}} \tag{7.30}$$

where h denotes hours, min denotes minutes, and h s denotes sidereal hours to give us an offset in degrees. The angle $\Phi_0$ was calculated using **??** for both camera sites.

Now we are all set to relate the azimuth and elevation angles with the right ascension and declination angles. Given our point $P$ with right ascension $\rho_P$ and declination $\delta_P$ the angular separation between $P$ and the hour angle of the vernal equinox, $\gamma$, is given by 7.29. We can define $P$'s position in terms of the standard spherical coordinates, however our axes are aligned such that $\theta$ is measured clockwise from the $X$-axis and so we have to change our sines to cosines and vice versa. Therefore our coordinate transformation is

$$X = \cos\delta_P \cos\theta \tag{7.31a}$$

$$Y = \cos\delta_P \sin\theta \tag{7.31b}$$

$$Z = \sin\delta_P \tag{7.31c}$$

where we are assuming a unit radius because we are considering the distances to distinct stars to be equivalent. This coupled with the 7.19, 7.20, and 7.21 describes the transformation from our topocentric coordinate system to our geocentric coordinate system. Firstly, let's rewrite 7.19 and 7.20 in the form of a matrix equation.

$$\begin{bmatrix} X' \\ Y' \\ Z' \end{bmatrix} = \begin{bmatrix} a_{X'X} & a_{X'Y} & a_{X'Z} \\ a_{Y'X} & a_{Y'Y} & a_{Y'Z} \\ a_{Z'X} & a_{Z'Y} & a_{Z'Z} \end{bmatrix} \begin{bmatrix} X \\ Y \\ Z \end{bmatrix} \tag{7.32}$$

where the primed coordinates represent $P$'s position in the geocentric coordinate system and the unprimed coordinates represents $P$'s position in the topocentric coordinate system. But we already have $P$'s coordinates in the topocentric coordinate system. With the plate constants we can turn any $x$-$y$ coordinate pair into an $\alpha$-$\beta$ coordinate pair. Therefore we need an inverse transformation that converts an $\alpha$-$\beta$ coordinate pair to a $\rho$-$\delta$ coordinate pair, that is a transformation that goes from the topocentric coordinate system to the geocentric coordinate system. Since we have written 7.32 as a matrix equation our problem reduces to a linear algebra problem. First let's fill in our direction cosines to get

$$\begin{bmatrix} X' \\ Y' \\ Z' \end{bmatrix} = \begin{bmatrix} \cos\phi'\cos\theta & \cos\phi'\sin\theta & \sin\phi' \\ \sin\theta & \cos\theta & 0 \\ -\sin\phi'\cos\theta & -\sin\phi'\sin\theta & \cos\phi' \end{bmatrix} \begin{bmatrix} X \\ Y \\ Z \end{bmatrix} \tag{7.33}$$

Our problem of finding an inverse transformation reduces to inverting the above matrix equation which reduces to inverting the matrix of direction cosines.

A basic concept of linear algebra is the inverse matrix. Given a $m \times n$ matrix $A$ its inverse $A^{-1}$ is an $n \times m$ matrix such that

$$AA^{-1} = A^{-1}A = I \tag{7.34}$$

where $I$ is the identity matrix. The inverse matrix, $A^{-1}$, is defined as

$$\frac{(\operatorname{cof} A)^T}{\det A} \tag{7.35}$$

where $(\operatorname{cof} A)^T$ is the transpose of the matrix of the cofactors of $A$ and $\det A$ is the determinant of $A$. The determinant of a matrix is only defined for square matrices. For a $2 \times 2$ matrix $B$ defined as

$$\begin{bmatrix} a_1 & a_2 \\ b_1 & b_2 \end{bmatrix} \tag{7.36}$$

the determinant of $B$ is

$$\det B = \left| \begin{bmatrix} a_1 & a_2 \\ b_1 & b_2 \end{bmatrix} \right| = a_1 b_1 - c_1 d_1 \tag{7.37}$$

and for $C$, a $3 \times 3$, we write the determinant as

$$\det C = \left| \begin{bmatrix} a_1 & a_2 & a_3 \\ b_1 & b_2 & b_3 \\ c_1 & c_2 & c_3 \end{bmatrix} \right| = a_1 \left| \begin{bmatrix} b_2 & b_3 \\ c_2 & c_3 \end{bmatrix} \right| - a_2 \left| \begin{bmatrix} b_1 & b_3 \\ c_1 & c_3 \end{bmatrix} \right| + a_3 \left| \begin{bmatrix} b_1 & b_2 \\ c_1 & c_2 \end{bmatrix} \right| \tag{7.38}$$

where the $2 \times 2$ matrices are called minors. In principle the determinant of any square matrix can be expanded in terms of determinants of its minors and so we can write the determinant of any square matrix, $D$, as

$$\det D = \sum_{i=1}^{\infty} \sum_{j=1}^{\infty} \sum_{k=1}^{\infty} ... \epsilon_{ijk} ... a_i b_j c_k ... \tag{7.39}$$

where

$$\epsilon_{ijk} = \begin{array}{ll} +1 & \text{for even permutations of the indices} \\ -1 & \text{for odd permutations of the indices} \\ 0 & \text{for repeated indices} \end{array} \tag{7.40}$$

The cofactor of an entry of $A$, $a_{ij}$, can be defined in terms of the deterrminant of $A$ as

$$a_{ij} = (-1)^{i+j} D_{ij} \tag{7.41}$$

where $D_{ij}$ is the determinant of the minor obtained by omitting the $i$th row and $j$th column of $A$.

And so our matrix of direction cosines has an inverse as long as its determinant is exists and is nonzero. We can compute its determinant as outlined above. Our matrix of direction cosines is

$$M = \begin{bmatrix} \cos\phi' \cos\theta & \cos\phi' \sin\theta & \sin\phi' \\ \sin\theta & \cos\theta & 0 \\ -\sin\phi' \cos\theta & -\sin\phi' \sin\theta & \cos\phi' \end{bmatrix} \tag{7.42}$$

and so its determinant is

$$\det M = \cos\phi' \cos\theta \det \begin{bmatrix} \cos\theta & 0 \\ -\sin\phi\sin\theta & \cos\phi' \end{bmatrix}$$
$$-\cos\phi' \sin\theta \det \begin{bmatrix} \sin\theta & 0 \\ -\sin\phi'\cos\theta & \cos\phi' \end{bmatrix} + \sin\phi' \det \begin{bmatrix} \sin\theta & \cos\theta \\ -\sin\phi'\cos\theta & -\sin\phi'\sin\theta \end{bmatrix} \tag{7.43}$$

$$\det M = \cos^2\phi' \cos^2\theta - \cos^2\phi' \sin^2\theta + \sin\phi' \left(-\sin^2\theta \sin\phi' + \sin\phi' \cos^2\theta\right) \tag{7.44}$$

Collecting like terms we have

$$\det M = \cos^2\theta \left(\cos^2\phi' + \sin^2\phi'\right) - \sin^2\theta \left(\cos^2\phi' + \sin^2\phi'\right) \tag{7.45}$$

and so we have

$$\det M = \cos^2\theta - \sin^2\theta \tag{7.46}$$

which is just

$$\det M = \cos 2\theta \tag{7.47}$$

which is, in general, nonzero and so $M$ is invertible. We only need the matrix of $M$'s cofactors to determine its inverse. To avoid confusion let's first rewrite the elements in $M$ with separate indices for rows and columns.

$$M = \begin{bmatrix} \cos\phi'\cos\theta & \cos\phi'\sin\theta & \sin\phi' \\ \sin\theta & \cos\theta & 0 \\ -\sin\phi'\cos\theta & -\sin\phi'\sin\theta & \cos\phi' \end{bmatrix} = \begin{bmatrix} m_{11} & m_{12} & m_{13} \\ m_{21} & m_{22} & m_{23} \\ m_{31} & m_{32} & m_{33} \end{bmatrix} \tag{7.48}$$

The cofactor of $m_{11}$, $\tilde{m}_{11}$, is

$$\tilde{m}_{11} = (-1)^{1+1} \begin{vmatrix} \cos\theta & 0 \\ -\sin\phi'\sin\theta & \cos\phi' \end{vmatrix} \tag{7.49}$$

which is simply

$$\tilde{m}_{11} = \cos\theta\cos\phi' \tag{7.50}$$

Similarly for the other cofactors we have

$$\tilde{m}_{12} = (-1)^{1+2} \left| \begin{bmatrix} \sin\theta & 0 \\ -\sin\phi' \cos\theta & \cos\phi' \end{bmatrix} \right| = -\sin\theta\cos\phi' \tag{7.51a}$$

$$\tilde{m}_{13} = (-1)^{1+3} \left| \begin{bmatrix} \sin\theta & \cos\theta \\ -\sin\phi' \cos\theta & -\sin\phi' \sin\theta \end{bmatrix} \right| = \sin\phi' \left(-\sin^2\theta + \cos^2\theta\right) = \sin\phi' \cos 2\theta \tag{7.51b}$$

$$\tilde{m}_{21} = (-1)^{2+1} \left| \begin{bmatrix} \cos\phi' \sin\theta & \sin\phi' \\ -\sin\phi' \sin\theta & \cos\phi' \end{bmatrix} \right| = -\sin\theta \left(\cos^2\phi' + \sin^2\phi'\right) = -\sin\theta \tag{7.51c}$$

$$\tilde{m}_{22} = (-1)^{2+2} \left| \begin{bmatrix} \cos\phi' \cos\theta & \sin\phi' \\ -\sin\phi' \cos\theta & \cos\phi' \end{bmatrix} \right| = \cos^2\phi' \cos\theta + \sin^2\phi' \cos\theta = \cos\theta \tag{7.51d}$$

$$\tilde{m}_{23} = (-1)^{2+3} \left| \begin{bmatrix} \cos\phi' \cos\theta & \cos\phi' \sin\theta \\ -\sin\phi' \cos\theta & -\sin\phi' \sin\theta \end{bmatrix} \right| = \left(\cos\phi' \cos\theta \sin\phi' \sin\theta - \cos\phi' \sin\theta \sin\phi' \cos\theta\right) = 0 \tag{7.51e}$$

$$\tilde{m}_{31} = (-1)^{3+1} \left| \begin{bmatrix} \cos\phi' \sin\theta & \sin\phi' \\ \cos\theta & 0 \end{bmatrix} \right| = -\cos\theta \sin\phi' \tag{7.51f}$$

$$\tilde{m}_{32} = (-1)^{3+2} \left| \begin{bmatrix} \cos\phi' \cos\theta & \sin\phi' \\ \sin\theta & 0 \end{bmatrix} \right| = \sin\theta \sin\phi' \tag{7.51g}$$

$$\tilde{m}_{33} = (-1)^{3+3} \left| \begin{bmatrix} \cos\phi' \cos\theta & \cos\phi' \sin\theta \\ \sin\theta & \cos\theta \end{bmatrix} \right| = \cos\phi' \left(\cos^2\theta - \sin^2\theta\right) = \cos\phi' \cos 2\theta \tag{7.51h}$$

and so the inverse of $M$ can be written as

$$M^{-1} = \frac{1}{\cos 2\theta} \begin{bmatrix} \cos\theta\cos\phi' & -\sin\theta\cos\phi' & \sin\phi'\cos 2\theta \\ -\sin\theta & \cos\theta & 0 \\ -\cos\theta\sin\phi' & -\sin\theta\sin\phi' & \cos\phi'\cos 2\theta \end{bmatrix}^T \tag{7.52a}$$

$$M^{-1} = \begin{bmatrix} \frac{\cos\theta\cos\phi'}{\cos 2\theta} & -\frac{\sin\theta}{\cos 2\theta} & -\frac{\cos\theta\sin\phi'}{\sin 2\theta} \\ -\frac{\cos\phi'\sin\theta}{\cos 2\theta} & \frac{\cos\theta}{\cos 2\theta} & \frac{\sin\theta\sin\phi'}{\sin 2\theta} \\ \sin\phi' & 0 & \cos\phi' \end{bmatrix} \tag{7.52b}$$

To verify that $M^{-1}$ is indeed the inverse we need only multiply it with $M$

$$MM^{-1} = \begin{bmatrix} \cos\phi'\cos\theta & \cos\phi'\sin\theta & \sin\phi' \\ \sin\theta & \cos\theta & 0 \\ -\sin\phi'\cos\theta & -\sin\phi'\sin\theta & \cos\phi' \end{bmatrix} \begin{bmatrix} \frac{\cos\theta\cos\phi'}{\cos 2\theta} & -\frac{\sin\theta}{\cos 2\theta} & -\frac{\cos\theta\sin\phi'}{\cos 2\theta} \\ -\frac{\cos\phi'\sin\theta}{\cos 2\theta} & \frac{\cos\theta}{\cos 2\theta} & \frac{\sin\theta\sin\phi'}{\cos 2\theta} \\ \sin\phi' & 0 & \cos\phi' \end{bmatrix} \tag{7.52c}$$

$$MM^{-1} = \begin{bmatrix} \frac{\cos^2\phi'\cos^2\theta - \sin^2\theta\cos^2\phi'}{\cos 2\theta} + \sin^2\phi' & \frac{-\sin\theta\cos\theta\cos\phi' + \cos\theta\sin\theta\cos\phi'}{\cos 2\theta} & \frac{-\cos\phi'\sin\phi'\cos^2\theta + \sin^2\theta\cos\phi'\sin\phi'}{\cos 2\theta} + s \\ \frac{\sin\theta\cos\theta\cos\phi' - \cos\theta\cos\phi'\sin\theta}{\cos 2\theta} & \frac{-\sin^2\theta + \cos^2\theta}{\cos 2\theta} & \frac{-\sin\theta\cos\theta\sin\phi' + \cos\theta\sin\theta\sin}{\cos 2\theta} \\ \frac{-\sin\phi'\cos^2\theta\cos\phi' + \sin\phi'\sin^2\theta\cos\phi'}{\cos 2\theta} + \cos\phi'\sin\phi' & \frac{\sin\phi'\cos\theta\sin\theta - \sin\phi'\sin\theta\cos\theta}{\cos 2\theta} & \frac{\sin^2\phi'\cos^2\theta - \sin^2\phi'\sin^2\theta}{\cos 2\theta} + \cos \end{bmatrix}$$

(7.52d)

$$MM^{-1} = \begin{bmatrix} \frac{\cos^2\phi'\left(\cos^2\theta - \sin^2\theta\right)}{\cos 2\theta} + \sin^2\phi' & 0 & \frac{-\cos\phi'\sin\phi'\left(\cos^2\theta - \sin^2\theta\right)}{\cos 2\theta} + \sin\phi'\cos\phi' \\ 0 & 1 & 0 \\ \frac{-\sin\phi'\cos\phi'\left(\cos^2\theta - \sin^2\theta\right)}{\cos 2\theta} + \cos\phi'\sin\phi' & 0 & \frac{\sin^2\phi'\left(\cos^2\theta - \sin^2\theta\right)}{\cos 2\theta} + \cos^2\phi' \end{bmatrix} \tag{7.52e}$$

$$MM^{-1} = \begin{bmatrix} \cos^2\phi' + \sin^2\phi' & 0 & \sin\phi'\cos\phi' - \cos\phi'\sin\phi' \\ 0 & 1 & 0 \\ \cos\phi'\sin\phi' - \sin\phi'\cos\phi' & 0 & \cos^2\phi' + \sin^2\phi' \end{bmatrix} \tag{7.52f}$$

$$MM^{-1} = \begin{bmatrix} 1 & 0 & 0 \\ 0 & 1 & 0 \\ 0 & 0 & 1 \end{bmatrix} = I \tag{7.52g}$$

and so is indeed our inverse matrix. We can find the inverse transformation by multiplying the left and right-hand sides of 7.33 by **??** as follows

$$\begin{bmatrix} \frac{\cos\theta\cos\phi'}{\cos 2\theta} & -\frac{\sin\theta}{\cos 2\theta} & -\frac{\cos\theta\sin\phi'}{\cos 2\theta} \\ -\frac{\cos\phi'\sin\theta}{\cos 2\theta} & \frac{\cos\theta}{\cos 2\theta} & \frac{\sin\theta\sin\phi'}{\cos 2\theta} \\ \sin\phi' & 0 & \cos\phi' \end{bmatrix} \begin{bmatrix} X' \\ Y' \\ Z' \end{bmatrix} = \tag{7.52h}$$

$$\begin{bmatrix} \frac{\cos\theta\cos\phi'}{\cos 2\theta} & -\frac{\sin\theta}{\cos 2\theta} & -\frac{\cos\theta\sin\phi'}{\cos 2\theta} \\ -\frac{\cos\phi'\sin\theta}{\cos 2\theta} & \frac{\cos\theta}{\cos 2\theta} & \frac{\sin\theta\sin\phi'}{\cos 2\theta} \\ \sin\phi' & 0 & \cos\phi' \end{bmatrix} \begin{bmatrix} \cos\phi'\cos\theta & \cos\phi'\sin\theta & \sin\phi' \\ \sin\theta & \cos\theta & 0 \\ -\sin\phi'\cos\theta & -\sin\phi'\sin\theta & \cos\phi' \end{bmatrix} \begin{bmatrix} X \\ Y \\ Z \end{bmatrix} \tag{7.52i}$$

$$\begin{bmatrix} \frac{\cos\theta\cos\phi'}{\cos 2\theta} & -\frac{\sin\theta}{\cos 2\theta} & -\frac{\cos\theta\sin\phi'}{\cos 2\theta} \\ -\frac{\cos\phi'\sin\theta}{\cos 2\theta} & \frac{\cos\theta}{\cos 2\theta} & \frac{\sin\theta\sin\phi'}{\cos 2\theta} \\ \sin\phi' & 0 & \cos\phi' \end{bmatrix} \begin{bmatrix} X' \\ Y' \\ Z' \end{bmatrix} = \begin{bmatrix} X \\ Y \\ Z \end{bmatrix} \begin{bmatrix} 1 & 0 & 0 \\ 0 & 1 & 0 \\ 0 & 0 & 1 \end{bmatrix} \tag{7.52j}$$

$$\begin{bmatrix} \frac{\cos\theta\cos\phi'}{\cos 2\theta} & -\frac{\sin\theta}{\cos 2\theta} & -\frac{\cos\theta\sin\phi'}{\cos 2\theta} \\ -\frac{\cos\phi'\sin\theta}{\cos 2\theta} & \frac{\cos\theta}{\cos 2\theta} & \frac{\sin\theta\sin\phi'}{\cos 2\theta} \\ \sin\phi' & 0 & \cos\phi' \end{bmatrix} \begin{bmatrix} X' \\ Y' \\ Z' \end{bmatrix} = \begin{bmatrix} X \\ Y \\ Z \end{bmatrix} \tag{7.52k}$$

And so we have our inverse transformation that allows us to go from the geocentric coordinate system to the topocentric coordinate system. Now we only have to solve 7.31 for $\delta_P$ and $\theta$. We have

$$X = \cos\delta_P\cos\theta \tag{7.52l}$$

$$Y = \cos\delta_P\sin\theta \tag{7.52m}$$

$$Z = \sin\delta_P \tag{7.52n}$$

We can see that

$$\theta = \arctan \frac{Y}{X} \tag{7.52o}$$

$$\delta_P = \arcsin Z \tag{7.52p}$$

where the right ascension is given by

$$\rho_P = \theta + \Phi. \tag{7.53}$$

Now we have all of the elements necessary to do an image conversion. Starting with 7.3 we can map from the image coordinate system to the standard coordinate system. We can rewrite 7.3 as

$$X = ax + by + c \tag{7.54}$$

$$Y = dx + ey + f \tag{7.55}$$

because we assume that any rotations of the camera axis are uniform across the camera's CCD and therefore uniform across the resulting image. The same can be said about the $x$ and $y$-offsets, as long as they are constant throughout the image we can combine those constants into more generalized constants. Now we are left with two equations and six unknowns for each point in the image that we try to map to over into the standard coordinates and we those unknowns are the so-called "plate constants". As those plate constants define how camera's optical axis is positioned relative to the background star field, determining them for the image is paramount to converting arbitrary points in the image into the standard coordinates. In general only three reference points are necessary to determine the plate constants however such a solution can cause discrepancies away

from those three points. It is only natural to use the stars for those reference points because we know where they are on the celestial sphere at any point in time. And because we are using the stars as a reference we are bound to have more equations than unknowns as per 7.54. This sort of situation is ideal for a least squares solution.

The method of least squares is an approximate way of solving an over determined system using the concept of minimizing the sums of the squares of the residues. The residues represent the deviations between points in the data set and their approximated values. This is best explained by a line, (insert least squares image) where the least squares solution is the line and the residuals are the vertical deviations between the line and the original data points. Given a good image of a background star field we can have $N$ stars and so we can have $2N$ equations with only six unknowns. Their corresponding images coordinates are $(x_1, y_1)$, $(x_2, y_2)$, ..., $(x_n, y_n)$. Their corresponding standard coordinates are
$(ax_1 + by_1 + c, dx_1 + ey_1 + f)$, $(ax_2 + by_2 + c, dx_2 + ey_2 + f), ..., (ax_n + by_n + c, dx_n + ey_n + f)$.
The expressions that we want to minimize become

$$\sum_{i=1}^{N} \left( X_i - x_i \left( a + \frac{1}{F} \right) - by_i - c \right)^2 \tag{7.56}$$

$$\sum_{i=1}^{N} \left( Y_i - dx_i - y_i \left( e + \frac{1}{F} \right) - f \right)^2 \tag{7.57}$$

where the quantities being summed over are the residuals. By applying a least squares fit the overall deviation in the calculated and measured image coordinates will be reduced.

# Part II

# The Calibration of Pressure Sensors for the Mesosphere-Lower Thermosphere

## Chapter 8

# Introduction

Pressure measurements of the atmosphere can be accomplished with various gauges for the various pressure ranges. For tropospheric pressure measurements, $1000\,\text{mbar} - 100\,\text{mbar}$, there are no difficulties in measurement because we are immersed in the atmosphere either directly or indirectly, via the numerous airplanes that are ubiquitous these days. But for measurements above the troposphere this can become quite troublesome as only indirect methods are available. To get instruments above the troposphere, namely into the stratosphere , one usually uses balloons or high altitude aircraft. However, balloons are only useful to about 40 km, above this altitude rockets are the only source of getting instruments into the atmosphere. While expensive, rockets remain the best means of elevating an instrument for an in-situ pressure measurement.

As previously mentioned there are various gauges for various pressure ranges. For tropospheric pressures there are such gauges as the Bourdon gauge and the capacitance manometer. For stratospheric pressures there are the Pirani and thermocouple gauges. But for low pressure systems, below $10^{-3}\,\text{mbar}$, ionization gauges are the only way of accurately measuring the pressure. This is accomplished by creating a current via the ionization of the background gas in the system. This current, which can easily be in the picoampere range, can be readily measured after some amplification. However, each type of pressure gauge has its pros and cons and no pressure gauge is capable of accurate measurements in all pressure ranges.

The CONE, **c**ombined **n**eutral and **e**lectron, sensor, is a rocket borne probe capable of measuring the low pressures found in the Mesophere-Lower Thermosphere, MLT,

region. No single pressure gauge is capable of measuring pressures on all scales however, the MLT region is rather expansive, ranging from 60 km to 180 km. It would be ideal if one probe could be used to study this region. While ionization gauges are ideal for low pressures they become inaccurate at the higher pressures found at the bottom of the MLT region. CONE represents a means of accurately measuring higher pressures with an ionization gauge. The goal of this thesis is to calibrate CONE probes for the pressures found within the MLT region. Properly calibrated, the measurements from the CONE probes can then be used to calculate temperature profiles for the MLT region.

## 8.1 A brief history of ionization gauges

The CONE, **co**mbined **n**eutral and **e**lectron, sensor is a hand-made spherical triode pressure gauge developed by at the University of Bonn(**?**). A basic triode consists of a cathode, an anode, and the ion collector. Originally, the cathode, or filament, was in the center with the grid inserted between it and the ion collector, which was a cylinder enclosing the cathode and grid. This design was incapable of measuring pressures below $9.9 \times 10^{-9}$ mbar because of the photoelectric effect. Electrons which struck the grid produced X-rays. When these X-rays struck the ion collector they would produce photoelectrons which would be accelerated away from the ion collector. This is measured as a current by the ion collector thereby causing the ion collector to inaccurately measure the ion current. The Bayard-Alpert gauge, or BAG, was developed to solve this problem. The positions of the ion collector and the cathode were switched. Additionally, instead of a cylinder the ion collector was a thin wire. This reduction in the surface area of the ion collector greatly reduced the production of photoelectrons allowing the accurate measurement of lower pressures, as low as $1.3^{-12}$ mbar (Lafferty, J.M., 1998).

The principle underlying ionization gauges is to use energetic electrons to ionize the background gas. An anode or grid is then used to screen electrons from the ion collector. The ion collector's potential of 0 V attracts the ions creating a flow of ions to the

collector. This flow is measured as a current by an electrometer which is attached to the ion collector. This current scales linearly with pressure which makes ionization gauges an ideal choice of gauge for low pressures. At the same time, ionization gauges all saturate at some pressure where the ion current rises independently of pressure. In Figure 8·1 we

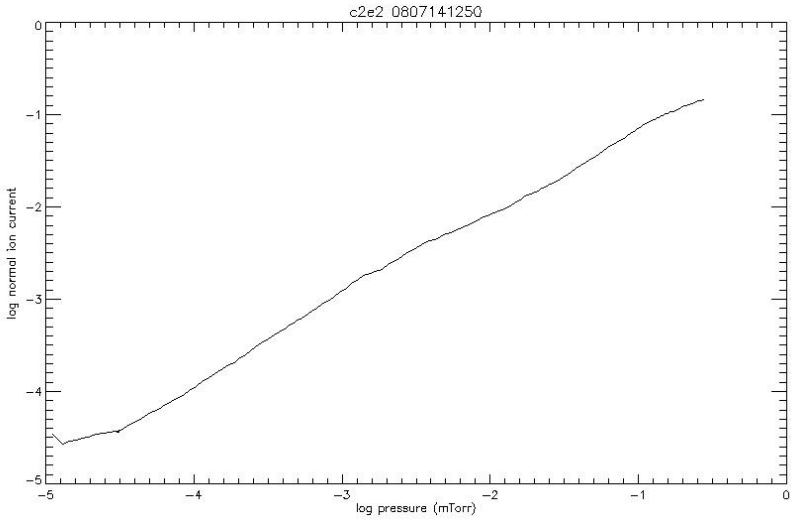


**Figure 8·1:** A plot of pressure versus normalized ion current from a calibration trial of the second CONE probe.

see a plot of the normalized ion current plotted against pressure from a calibration trial for the second CONE probe. The basic equation underling this plot is

$$i_+ = i_- pS \tag{8.1}$$

where $i_+$ is the ion current, $i_-$ is the electron current, $p$ is the pressure, and $S$ is the sensitivity of the gauge. In practice it is usually given by

$$\frac{i_+}{i_-} = pS \tag{8.2}$$

where the quantity $\frac{i_+}{i_-}$ is called the normalized ion current. As the pressure rises beyond

$10^{-3}$ mbar the linear relationship between pressure and current begins to bend downards towards a saturation point. While the pressures in this plot were measured with a MKS Baratron capacitance manometer, the ionization currents were produced by a CONE probe. The high pressure limit of ionization gauges is determined by the production of secondary ions.

Increasing the electric field intensity can be done by decreasing the distance between the cathode and the anode or by increasing the voltage of the anode. Be that as it may, decreasing the electrode distance causes the separation coefficient to increase, while increasing the anode's voltage leads to the ignition of a discharge. To extend the pressure range of the ionization gauge via the electric field intensity requires a small intensity near the cathode and a large one near the anode. This is best accomplished with a spherical electrode assembly(Kudzia, J. and Stôwo, W., 1980). CONE is such a pressure gauge and because of that it measure pressures up to 1 mbar . The generation of secondary ions is limited by the distance between the ion collector and the +85 V of the anode.

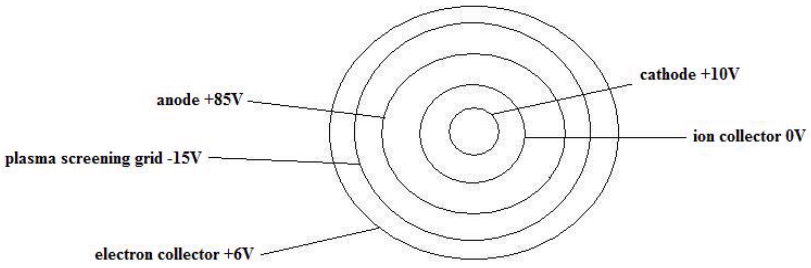


**Figure 8·2:** A schematic layout of the grids for a CONE probe.

CONE is comprised of four concentric spherical grids which encapsulate the cathode, three of which can be seen in Figure 8·3. As CONE was designed to operate within the MLT region, it needed a mechanism to prevent interference from the plasmas within the ionosphere. On the other hand, its designers wanted it to be able to measure the densities


**Figure 8·3:** A photograph of one of the CONE probes taken during a vibration test. The picture clearly shows the filament and three of the concentric spherical grids.

within those same plasmas. Therefore, it was given two extra grids, the outermost acted was given a +6 V potential which allowed it to act as a fixed biased Langmuir probe while the subsequent grid used a −15 V to screen any positive ions from the probe's exterior. Immediately within the anode is the ion collector, the grid from which the ion current is measured by the electrometer. An electron produced by the filament ionizes the neutral that it comes in contact with. The cathode then attracts the electrons while the ion collector attracts the ions, from which the ion current is measured.

The calibration of an ionization gauge is determined by the relationship between the

gauge's normalized ion current and the actual pressure being measured by the gauge. The normalized ion current is merely the ratio between the ion current and the electron current. The electron current is a product of the emission current, as produced by the filament, and the electrons from the ionization of the background gas. Figure 8·1 is one such relationship. The ion current has a linear relationship with pressure until the current reaches a value of approximately $10^{-3}$ mbar. Above this value there is a point of inflection, above which the pressure increases nonlinearly with respect to the ion current.

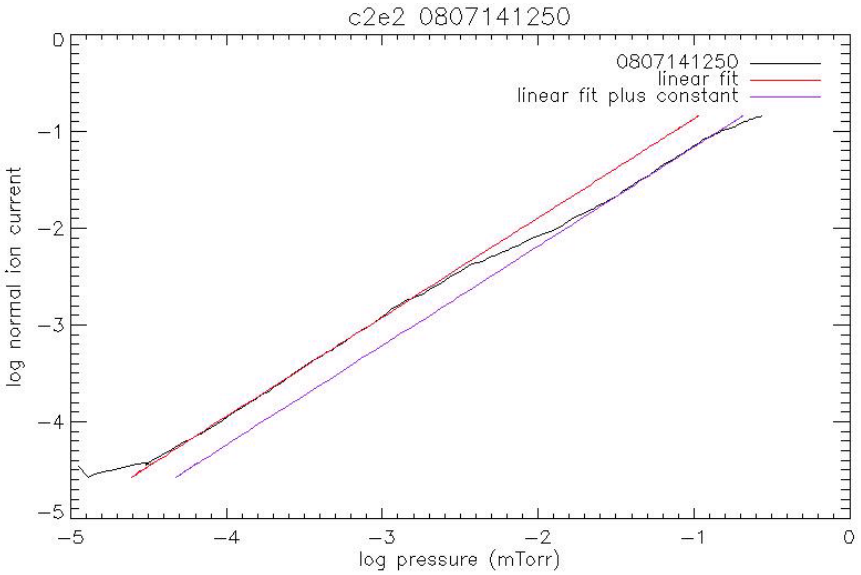


**Figure 8·4:** A plot of the logarithm of the normalized ion current versus the logarithm of pressure. Two linear plots are included to emphasize the nonlinearity around the point of inflection.

This is best seen in Figure 8·4. Therein, a calibration curve is plotted along with two linear fits which help to emphasize the region of nonlinearity in the data. The goal of the calibrations is to mathematically describe all three regions of the data set, in particular the nonlinear region.

## Chapter 9

# Experimental Setup and Procedure

Three CONE probes were hand-crafted by a team at the Lebiniz-Institut für Atmosphärenphysik in Kühlungsborn, Germany, for a rocket campaign in February of 2009. Two of the probes were to be used for the experiment with the third as a backup. The electrometers were developed by Prof. Charles Croskey of Penn State, where each electrometer was calibrated for a specific CONE probe.

For calibration experiments the CONE probe was inserted into a vacuum chamber. The main part of the chamber is a 4 in diameter flange which is mounted to a Pfeiffer TSU 261 turbomolecular pumping station. A 4 in Varian viton sealed swing gate valve is used to partition the main cavity such that the pump can be used continuously on one part of the chamber leaving the other part of the chamber available for experimentation. This part of the chamber has four equidistant flanges of various sizes for various devices along its perimeter as well as an opening at the top of the flange. Three of the side flanges were used for the calibrations while the fourth was sealed.

Figure 9·2 shows a rough schematic of the vacuum chamber assembly used to calibrate the CONE probes. The CONE probes were mounted on a flange which was inserted into the vacuum chamber and bolted to the chamber via an opening at the top of the chamber. Wires from the probe were connected to the electrometer which was connected to a computer. Also attached to the assembly were three pressure gauges; a Pfeiffer PKR 251 compact full range gauge, a MKS 690A01TRC Baratron capacitance manometer, and a MKS SRG2CE spinning rotor gauge. However, the SRG2CE was used mainly to calibrate the Baratron so it isn't included in the schematic. A tank of dry air

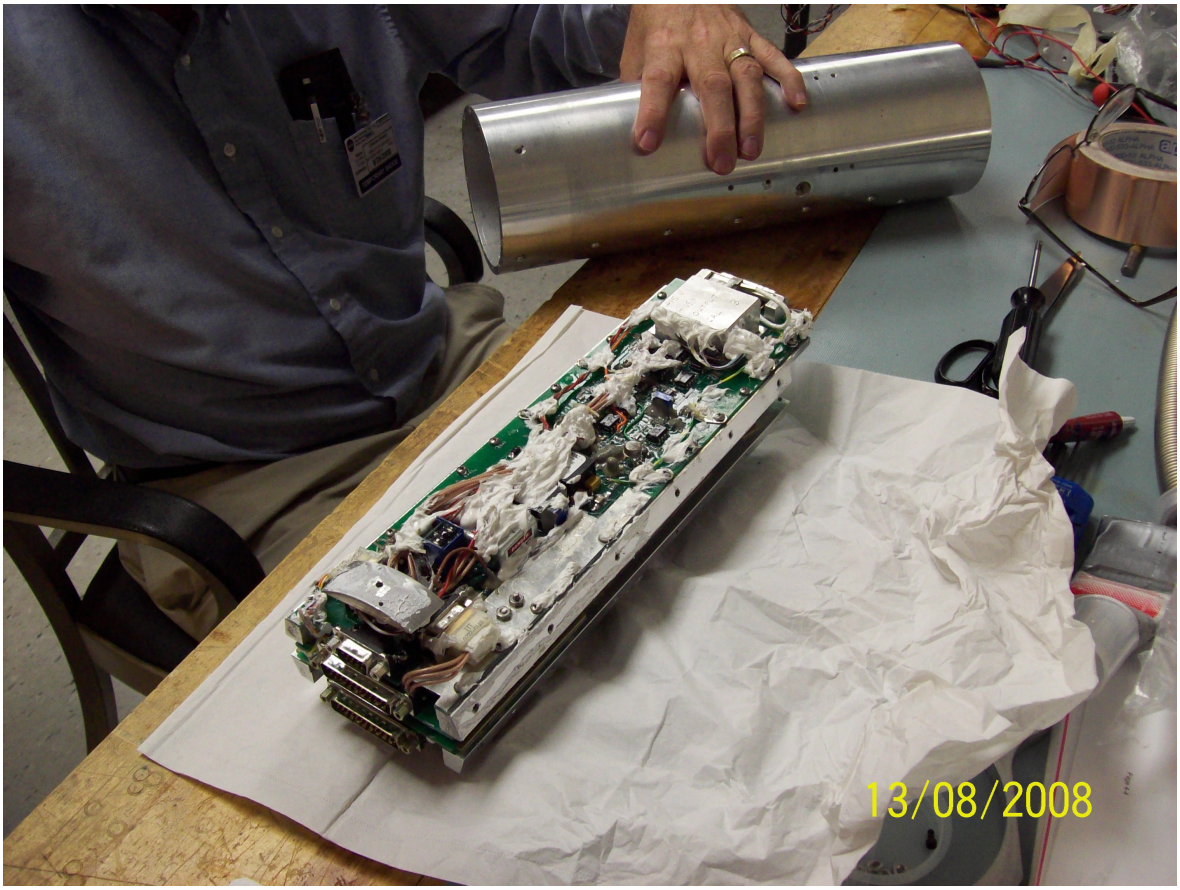


**Figure 9·1:** A picture of one of the electronics units, designed by Prof. Charles Croskey, including the electrometer.

was connected to the inlet valve via flexible tubing. The entire setup was mounted atop the pumping station.

The spinning rotor gauge was used to calibrate the Baratron. While the spinning rotor gauge is highly accurate for the low pressure regime, it becomes inaccurate for higher pressures. The SRG2CE can measure pressures from $3.6 \times 10^{-4}$ mbar to $7.5 \times 10^{2}$ mbar however, any measurements above $7.5 * 10^{-2}$ mbar become increasingly inaccurate. The gauge's RS232 interface unit automatically corrects for this nevertheless, for pressures above $7.5 * 10^{-2}$ mbar the measurements can be up to 10% off. The Baratron has a measuring range from $1.3 \times 10^{-5}$ mbar $-$ 1 mbar with an accuracy of

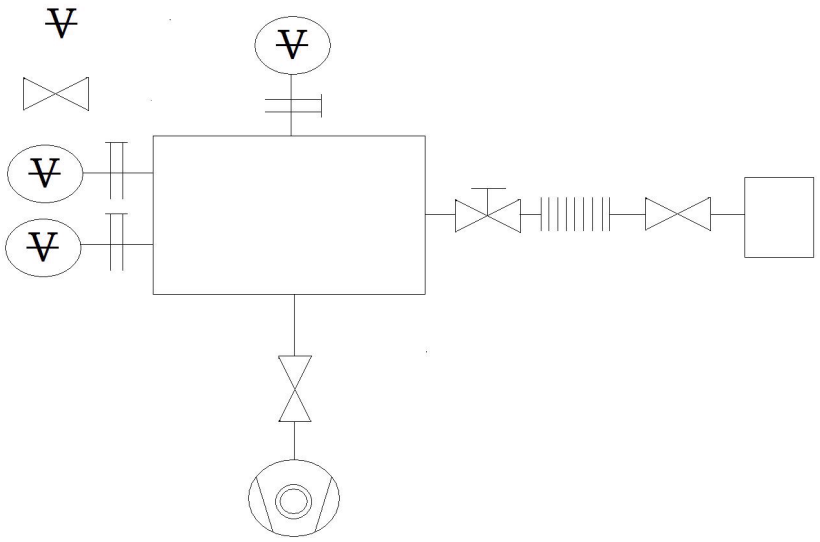

**Figure 9·2:** A schematic of the vacuum chamber setup used in to calibrate the CONE probes.

0.12% of the pressure readings. The PKR 251 was used only for comparison with the pressures from the Baratron. It is comprised of two gauges working in unison, a Pirani and a cold cathode gauge, CCG, based on the principle of the inverted mangetron. The PKR 251 has an accuracy of 30% ranging from $5.0 \times 10^{-9}$ mbar to $10^{4}$ mbar which makes it good enough for order of magnitude comparisons with the Baratron.

To calibrate the CONE probe the swing gate valve was fully opened while the turbomolecular pump evacuated the chamber to the $10^{-9}$ mbar range. This range coincides with the lower pressure range for the Baratron. Then the swing gate valve was closed, leaving the pump operable during experimentation. The filament was then turned on via a switch designed by Charlie Croskey, and this was confirmed by looking at the reading for the filament current. As the Baratron was connected via a flange from the periphery, instead of being in the center of the chamber like the probe, the Baratron's readings were expected to lag behind the readings from the probe. This delay was ameliorated by slowly opening the inlet valve and waiting until the pressure reading

stabilized before further increasing the pressure. This was done roughly five times per decade to give a better, more accurate reading than continuously opening the inlet valve. As the pressure approached 1 mbar, the pressure values rose independently of the inlet valve. This was allowed until the pressures rose into the 1 mbar range as that represents the ceiling for the Baratron's measurements.

The main measurements from the CONE probes were the filament current, the emission current expressed as a voltage, and the electrometer current also expressed as a voltage. The emission current, $I\_$, is just the flow of electrons created by the filament, in addition to the electrons caused by ionization of the background gas, is expected to be the same as the ion current, $I_+$, if all of the ionization takes place between the filament and the ion collector. It was kept constant, at about 14 $\mu$A, by varying the filament current. Prof. Croskey designed all of the electronics for the CONE probes, from the electrometers to the interface between the probes and the computer. He calibrated each electronics unit with its own interface and electrometer. Since the only direct measurement from calibration was the pressure, Dr. Croskey discovered the relationships between the voltage representations of the electrometer current and the emission current to their actual respective currents. If we call the voltage representations of the electrometer current and emission current, respectively, $I_{+v}$ and $I_{-v}$ Dr. Croskey's results can be expressed as

$$\begin{array}{lll} & \text{ion current} & \text{emission current} \\ \text{CONE 1} & \log I_+ = 4.3564 I_{+v} - 24.966 & I_- = \frac{23.173 - 5.4908 I_{-v}}{7.15 * 10^7} \\ \text{CONE 2} & \log I_+ = 4.1983 I_{+v} - 25.684 & I_- = \frac{23.226 - 5.5344 I_{-v}}{7.15 * 10^7} \\ \text{CONE 3} & \log I_+ = 4.0426 I_{+v} - 25.791 & I_- = \frac{23.216 - 5.2662 I_{-v}}{7.15 * 10^7} \end{array} \tag{9.1}$$

where the ion currents are expressed in A and the emission currents are in $\mu$A. The ion current is usually expressed as the ratio of the ion current to the emission current, the so-called normalized ion current.

# Chapter 10

# Results

Two CONE sensors, CONE-1 and CONE-2, were calibrated in for this analysis, each with its own electronics unit and electrometers as per 9.1. Both sensors were used in a rocket campaign during February of 2009. CONE-1 was used in flight 41.078 and CONE-2 was used in 41.079.

The results of each calibration run were recorded via computer. The data sets were labeled based on the date and time of the individual trials. Taking a given data set, 0807111118, the first six digits are the date in the form yymmdd, that is two digit year, month, and day. The remaining four digits correspond to the time ergo, 1118 corresponds to 11:18 Eastern Standard Time on a 12-hour clock.

## 10.1 CONE #1

As previously mentioned, the raw outputs from CONE are the emission and ion currents, expressed as voltages and the filament current. In Figure 10·1 the ion current, expressed as a voltage, is plotted against pressure for various times. Figure 10·1 shows the raw ion current data for CONE #1. The most obvious feature is that the 0807111118 data has markedly lower ion currents than the other data sets. This data set seems to be an aberration because another data set, 0807111500, which was taken the same day, produced currents that agreed with the other calibration trials. The step-like pattern in the plot is a result of incrementally increasing the pressure and allowing time for the Baratron to equilibrate with the CONE. Another noteworthy characteristic of Figure 10·1 is that the data set for 0807111319 seems to have reached the high pressure

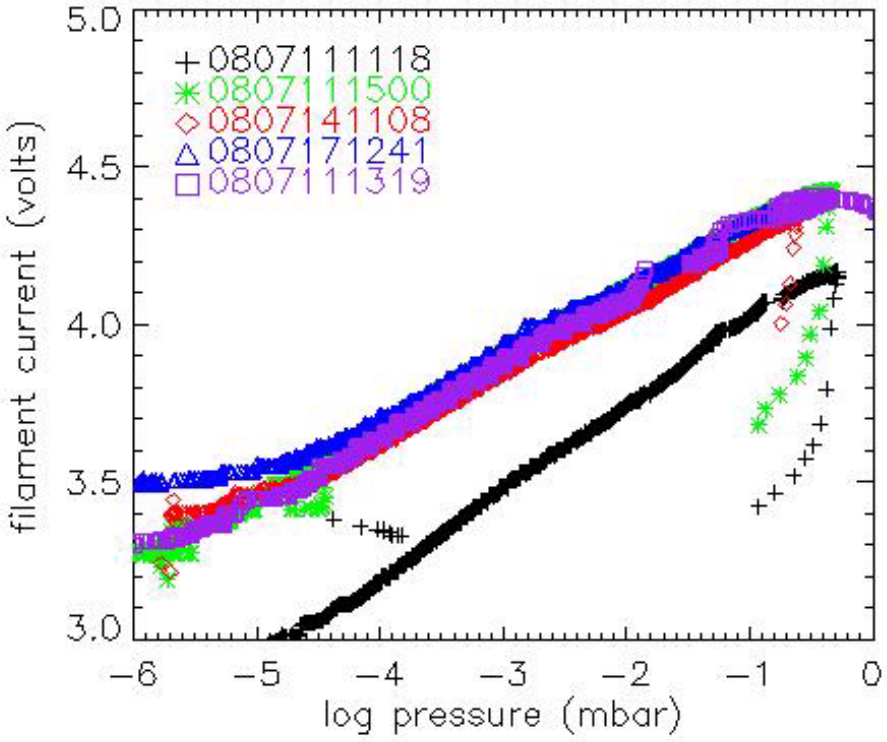


**Figure 10·1:** A plot of the ion current, expressed as a voltage, against pressure for various times.

limit before the other data sets. Starting from $5.01 \times 10^{-2}$ mTorr the ion current seems to be increasing independently of pressure, during the same pressure and current regime as most of the other plots. The 0807111118 data set seems to also reach the high pressure regime. Since both of the irregular data sets were taken on the same day it seems likely that their abnormalities can be attributed to the same cause. Contamination or negligence with the inlet valve seem to be the most likely causes the abnormality.

Figure 10·2 is a plot of emission current, expressed as a voltage, against pressure. For the most part, the values of the emission currents agree for all of the data sets. The only noteworthy aspect is that the 0807111118 data set has currents far lower than the other curves. This is the same inexplicable behavior that was noticed in Figure 10·1.

emiss

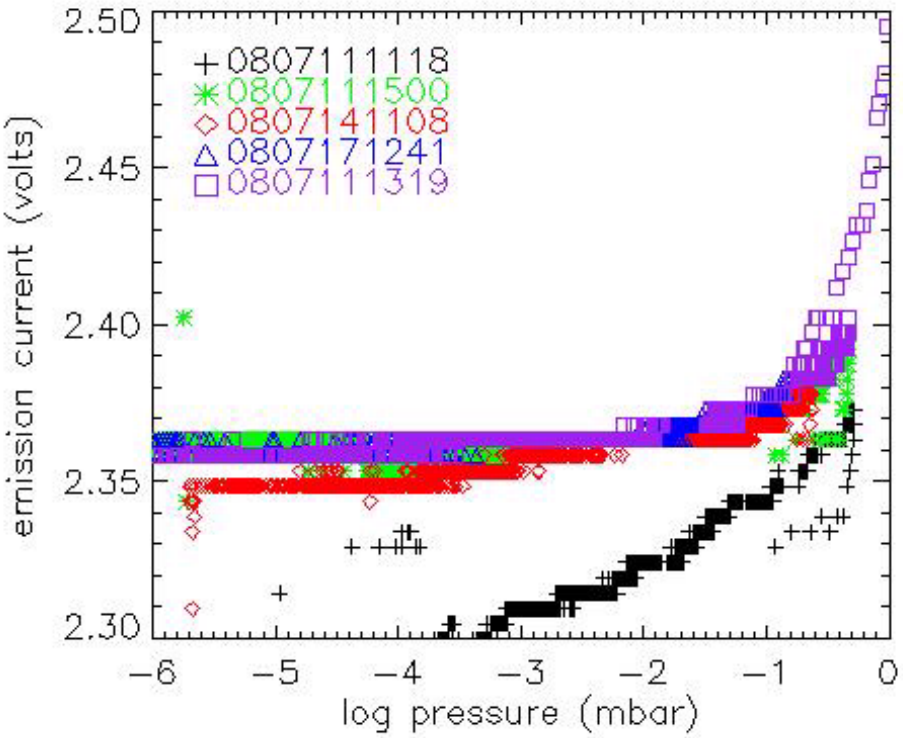


$_{3}$9.*pdf*

**Figure 10·2:** A plot of the emission current, expressed as a voltage, plotted against pressure for various times.

Figure 10·3 shows a plot of the normalized ion current plotted against pressure for several calibration trials. Again the 0807111118 data set produces currents which are far lower than the others. Treating the 0807111118 data set as an outlier, the 0807141108 data set represents the floor of the normalized ion current values while the 0807171241 data set represents the ceiling. The most interesting aspect of Figure 10·3 is how the other two data sets behave between the ceiling and floor plots. The 0807111500 and 0807111319 data sets start off with values similar to those from the floor but, as the pressure increased they asymptotically approach the ceiling.

Looking at Figure 10·4, it is obvious that the 0807111118 data set has a markedly higher filament current. Additionally, looking at

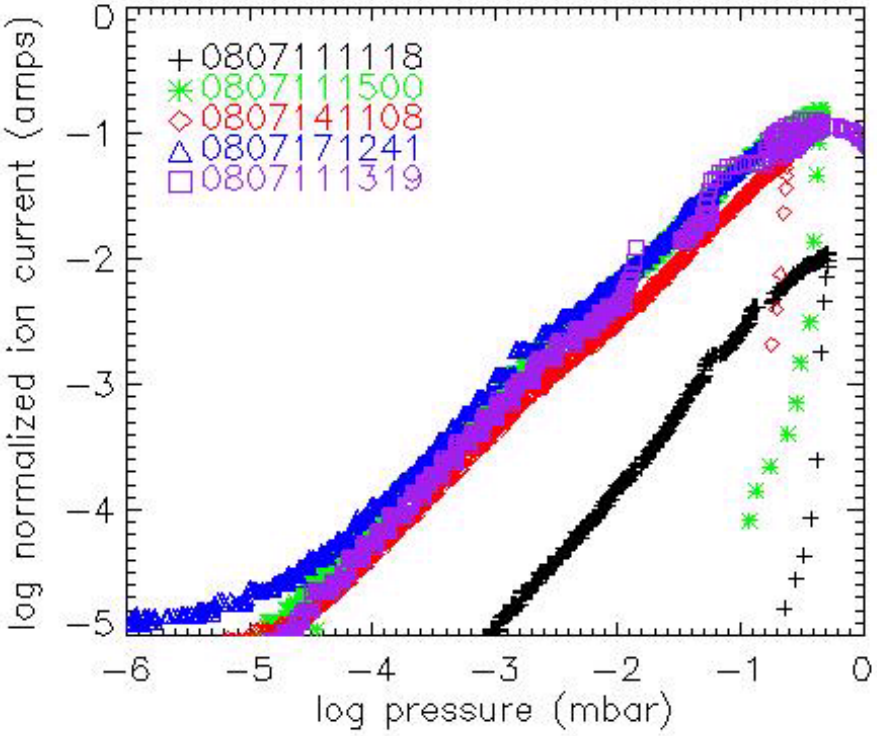


**Figure 10·3:** A plot of the normalized ion current plotted against pressure for several different times.

0807111500 and 0807111319, we see that they start off at a lower filament current than 0807171241 but, they begin to approach it at higher pressures. The 0807141108 data set also approaches the values of the 0807171241 data set. The 0807141108 curve also approaches the values set by the 0807171241 curve for higher pressures. Comparing Figures 10·4 and 10·3 we see that both, the 0807111500 and the 0807111319 curves behave similarly. Based on Figure 10·4, the behavior of the normalized ion currents of the 0807111319 and 0807111500 data sets can be attributed to their corresponding filament currents. Another facet revealed by Figure 10·4 is the behavior of 0807111118 data set. It has median values for the filament current for the entire plot. The fact that it produces currents below all of the other data sets seems to be an artifact of its emission

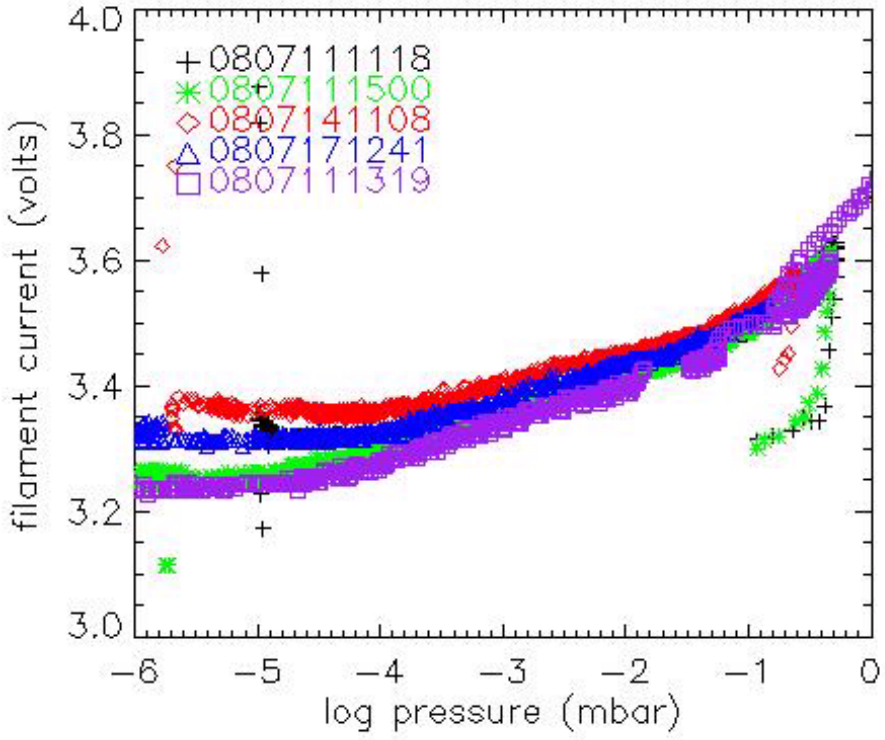


**Figure 10·4:** A plot of the filament current plotted against pressure at various times.

and ion currents. A median value for the filament current indicates that something was happening to the flow of electrons from the cathode which impeded ionization of the background gas.

Two fits were created for each calibration trial to define the pressure in terms of the normalized ion current: a polynomial fit and a Gaussian fit. Both fits were created by first subtracting a linear fit from the region with the point of inflection. A linear fit was done for both linear sections, resulting in two linear fits for each data set. The

coefficients of the linear fit for are as follows

$$\begin{array}{lllll} & x_1 & x_1^0 & x_2 & x_2^0 \\ 0807141108 & 1.0234430 & 0.45450648 & 1.0429411 & 0.61165390 \\ 0807171241 & 1.0319011 & 0.15518509 & 1.0369462 & 0.30570824 \end{array} \tag{10.1}$$

where the subscripts for $x$ delineate the different linear sections. The Gaussian fits had the following coefficients

$$\begin{array}{llll} & z_0 & z_1 & z_2 \\ 0807141108 & 0.087829185 & -2.6293139 & 0.088896268 \\ 0807171241 & 0.13695844 & -1.9364136 & 0.29982745 \end{array} \tag{10.2}$$

where $z_0$ is the height of the Gaussian, $z_1$ is the mean of the data, and $z_2$ is the standard deviation of the data. Given a normalized ion current, $\alpha$, and pressure, $\rho$, the Gaussian fit was computed using

$$\rho = z_0 \exp\left(\frac{-(\alpha - z_1)^2}{2z_2}\right) + x_1\alpha + x_1^0. \tag{10.3}$$

Both the polynomial fits, and the Gaussian fits were calculated using the least squares method. Because the least squares approach is based on minimizing the sum of the residuals, the difference between the expected and actual values squared. Therefore the best parameter to use in describing the fits is the sum of the residuals. The sum of residuals for 0807171241's Gaussian fit was $1.4 \times 10^{-2}$ while the same for 0807141108 was $5.4 \times 10^{-4}$ which indicate that both of the Gaussian fits were quite good. The polynomial fits were done in a similar fashion, subtracting a linear fit from the region with the point of inflection. The coefficients are as follows

$$\begin{array}{lccccccccc} & x^0 & x^1 & x^2 & x^3 & x^4 & x^5 & x^6 & x^7 & \\ 0807141108 & 2620.9170 & 2526.3210 & 444.22412 & -147.97748 & 13.640747 & 33.171539 & 5.3791647 & 0 & . \\ 0807171241 & -512.38263 & -1199.7357 & -1096.4006 & -461.33509 & -60.752798 & 18.744010 & 7.3773086 & 0.72133368 & \end{array} \quad (10.4)$$

A sixth order fit was done for 0807141108 while a seventh order was done for 0807171241. The orders of the polynomial fits were determined by choosing the smallest number of polynomials to produce the cubic like behavior near point of inflection. The sum of the residuals for 0807141108 is $2.4 \times 10^{-3}$ while the same for 0807171241 is $4.3 \times 10^{-3}$ which indicate that both of the polynomial fits were better than the 0807171241's Gaussian fit. The Gaussian fit for 0807141108 was the best fit. Figure 10·5 shows the results of

fit

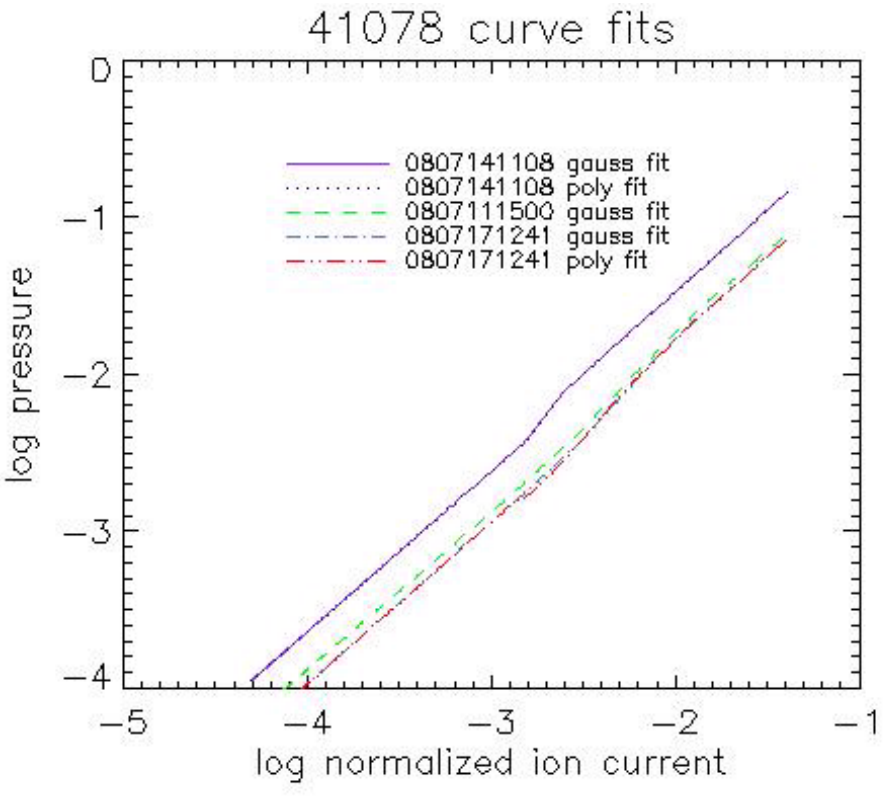


$_4$2.*pdf*

**Figure 10·5:** A plot of several fits to CONE #1's flight data.

several fits to data from CONE #1's flight data. The most obvious aspect is the result of the fits for 0807141108. Both the Gaussian fit and the polynomial fits produced a curve that was shifted leftward. Looking at Figure 10·3, this seems to be an artifact of the difference between ceiling and floor values from the calibration trials. Another noteworthy detail is the bump in 0807171241's polynomial fit around $1.3 \times 10^{-3}$ mbar . It is a rather small bump but, it may affect the corresponding temperature profile.

## 10.2 CONE #2

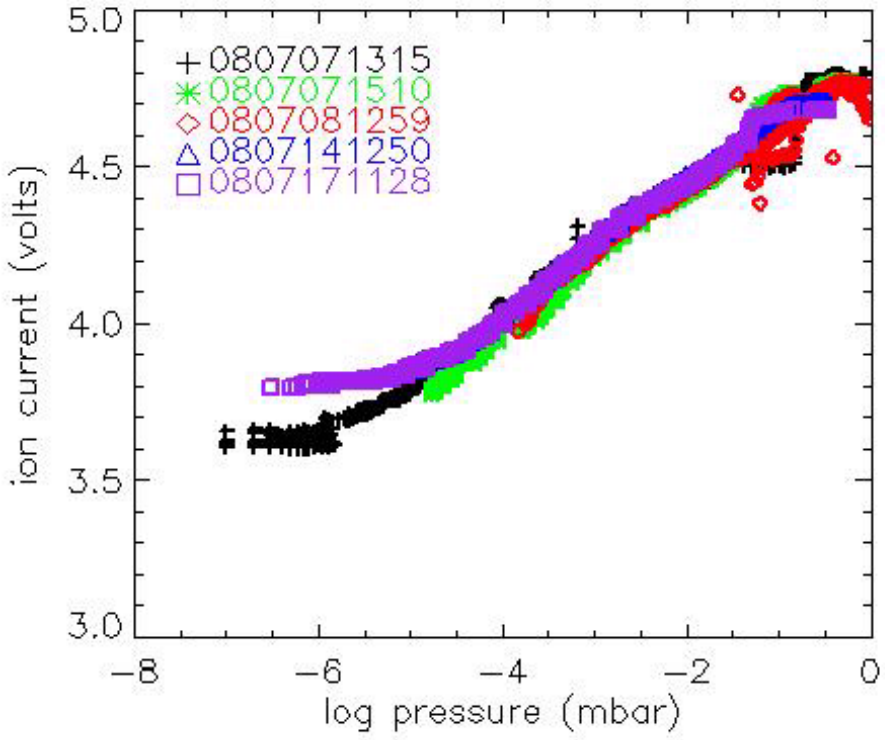


**Figure 10·6:** A plot of the ion current, expressed as a voltage, plotted against pressure for various calibration trials.

Figure 10·6 shows a plot of ion current versus pressure for various calibration trials. This plot shows the raw data from the The most interesting feature of this plot is the way

the various curves begin. Curves, 0807071315, 0807071510, and 0807171128 all start at different ion current values however, as the pressure rises they all converge to the same values. This could be due to the filament's behavior after it is turned on. These curves seem to indicate that the filament operates best after it has been on for a while. Another noteworthy aspect of the plot is the high pressure limit, around $10^{-1.5}$ mbar , for all of the curves. This is in the same order of magnitude as seen in the data from CONE #1, roughly $10^{-1.3}$ mbar . Figure 10·7 shows the emission current, expressed as a voltage,

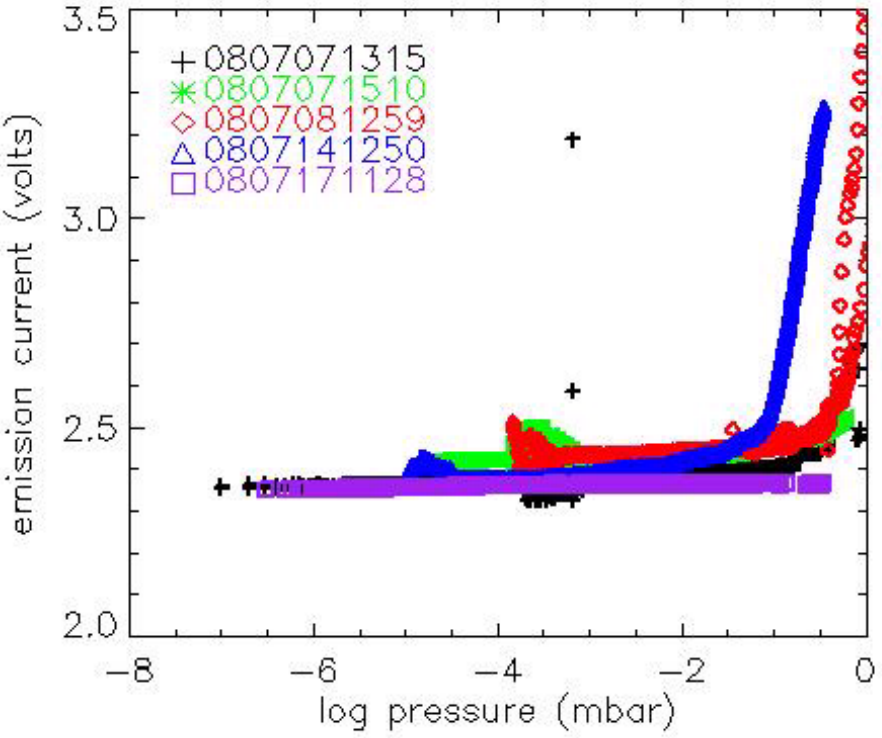


**Figure 10·7:** A plot of the emission current, expressed as a voltage, plotted against pressure for various calibration tests of CONE #2.

plotted against pressure for various calibration experiments. Immediately, the behavior of 0807071315, 0807071510, and 0708081215 between $10^{-4}$ mbar and $10^{-3}$ mbar . The fact that those three curves came from earlier times seems to indicate a temporal cause,

possibly due to the electrometer. Furthermore, all of the curves predict a different high pressure limit. Curve, 0807171128 doesn't even show any trace of the high pressure limit. This is quite different from CONE #1's emission current, where all of the curves increased nonlinearly after, roughly, $10^{-2}$ mbar . Additionally, the emission current for 0807141250 jumps between 10 mbar and $10^{-4}$ mbar . This oscillation could be due to the same mechanism as the oscillations seen in the other curves, despite the fact that both of them occur at different pressures. The oscillation in 0807141250 is approximately the same size as seen in the other curves but it is more well behave. The emission current rose to about 2.4 V and then it asymptotically approached its prior value before rising due to the high pressure limit. Figure 10·8 shows the normalized ion current plotted

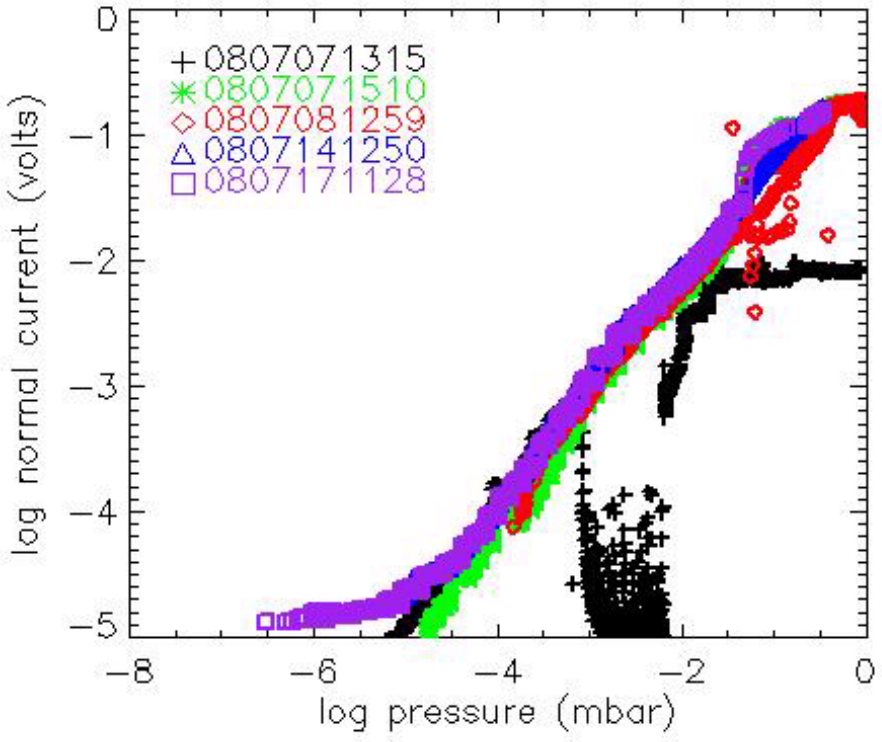


**Figure 10·8:** A plot of the normalized ion current versus pressure for various calibration trials of CONE #2.

against pressure for various calibration trials. Instantly, the behavior of 0807071315 stands out between $10^{-4}$ mbar and $10^{-2}$ mbar . Looking at 0807071510 we can see a similar behavior however, the ion current doesn't oscillate as much as in 0807071315. This could be due, in part, to the fluctuation in the emission currents seen in Figure 10·7 however, the extent of there is a difference in the extent of the fluctuations between the plots. Curves 0807081259 and 0807141250 seem to follow the trend set by the other curves for the most part however, curve 0807081259 falls briefly, at around $10^{-3.8}$ mbar which is precisely where it began fluctuating in Figure 10·7. Figure 10·9 shows a plot of

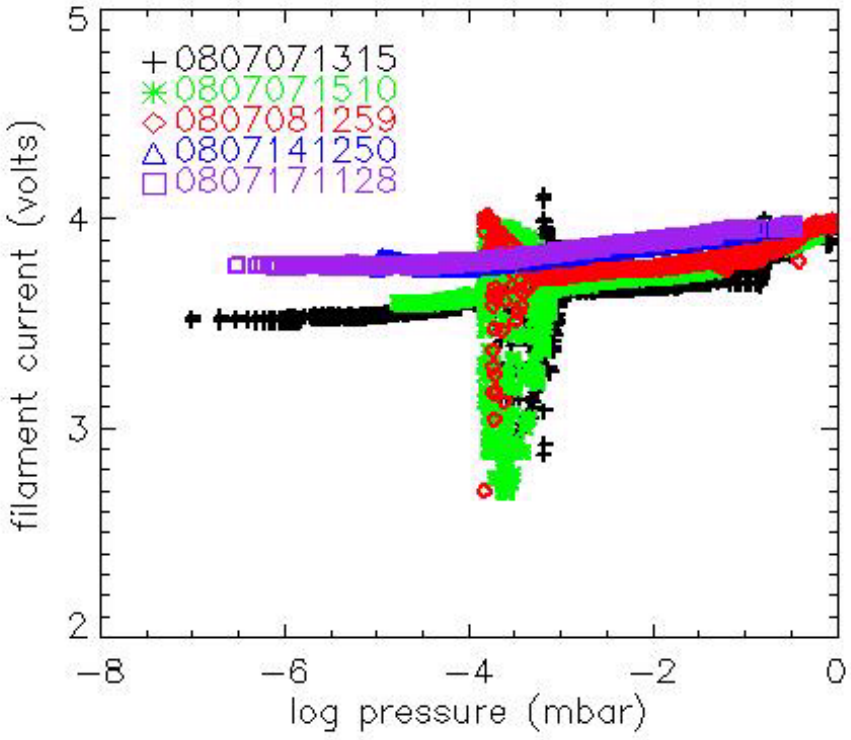


**Figure 10·9:** A plot of the filament current versus pressure for various calibration trials of CONE #2.

the filament current plotted against pressure for various calibration trials. Immediately, the fluctuations between $10^{-4}$ mbar and $10^{-3}$ mbar stand out. The extent of

0807071315's fluctuations are screened by 0807071510's however, this explains the fluctuations within the previous plots except for 10·8. The electronics were designed to keep the emission current constant by varying the filament current in a feedback loop. The large oscillations in the filament current imply that the electronics overshot the proper value, akin to a damped harmonic oscillator. The resulting oscillations represent the feedback system trying to correct for that overshot. Both 0807071510 and 0807081259 have relatively median values for their normalized ion currents while 0807071315 has values which are far lower. The fact that the normalized ion current oscillates within the range $10^{-3}$ mbar to $10^{-2}$ mbar indicates that this could be another anomaly. Its absence in all of the other plots indicates that it could be due to the electrometer or another mechanism.

The linear coefficients for CONE #2 are as follows

| | $x_1$ | $x_1^0$ | $x_2$ | $x_2^0$ |
|---|---|---|---|---|
| 0807171128 | 1.0004650 | −0.0079469408 | 0.86057493 | −0.035810723 |
| 0807141250 | 0.97531849 | −0.15248524 | 1.0310500 | 0.20081759 |

(10.5)

and the Gaussian coefficients are

| | $z_0$ | $z_1$ | $z_2$ |
|---|---|---|---|
| 0807171128 | 0.23444151 | −1.8292518 | 0.34856866 |
| 0807141250 | 0.27355265 | −1.7873806 | 0.34360655 |

(10.6)

The sum of the residuals for 0807141250's Gaussian fit is $4.0 \times 10^{-3}$ while the same for

0807171128 is $1.9 * 10^{-3}$. The coefficients of the polynomial fit are as follows

| | $x^0$ | $x^1$ | $x^2$ | $x^3$ | $x^4$ | $x^5$ | $x^6$ | $x^7$ | $x^8$ |
|---|---|---|---|---|---|---|---|---|---|
| 0807171128 | −316.37189 | −720.32556 | −627.20468 | −237.13199 | −15.495911 | 15.659600 | 4.1698513 | 0.17431998 | −0.030553207 |
| 0807141250 | 3395.1462 | 5944.7544 | 2553.1407 | −1532.4128 | −1967.6617 | −808.8971 | −153.83768 | −11.455081 | |

(10.7)

which yield a value of $3.4 \times 10^{-3}$ as the sum of residuals for 0807171128. The sum of differences squared for 0807141250's polynomial fit is $9.6 \times 10^{-3}$. The sum of the residuals for all of these fits are to the order of $-3$ which makes them good fits. Here the Gaussian fits seem better based on the sum of the residuals alone.Figure 10·10 shows the

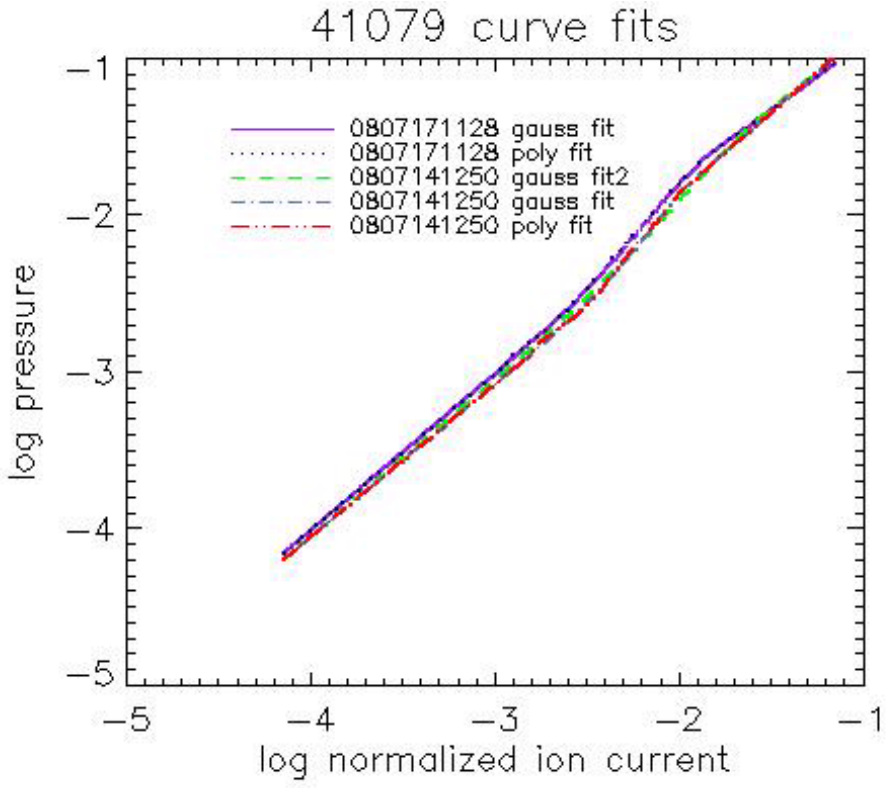


**Figure 10·10:** A plot showing the results of polynomial and Gaussian fits for two of the calibration experiments of CONE #2.

results of polynomial and Gaussian fits to two of the calibration trials. All of the fits

match up pretty well. The main disparity is the burgeoning gap between the fits for 0807171128 and 0807141250 between $10^{-4}$ mTorr and $10^{-2.5}$ mTorr which shrinks for higher pressures. This is also present in Figures 10·8 and 10·9.

# Chapter 11

# Temperature Profiles

There are variations in the calibrations for each sensor. Temperature profiles provide one means of estimating the influences of these variations. The ion current is directly related to the number density of particles within the MLT region. To produce a more accurate temperature profile 2.13 will be integrated from the top using values from an MSIS profile. Figures 10·5 and 10·10 show the results of the calibrations for CONE1 and CONE2 respectively. Using 2.13 the resulting pressures can be converted into densities and temperatures.

Figure 11·1 shows the temperature profiles resulting from two different fit types: Gaussian and polynomial. The curves all agree with the position of the mesopause, the temperature minimum at 93 km. The main discrepancy between the fits occurs roughly between 96 km and 103 km. The inversion of the 0807171241's temperature profile could be due to the bump in the calibration curve however, several other curves share that local maximum, albeit at a different altitude. Despite the confusion between the local maximum or minimum between 96 km and 103 km all of the curves agree rather well with the MSIS profile. Furthermore, all of the curves agree on the altitude of the mesopause while the temperature of the mesopause is $150\,\mathrm{K} \pm 10\,\mathrm{K}$.

Figure 11·1 shows the resulting temperature profiles for the fits. All of the curves math up fairly well, with the main difference being the local temperature maximum near 98 km. Curve 0807171128 has a smoother transition between the two temperature minima while the other curves have steeper transitions resulting in a critical point at 98 km. The

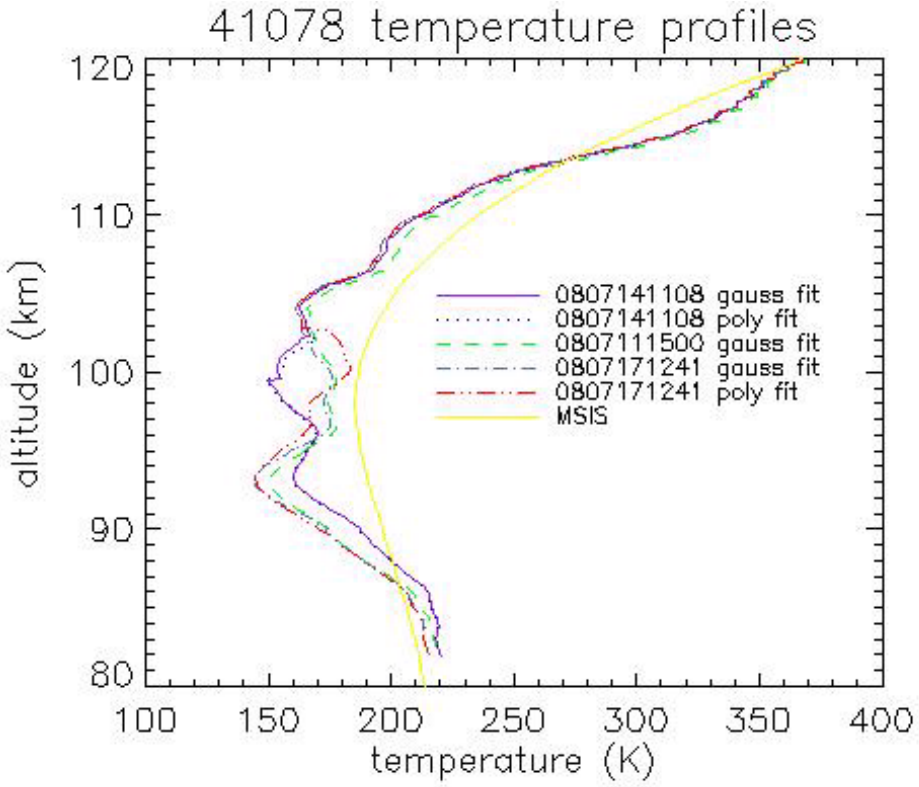


**Figure 11·1:** A plot of the temperature profiles calculated for two of the calibration trials. The results of a gaussian fit are compared to those for a polynomial fit.

curves indicate that the mesopause lies roughly between 92 km and 93 km, with 0807141250's Gauss fit2 producing a slightly lower height than the other curves. This coincides with the mesopause indicated by the results of CONE #1. The local maximum seen at approximately 105 km in CONE #1 is slightly lower, at an altitude of 103 km. Furthermore, the discrepancy seen between 96 km and 103 km in the results of CONE #1 is clarified by local minima seen in the results of CONE #2. CONE #2 predicts a mesopause temperature of $153\,\mathrm{K} \pm 13\,\mathrm{K}$ which agrees well with the $150\,\mathrm{K} \pm 10\,\mathrm{K}$ indicated by CONE #1.

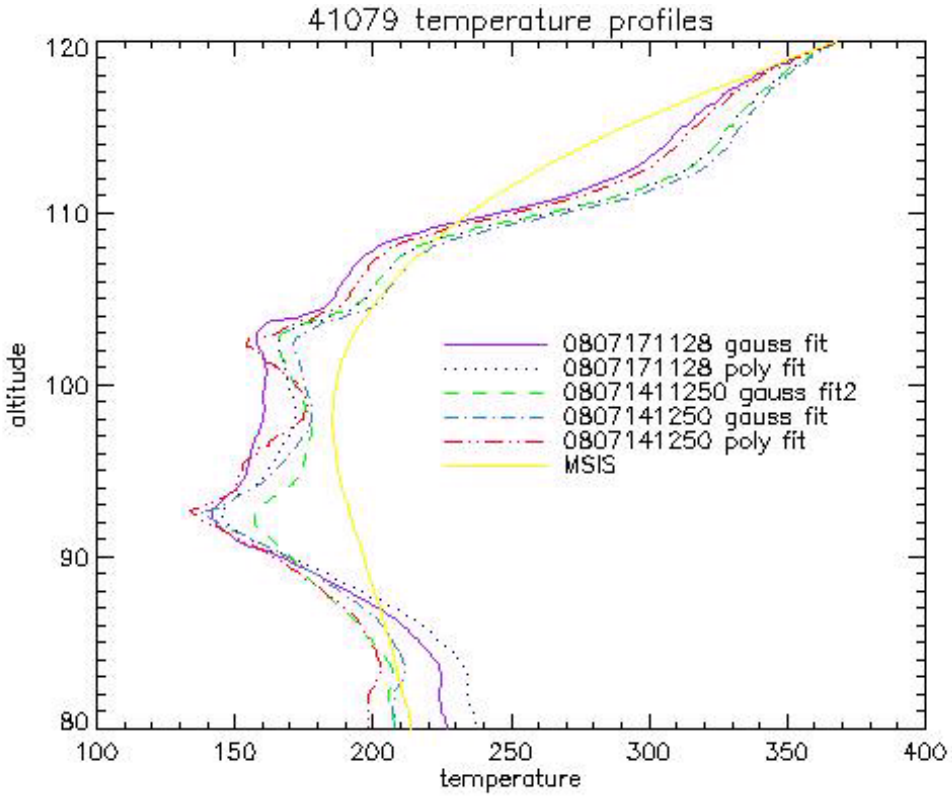


**Figure 11·2:** A plot of the temperature profiles resulting from the two polynomial and Gaussian fits.

## Chapter 12

# Conclusion

The irregularities seen in the various plots were mostly understood. The currents measured by CONE #1 were well behaved, for the most part. The main abnormality was a reduction in the measured ion current for 0807111118 which is attributed to a malfunction of the gauge. CONE #2 produced more interesting results, mainly fluctuations in the emission and filament currents. The fluctuations in the emission currents seem to have been caused by oscillations in the filament currents. The curve for 0807081315 had a pronounced fluctuation in the ion currents which remains an enigma. Curves 0807071510 and 0807081259 both show signs of a mild fluctuation in their corresponding normalized ion currents however, those fluctuations are attributed to the fluctuations seen in their emission currents. The fluctuations in the filament currents seem more of an instrumental error than anything. Whatever mechanism led to them wasn't in the data taken at later times.

The fits were mutually sucessful in removing the point of inflection from the various data sets. As all of the fits were done via the least squares principle, the sum of their resulting residuals was an ideal indicator of their ability to accurately determine their corresponding pressures. All of the fits produced a sum of residuals to the order of $-2$ or lower.

The polynomial and Gaussian fits have produced results that are consistent for both of the CONE probes used in the rocket campaign. The main indications of a successful fit are agreement for the local minima and maxima between 80 km and 120 km. Furthermore, the results of CONE #2 clarified the disparity seen in Figure **??**.

Additionally, the results of both CONE probes indicate that the mesopause lies between 92 km and 93 km with a temperature of about $152\,\mathrm{K} \pm 12\,\mathrm{K}$. The bump seen in the fits for 0807171241 seemed to only have a negligible impact on the temperature profiles. Surprisingly, its temperature profiles agree with the profiles attributed to CONE #2 while the curves for 0807141108 produce a false maxima.

# References


Ammosov, P. P., G. A. Gavrilyeva, and I. I. Koltovskoi. "Observations of Short-Period Waves with an All-Sky Camera in the INfrared Airglow above Yakutsk." Geomagnetism and Aeronomy 46.6 (2006): 760-64. Print.

Arfken, George B., and Hans J. Weber. *Mathematical Methods for Physicists.* Sixth ed. Boston: Elsevier, 2005. Print.

Ayres, Frank, Jr. *Schaum's Outline of Theory and Problems of Plane and Spherical Trigonometry (Schaum's Outline).* New York: McGraw-Hill Education, 1954. Print.

Beeck U., and G. Reich. "A New Method of Linearizing the Characteristics of High-Pressure Ionization Gauges." Vacuum 24.1 (1973): 27-29. Print.

Bronshten, V. A., and N. I. Grishin. *Noctilucent Clouds.* Jerusalem: Keter Publishing House Jerusalem Ltd., 1976. Print.

Fleagle, Robert G., and Joost A. Businger. *An Introduction to Atmospheric Physics.* 2nd ed. Orlando: Academic press, 1980. Print.

Cho, John Y. N., and Jürgen Röttger. "An Updated Review of Polar Mesosphere Summer Echoes: Observation, Theory, and Their Relationship to Noctilucent Clouds and Subvisible Aerosols." Journal of Geophysical Research 102.D2 (1997): 2001-020. Print.

Cleaver, J. S. "A New High-Pressure Ionization Gauge." Journal of Scientific Instruments 44 (1967): 969-72. Print.

Dalin, P., S. Kirkwood, A. Moström, K. Stebel, P. Hoffman, and W. Winger. "A Case Study of Gravity Waves in Noctilucent Clouds." Annales Geophysicae 22 (2004): 1875-884. Print.

Espy, P. J., and H. Jutt. "Equilibrium temperature of Water-Ice Aerosols in the High-Latitude Summer Mesosphere." Journal of Atmospheric and Solar-terrestrial Physics 64 (2002): 1823-832. Print.

Essenwanger, O. M. *Applied Statistics in Atmospheric Science.* Amsterdam: Elsevier Scientific Pub. Co., 1976. Print.

Granville, William A. *Plane and Spherical Trigonometry and Four Place Tables.* Ed. Percey F. Smith and James S. Mikesh. Revised. Second ed. Boston: Ginn and Company, 1941. Print.

Houghton, John Theodore. *Physics of Atmospheres.* Cambridge, U.K: Cambridge UP, 2002. Print.

Jusius, C. G., H. D. Edwards, and R. N. Fuller. "A Method Employing Star Backgrounds for Improving the Accuracy of the Location of Objects in Space." Photogrammetric Engineering (1964): 594-607. Print.

Gadsen, Michael and Schröeder, Wilfried . Noctilucent Clouds. New York: Springer-Verlag, 1989. Print.

CONE- A New Probe for In-Situ Observations of Neutral and Plasma Density Fluctuations, ESA-SP-355, pg. 311-318, 1993.

Jesse, O. "Auffallende Abendersheinungen am Himmel." Meterol Z. 2.20 (1885): 311-12. Print.

Giesen, Jurgen. "Local Sidereal Time Clock." Physik und Astronomie: Applets, Materialien. Web. 23 Nov. 2009. <http://www.jgiesen.de/astro/astroJS/siderealClock/>

Kassander Jr., A. Richard, and Lee L. Sims. "Cloud Photogrammetry With Ground-Located K-17 Aerial Cameras." Journal of Meteorology 14 (1957): 43-49. Print.

Kells, Lyman M., Willis F. Kern, and James R. Bland. *Spherical Trigonometry with Naval and Military Applications.* First ed. New York: McGraw-Hill Book Company, Inc., 1942. Print.

Kirkwood, S., P. Dalin, and A. Réchou. "Noctilucent Clouds Observed from the UK and Denmark – Trends and Variations over 43 Years." Annales Geophysicae 26 (2008): 1243-254. Print.

Kudzia, J., and W. Stôwo. "A Spherical High-Pressure Ionization Gauge." Vacuum 31 (1980): 9-13. Print.

Lafferty, James M., ed. Foundations of Vacuum Science and Technology. New York: Wiley, 1998. Print.

Larsen, Miguel F. "Analysis Techniques for Determining Upper Atmosphere Motions from Sounging Rocket Chemical Tracer Releases". Technical Paper(2004).

Leslie, R. "Sky glows." Nature(London) 32 (1885): 245. Print.

Manson, A. H., C. E. Meek, J. Qian, and C. S. Gardner. "Spectra of Gravity Wave Density and Wind Perturbations Observed During Artic Noctilucent Cloud (ANLC-93) Campaign over the Canadian Prairies: Synergistic Airborne Na Lidar and MF Radar Observations." Journal of Geophysical Research 103.D6 (1998): 6455-465. Print.

McAndrew, Alasdair. *Introduction to Digital Image Processing with MATLAB.* Boston: Course Technology, 2004. Print.

McCulloh, K. E., and C. R. Tilford. "Nitrogen Sensitivities of a Sample of Commerical Hot Cathode Ionization Gage Tubes." Journal of Vacuum Science and Technology 18.3 (1981): 994-97. Print.

Medeiros, A. F., M. J. Taylor, and H. Takahashi. "An Investigation of Gravity Wave Activity in the Low-Lattidue Upper Mesosphere: Propagation Direction and Wind Filtering." Journal of Geophysical Research 108.D14 (2003): 4411-419. Print.

Medeiros, A. F., H. Takahashi, R. A. Buriti, K. M. Pinheiro, and D. Gobbi. "Atmospheric Gravity Wave Propagation Direction Observed by Airglow Imaging in the South American Sector." Journal of Atmospheric and Solar-terrestrial Physics 67 (2005): 1767-773. Print.

Mueller, Ivan I., and Heinrich Eichhorn. *Spherical and Practical Astronomy as Applied to Geodesy.* New York: Frederick Ungar Co., Inc., 1969. Print.

Orville, Harrold D., and A. Richard Kassander Jr. "Terrestrial Photogrammetry of Clouds." Journal of Meteorology 18 (1961): 682-87. Print.

Pear, P. E. "The Choice of Cathode Material in a Hot Cathode Ionization Gauge." Vacuum 26.1 (1975): 3-10. Print.

Schulz, G. J. "Characteristics of the Bayard-Alpert Ionization Gauge at Pressures above $10^{-4}$ mmHg." Journal of Applied Physics 28 (1957): 1149-152. Print.

Stewart, James. *Calculus Concepts and Contexts (with CD-ROM, Make the Grade, and InfoTrac).* Second ed. Belmont: Brooks Cole, 2000. Print.

Wang, Yu-zhi. "A Fundamental Theory of High Pressure Hot Cathode ionization Gauges." Vacuum 34.8/9 (1984): 775-78. Print.

Tserakii, Vitol'd K. "Astronomicheskii Fotometr i Ego Prilozheniya." Mathematicheskii Sbornik 13 (1887): 76-81. Print.

Witt, Georg. "Height, Structure and Displacements of Noctilucent Clouds." Tellus XIV1.(1962): 1-118. Print.

International Noctilucent Cloud Manual. WMO No. 250.TP.138, Geneva